Theoretical studies of molecular dynamical processes using X-ray photoelectron angular distributions

January 2017

Shota TSURU

Graduate School of Advanced Integration Science

CHIBA UNIVERSITY

X 線光電子角度分布を用いた
分子の動的過程の理論的研究

2017 年 1 月

千葉大学大学院融合科学研究科

ナノサイエンス専攻ナノ物性コース

水流　翔太

Acknowledgements

Contents

Chapter 1

General introduction

1.1 X-ray photoelectron diffraction as a surface analysis method

The photoelectric effect was first observed by Hertz in 1887 [1] and Hallwachs in 1888 [2]. This effect is in conflict with classical electrodynamics. Electrons were discovered in 1897, [3] and the above-mentioned photoelectric effect was found to be associated with the emission of electrons from a metal under ultraviolet irradiation [4,5]. Based on the dependence of the emitted electron current on the light intensity and that of the electron velocity on the light frequency, Einstein proposed the concept of photons in 1905 [6], which paved the way to the development of the "Old Quantum Theory". Application of the photoelectric effect to chemistry was hindered by the poor energy resolution of electrons and low quality of vacuum pumps. Meanwhile, X-ray diffraction (XRD), which had been discovered in 1898 [7], was examined by W. H. Bragg and W. L. Bragg in 1913 [8]. Subsequently, crystallography based on XRD was established in the first half of the 20th century [9–11].

The major breakthrough towards chemical analysis using X-ray photoemission was achieved in 1957 through the application of a β-ray detector [12] to X-ray photoelectron detection by K. Siegbahn *et al.*, who succeeded in measuring the electronic binding energies of the atomic inner shells [13]. They continuously obtained X-ray photoelectron spectra that revealed the peak position shift, which is called *chemical shift*, due to the chemical environment of the photoelectron emitter, such as the types of surrounding atoms, nuclear-nuclear distance and coordination number. Thus, they established X-ray photoelectron spectroscopy (XPS), which is also known as electron spectroscopy for chemical analysis (ESCA) [14, 15]. Simultaneously,

ultraviolet photoelectron spectroscopy (UPS) for valence-electronic study was also established [16, 17].

Further, K. Siegbahn *et al.* observed strong diffraction effects in X-ray photoelectron emission from single-crystal substrates [18], which was also observed by Fadley and Bergstrom subsequently [19]. These observations paved the way for the use of X-ray photoelectron diffraction (XPD) and its close relative, Auger electron diffraction (AED), as methods for surface structural analysis. XPD and AED are element-specific and chemical-state-specific; moreover, they are sensitive to bond directions, bond distances, and coordination numbers. Nowadays, XPD and AED are widely used for short-range surface analysis [20–23,27]. Low-energy electron diffraction (LEED), which is a major long-range surface analytical method, is also noteworthy [24].

1.2   Photoelectron diffraction theories

The simplest method for XPD analysis is based on the single-scattering plane-wave (SSC-PW) model [20–22,25–27]. However, the potential shape of scattering-sites and the multiple-scattering (MS) effect sometime influence XPD patterns. Hence, theoretical methods that are more advanced than the SSC-PW model, such as curved-wave-front correction [28–30], linear superposition [31], Rehr-Albers expansion [32–34], and the cluster-model approach [35–38], have been proposed. Fujikawa formulated the MS-XPD theory by renormalization of the scattering path expansion into the inversion of the multiple scattering matrix [39, 40]. This approach simultaneously satisfies both full convergence in the scattering path expansion and the computational cost requirements. Furthermore, it does not use surface symmetry. Thus, it is advantageous for XPD analysis of low-symmetric molecules, such as complicated organic molecules and biomolecules. It should be noted that MsSpec–1.0, a software package for electron spectroscopy, including XPD based on a similar MS approach is available [41].

The MS methods mentioned above are based on partitioning of the scattering potential into spherical potentials that are attached to one another, namely muffin-tin potential [42]. Hatada *et al.* proposed a more sophisticated full-potential MS method with space-filling cells [43, 44], which has been applied to X-ray absorption spectroscopy (XAS) [45]. Application of this method to XPD analysis is desired.

1.3 Inner-shell photoionization of gas-phase molecules

Photoelectron angular distributions (PADs) from isolated gas-phase molecules by X-rays in the laboratory frame (LF) are of the form

$$I(\theta) = \frac{\sigma}{4\pi}[1 + \beta P_2(\cos\theta')], \tag{1.3.1}$$

where σ is the integrated cross section, β is the asymmetry parameter, $P_2(\cos\theta)$ is the Legendre polynomial of the second order, and θ' is measured from the electric vector of the light. This is due to free molecular rotation [46]. In 1976, Dill presented a general formula of PADs from fixed-in-space molecules, i.e., molecular frame photoelectron angular distributions (MFPADs) by a general series of the spherical harmonics $Y_{KM}(\theta, \phi)$:

$$I(\theta, \phi) = \sum_{K=0}^{2l_{max}} \sum_{M} A_{KM} Y_{KM}(\theta, \phi), \tag{1.3.2}$$

where θ and ϕ are measured from the molecular z-axis. This formula is much richer source of information on photoionization dynamics, providing details that are "washed out" by the freely rotating molecules in typical gas-phase experiments [47]. In the 1990s, Golovin *et al.* succeeded in the measurement of an MFPAD from a valence orbital of an O_2 molecule [48]. Then, N_2 $1s$ [49] and CO C $1s$ [50] were measured.

MFPADs from two-atomic molecules are measured using the angle-resolved photoelectron–ion coincidence technique (see Fig. 1.3.1) [51–53]. The two fragment ions are immediately ejected after the Auger decay due to Coulomb repulsion. The initial momenta of the fragment ions $\boldsymbol{P}_1$ and $\boldsymbol{P}_2$ give the recoil axis as the direction of the momentum difference of $\boldsymbol{P}_{recoil} = \boldsymbol{P}_1 - \boldsymbol{P}_2$. The initial photoelectron momentum $\boldsymbol{p}_e$ is measured in coincidence with the ion momenta; then, it is transformed from the LF to the recoil frame (RF). The recoil frame photoelectron angular distributions (RFPADs) measured using this method are regarded as MFPADs with the axial-recoil approximation [54] if the entire process takes place within a timescale that is much shorter than the molecular rotational period. The expansion coefficients of the Legendre polynomials of the MFPADs give the dipole transition matrix elements and the phase shifts for partial waves [55, 56]. Such *complete experiments* for obtaining all the dipole transition matrix elements and phase shifts for photoionization of two-atomic molecules are implemented by the

coincidence measurement mentioned above [57–63]. Furthermore, RFPADs of linear triatomic molecules are measured under the assumption that they can be regarded as MFPADs [64–72].

The original apparatuses for angle-resolved photoelectron–photoion coincidence (AR-PEPICO) measurement [48,51] detect photoelectrons and fragment ions using rotatable analyzers. Hosaka *et al.* developed a new apparatus using imaging detectors, which improved the collection efficiency and allowed for obtaining MFPADs in the energy region above 100 eV [73,74]. The difficulty due to the large number of partial waves for the single-centered expansion in such an energy region was overcome by applying the MS-XPD theory [39,40] for comparison with experimentally obtained MFPADs [75–77]. These studies indicate that the XPD picture can describe MFPADs in a high-energy region. Thus, static molecular structures can be extracted from MFPADs using the trial-and-error method based on the MS-XPD calculations [78].

1.4   Time-resolved molecular imaging

In the late 20th century, Zewail paved the way to femtosecond molecular imaging during chemical reactions using an ultrafast laser technique [79]. Since then, the temporal resolution of the ultrafast laser technique has been reduced to the order of attoseconds, which is sufficient for time-resolved electron imaging [80–82]. Along with the development of lasers for ultrafast electron dynamics, X-ray free-electron lasers (XFELs), such as FLASH at DESY in Hamburg [83–85], the Linac Coherent Light Source (LCLS) at the SLAC National Accelerator Laboratory in Menlo Park, California [86], and the SPring-8 Angstrom Compact free-electron LAser (SACLA) at the RIKEN Harima Institute [87–89], have been developed for ultrafast nuclear dynamics. XFELs have facilitated considerable progress in ultrafast dynamics, as has been reported [90–92].

For time-resolved imaging of isolated gas-phase molecules in the optical laser pump–XFEL probe experimental scheme (see Fig. 1.4.1), molecular orientation or alignment is necessary. Molecular orientation or alignment is usually achieved with the use of strong laser pulses [93]. By combining such pulses with rotational quantum-state selection, Holmegaard *et al.* realized a high degree of alignment of $< \cos^2 \theta_{2D} >= 0.97$ [94]. Molecular orientation or alignment without a laser field has also been studied to avoid its influence on the probe process [95,96]. Recently, Takei *et al.* succeeded in achieving molecular orientation in the laser-field-free condition by using rotational-state selection [97]. By assuming or implementing molecular orientation or alignment based on the above-mentioned methods, many theoretical or experimental studies have been
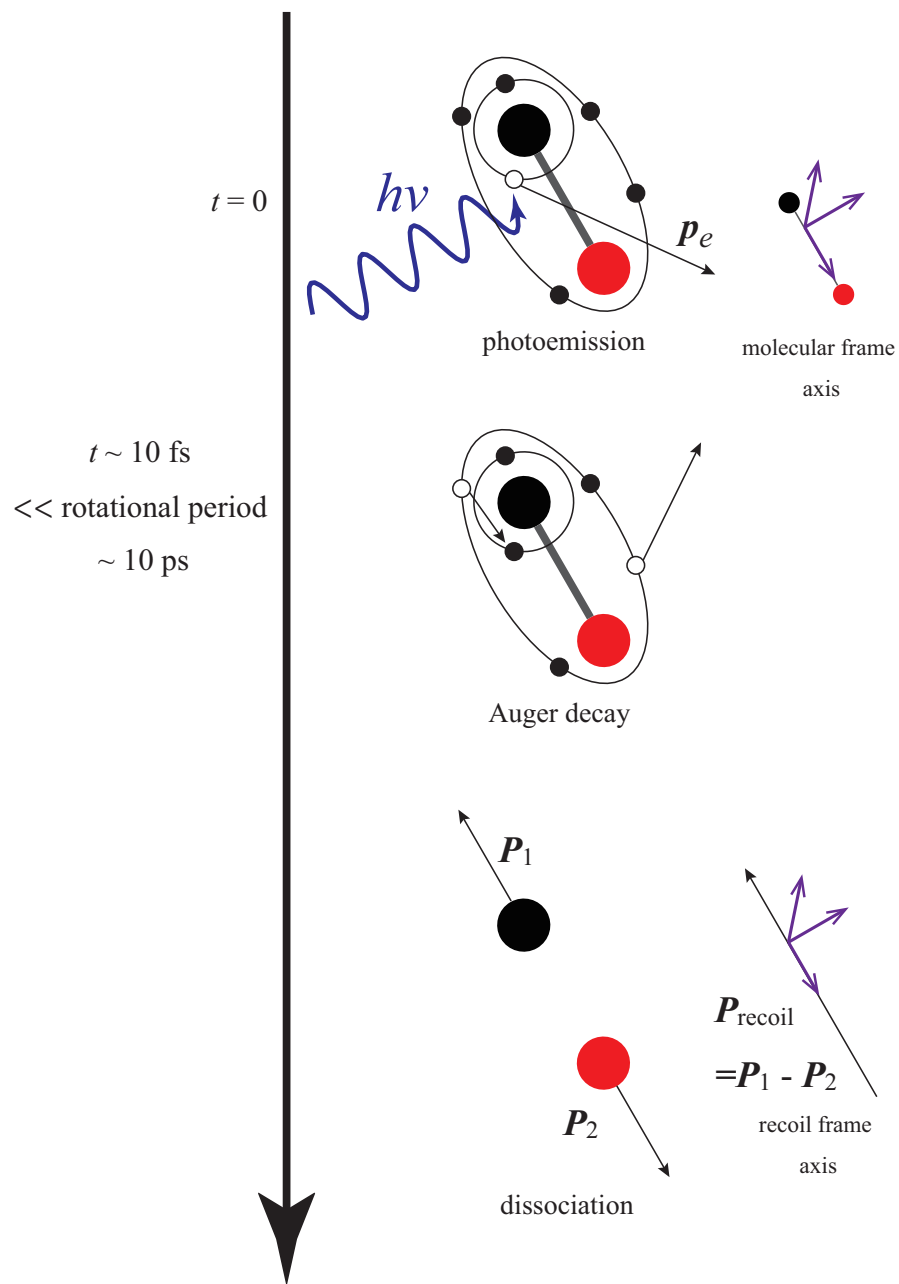
Figure 1.3.1: Concept of RFPAD measurement for two-atomic molecules using the photoelectron–ion coincidence technique. The initial momentum of the photoelectron is measured in coincidence with those of the fragment ions, which give the molecular recoil axis. The recoil axis is regarded as the molecular axis at the instant of photoemission if the entire process takes place within a timescale that is much shorter than the molecular rotational period [54].
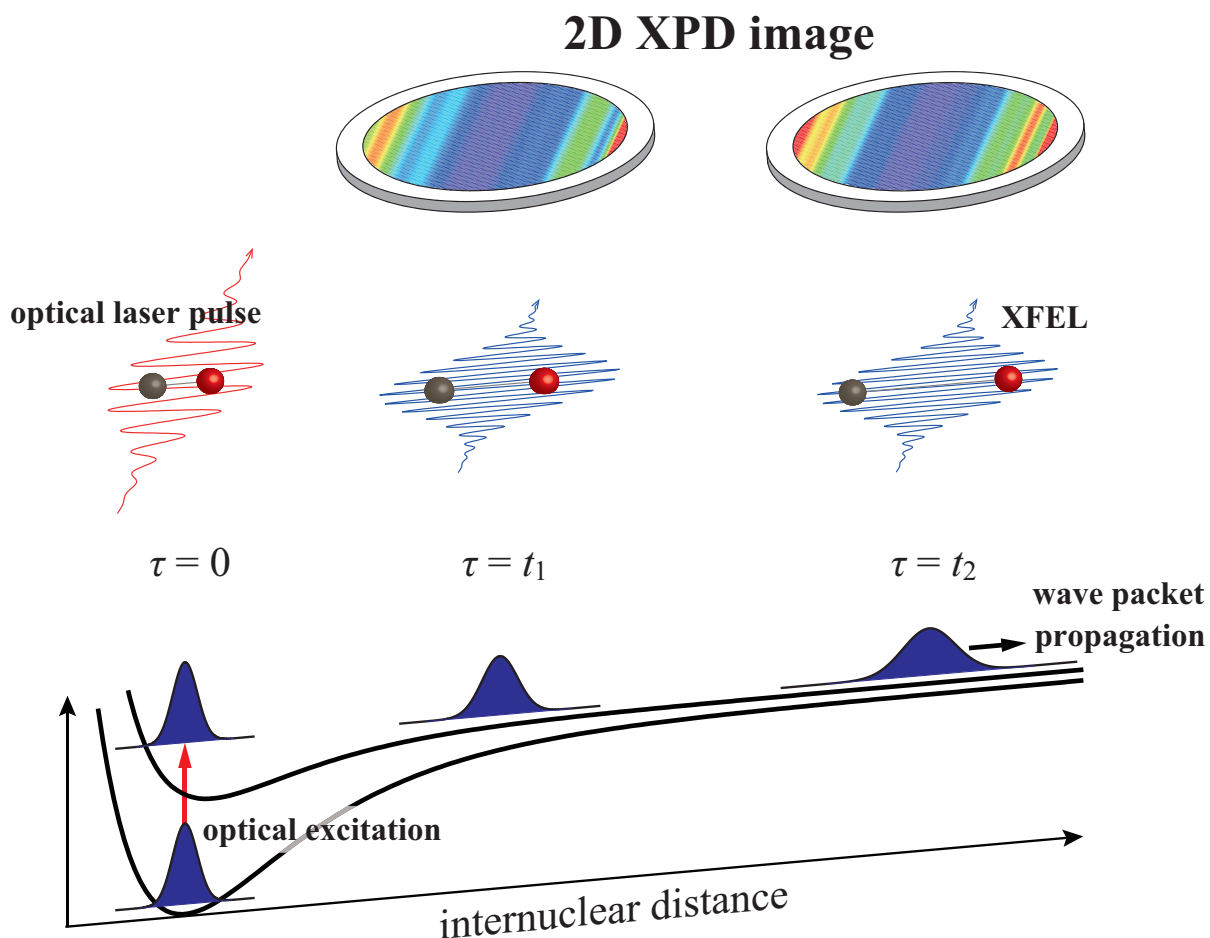
2D XPD image

Figure 1.4.1: Sketch of an optical laser pump–XFEL probe experimental scheme. An optical laser prepares vibrational wave packets on an excited state. Then, they are probed by means of XPD images with XFEL pulses.

conducted for time-resolved XRD [98–102] and time-resolved XPD [78, 103–112]. Recently, Glownia *et al.* succeeded in observing nuclear wave packets by using time-dependent XRD [113] (as did Yang *et al.* by using ultrafast electron diffraction [114]).

Although theoretical studies of time-resolved XRD and XPD are in progress, those that consider the wave packet dynamics of molecular rotation and nuclei are limited [98, 112]. Such studies, involving nonadiabatic dynamics near conical intersections [115, 116], are required for applying time-resolved XRD and XPD to studies of chemical reactions.

1.5   Outline of the thesis

The remainder of this thesis is organized as follows. Chap. 2 describes the MS-XPD theory to calculate the static XPD profile for a certain molecular geometry [39,40]. Chap. 3, which is based

on Refs. [108,109], shows the possibility of extracting molecular structures based on XPD profiles for molecules that are aligned by an Nd:YAG laser field. The proposed theoretical method is successfully applied to the analysis of the recent experimental data of the I_2 molecule [109], in which the elongated I_2 molecular structure in the laser field is identified by a comparison between the simulated and experimental XPD patterns. Chap. 4, which is based on Ref. [117], describes the formulation of XPD from molecules undergoing photochemical reactions induced by optical laser pulses, and subsequent application of the formula to the simulation of time-dependent XPD profiles from both dissociating I_2 molecules and bending CS_2 molecules. The dependence of nuclear wave packet motions on the intensity and shape of the optical laser pulses is examined. Consequently, the XPD simulations based on such nuclear wave packet calculations are observed to exhibit characteristic features, which are compared with the XPD profiles due to the classical trajectories of nuclear motions. Appendix A, which is based on Ref. [118], presents the C $1s$ PADs in coincidence with the CO^+–O^+ fragment ion pairs of CO_2 molecules at photoelectron energies of 85, 120, and 150 eV. The observed left-right asymmetric PADs are well reproduced by our theoretical model by considering the two degenerate zero-point bending vibrations. This leads to a conclusive result on the interpretation of such PADs; although such PADs from polyatomic molecules obtained in the photoelectron–ion coincidence measurement were thus far believed to be in the molecular frame, they are actually in the recoil frame. Appendix B, which is based on Ref. [119], presents the O $1s$ photoelectron angular distributions in coincidence with the CO^+–O^+ fragment ion pairs of CO_2 molecules at photoelectron energies of 90, 120 and 150 eV. The observed RFPADs are left-right asymmetric because of an increase in the bond-breaking probability of the C–O bond involving the O atom with the $1s$ hole, compared with the other C–O bond. A comparison between the experimental data and the calculations based on our semi-empirical model enables us to deduce the value of 1.4 for this increase in the relative bond breaking probability. Finally, Appendix C presents the derivation of the normal coordinate for the two-degenerate bending motions.

Chapter 2

Multiple-scattering XPD theory

By using the same one-electron molecular basis for the initial and final electronic states, the amplitude of core-level photoemission by dipole electron-photon interaction is expressed by $\langle \psi_{\boldsymbol{k}}^-(\boldsymbol{r}_\mathrm{A};\boldsymbol{R})|\hat{e}\cdot\boldsymbol{r}_\mathrm{A}|\phi_c(\boldsymbol{r}_\mathrm{A})\rangle$, where $\psi_{\boldsymbol{k}}^-(\boldsymbol{r}_\mathrm{A})$ denotes the photoelectron wave function of momentum $\boldsymbol{k}$ under the influence of the optical potential; $\phi_c(\boldsymbol{r}_\mathrm{A})$ denotes the wave function of a core orbital localized on the atomic site A; $\hat{e}$ denotes the polarization vector of the incident light; and $\boldsymbol{R}$ denotes the position vectors of the nuclei. One can assume that the photoelectron wave function $\psi_{\boldsymbol{k}}^-(\boldsymbol{r}_\mathrm{A})$ depends on a transient molecular structure owing to the nuclear Coulomb field and electron-electron interaction in the vicinity of the molecule. By using the site-t matrix expansion of $\psi_{\boldsymbol{k}}^-(\boldsymbol{r}_\mathrm{A})$ [39], the photoemission amplitude can be expressed as the multiple-scattering series

$$\langle \psi_{\boldsymbol{k}}^-(\boldsymbol{r}_\mathrm{A})|\hat{e}\cdot\boldsymbol{r}_\mathrm{A}|\phi_c(\boldsymbol{r}_\mathrm{A})\rangle = Z_0 + Z_1 + Z_2 + \cdots , \tag{2.0.1}$$

where Z_0 denotes the amplitude without scattering from the surrounding atoms (direct term), Z_1 denotes the single-scattering amplitude, Z_2 denotes the double-scattering amplitude, and so on. The direct term Z_0 is written as

$$Z_0 = \langle \phi_{\mathrm{A}\boldsymbol{k}}^-|\hat{e}\cdot\boldsymbol{r}_\mathrm{A}|\phi_c\rangle = \sum_{lm} Y_{lm}(\hat{\boldsymbol{k}})M_{lm,l_cm_c}, \tag{2.0.2}$$

where $\phi_{\mathrm{A}\boldsymbol{k}}^-$ denotes the wave function for the photoelectron with momentum $\boldsymbol{k}$ emitted from an atom A upon absorbing an X-ray, and l and m denote the azimuthal and magnetic quantum numbers, respectively. The photoionization matrix element M_{lm,l_cm_c} excited by linearly

15

polarized X-rays parallel to the z-axis is given by

$$M_{lm,l_cm_c} = \sqrt{\frac{2}{\pi}}i^{-l}e^{i\delta_l^{\mathrm{A}}}\int r_{\mathrm{A}}^2 dr_{\mathrm{A}} R_{\varepsilon l}(r_{\mathrm{A}})r_{\mathrm{A}} R_{nl_c}(r_{\mathrm{A}})$$

$$\times \int d\hat{\boldsymbol{r}}_{\mathrm{A}} Y_{lm}^*(\hat{\boldsymbol{r}}_{\mathrm{A}})\sqrt{\frac{4\pi}{3}}Y_{10}(\hat{\boldsymbol{r}}_{\mathrm{A}})Y_{l_cm_c}(\hat{\boldsymbol{r}}_{\mathrm{A}}), \tag{2.0.3}$$

where δ_l^{A} denotes the phase shift of the l-th partial wave at site A, and $R_{\varepsilon l}(r_{\mathrm{A}})$ and $R_{nl_c}(r_{\mathrm{A}})$ denote the radial part labeled by the angular momentum quantum numbers of (l, m) and (l_c, m_c) for $\phi_{\mathrm{A}\boldsymbol{k}}^-$ and ϕ_c, respectively. The integral of the angular part yields the angular momentum selection rule of the photoionization. The single-scattering term Z_1 is explicitly written as

$$Z_1 = \sum_{\alpha(\neq\mathrm{A})} \langle \phi_{\boldsymbol{k}}^0 | t_\alpha g_{\mathrm{A}}\hat{\boldsymbol{e}}\cdot\boldsymbol{r}_{\mathrm{A}} | \phi_c \rangle$$

$$= \sum_{\alpha(\neq\mathrm{A})} e^{-i\boldsymbol{k}\cdot\boldsymbol{R}_{\alpha\mathrm{A}}} \sum_{lm,l'm'} Y_{l'm'}(\hat{\boldsymbol{k}})t_{l'}^\alpha(k)G_{l'm',lm}(k\boldsymbol{R}_{\alpha\mathrm{A}})M_{lm,l_cm_c}, \tag{2.0.4}$$

where $\phi_{\boldsymbol{k}}^0$ denotes the plane wave, and $\boldsymbol{R}_{\alpha\mathrm{A}}$ denotes the position vector of the scatterer α measured from the photoelectron emitter A. Further, g_{A} is expressed by Green's function g_0 and site-t matrix t_{A} : $g_{\mathrm{A}} = g_0 + g_0 t_{\mathrm{A}} g_0$ (see Fig. 2.0.2) [40, 77]. The angular momentum representation of site-t matrix t_l^α at site α due to the phase shift $\delta_l^\alpha(k)$ is given as

$$t_l^\alpha(k) = -\frac{\exp[2i\delta_l^\alpha(k)] - 1}{2ik}. \tag{2.0.5}$$

The propagator

$$G_{l'm',lm}(k\boldsymbol{R}_{\alpha\mathrm{A}}) = -4\pi ik \sum_{l''m''} i^{l''} h_{l''}^{(1)}(kR_{\alpha\mathrm{A}})Y_{l''m''}(\hat{\boldsymbol{R}}_{\alpha\mathrm{A}})\int d\hat{\boldsymbol{r}} Y_{lm}^*(\hat{\boldsymbol{r}})Y_{l'm'}(\hat{\boldsymbol{r}})Y_{l''m''}(\hat{\boldsymbol{r}}), \tag{2.0.6}$$

where $h_{l''}^{(1)}(kR_{\alpha\mathrm{A}})$ is the spherical Hankel function of the first kind [120] and, describes electron propagation from site A with (l, m) to site α with (l', m') [39, 78]. By introducing $X = tG$, we

can obtain the general renormalized multiple-scattering XPD formula [39, 40, 77, 78] as

$$\langle \psi_{\boldsymbol{k}}^{-}(\boldsymbol{r}_{\mathrm{A}}) | \hat{\boldsymbol{e}} \cdot \boldsymbol{r}_{\mathrm{A}} | \phi_c(\boldsymbol{r}_{\mathrm{A}}) \rangle = \sum_{\alpha} e^{-i\boldsymbol{k} \cdot \boldsymbol{R}_{\alpha \mathrm{A}}} \sum_{lm,l'm'} Y_{l'm'}(\hat{\boldsymbol{k}}) \{1 + X + X^2 + X^3 + \cdots\}_{l'm',lm}^{\alpha \mathrm{A}} M_{lm,l_cm_c}$$

$$= \sum_{\alpha} e^{-i\boldsymbol{k} \cdot \boldsymbol{R}_{\alpha \mathrm{A}}} \sum_{lm,l'm'} Y_{l'm'}(\hat{\boldsymbol{k}}) \{[1 - X]^{-1}\}_{l'm',lm}^{\alpha \mathrm{A}} M_{lm,l_cm_c},$$

$$(2.0.7)$$

$$X_{lm,l'm'}^{\alpha\beta} = (1 - \delta^{\alpha\beta}) t_l^{\alpha}(k) G_{l'm',lm}(k\boldsymbol{R}_{\alpha\beta}), \qquad (2.0.8)$$

where X denotes a square matrix in which a matrix element is labeled by a set of atomic sites (A, α, β, ...) in a molecule as well as the pair of angular momentum numbers (l, m) (see Fig. 2.0.1). The dimension of the matrix is $N(l_{\max} + 1)^2$ for a molecule having N atoms and a maximum angular momentum of $l_{\max}$. Full multiple scattering is taken into account by use of the inverse matrix $(1 - X)^{-1}$. Thus, we can obtain an XPD profile $d\sigma(\boldsymbol{R})/d\hat{\boldsymbol{k}}$ by carrying out calculations of the MS-XPD formula:

$$\frac{d\sigma}{d\hat{\boldsymbol{k}}}(\boldsymbol{R}) \propto |\langle \psi_{\boldsymbol{k}}^{-}(\boldsymbol{r}_{\mathrm{A}}; \boldsymbol{R}) | \hat{\boldsymbol{e}} \cdot \boldsymbol{r}_{\mathrm{A}} | \phi_c(\boldsymbol{r}_{\mathrm{A}}) \rangle|^2. \qquad (2.0.9)$$
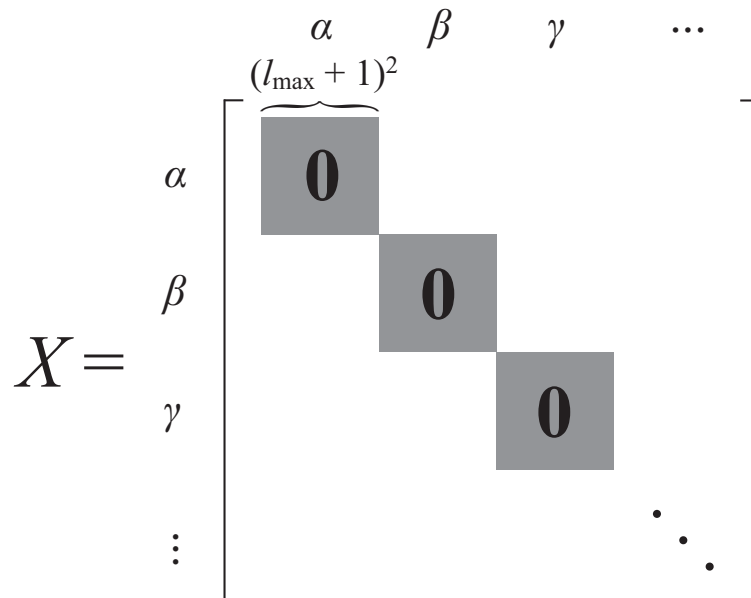
Figure 2.0.1: Graphical representation of the super matrix X. It is an $[N \times (l_{max} + 1)^2]$th-order square matrix, where N is the number of atoms. The indices of $\alpha, \beta, \gamma, \cdots$, denote a set of atomic sites. The diagonal elements are zero because the photoelectrons should propagate to other atomic sites.
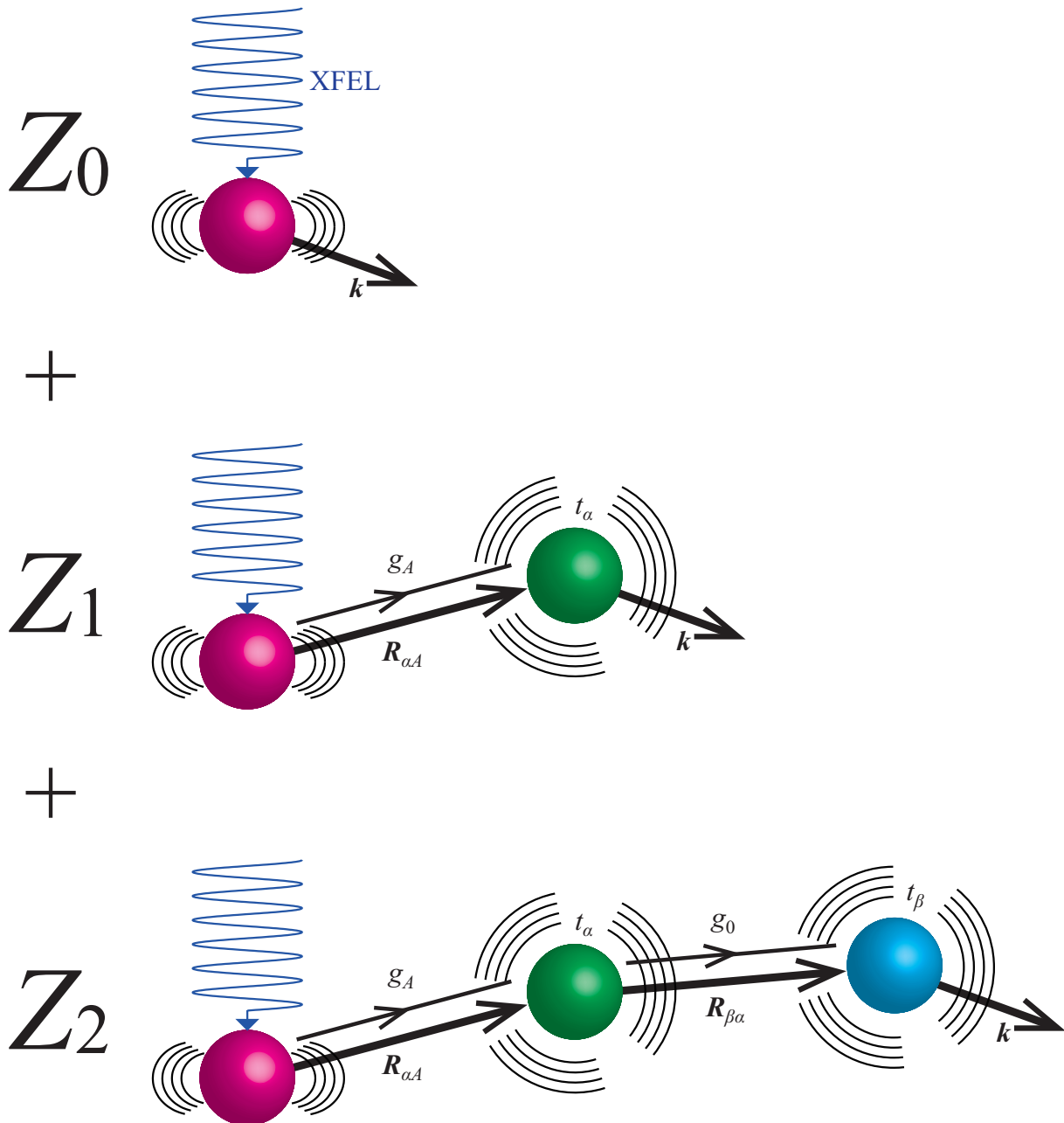
Figure 2.0.2: Pictorial representations of the multiple-scattering series of Z_0, Z_1, and Z_2 (see text for abbreviations).

As can be understood from the above discussion, the XPD profile contains information on the molecular structure through the position vectors of $\boldsymbol{R}_{\alpha\beta}$ in the MS-XPD calculations. In other words, in this work, such a molecular structure, which is defined by a set of positions for atomic sites (A, α, β, ...), is described by a muffin-tin potential. A schematic of the one-dimensional (1D) muffin-tin potential for a triatomic molecule is shown in Fig. 2.0.3. In general, the muffin-tin constant is different from the vacuum level. Therefore, the photoelectron energy experienced

in the molecular region, E_p, is described by $E_p = \varepsilon_p + V_0$, where ε_p denotes the kinetic energy of the photoelectron measured from the vacuum level, and V_0 denotes the energy between the vacuum level and the muffin-tin constant. We evaluated the muffin-tin radii and muffin-tin zero energy of V_0 from each of the atomic potentials $-Z/r + V_{\mathrm{HF}}$, where the center-of-gravity energy for V_{HF} was calculated using the Hartree-Fock program of Cowan [121, 122]. Thus, we prepared atomic potentials centered on the emitter atom A and the neighboring atoms to determine the muffin-tin radii and V_0. For the photoelectron emitter A, an atomic potential with a core hole was calculated. The muffin-tin radii and V_0 were determined from the intersection point of these two potentials, as the muffin-tin spheres do not overlap with each other. Although this muffin-tin model potential is very simple, it must be emphasized that for $\varepsilon_p > 100$ eV, the XPD profiles calculated with this approach have been confirmed to reproduce the relevant experimental data adequately [75, 76], and are in good agreement with those obtained by more sophisticated density functional theory calculations [77].
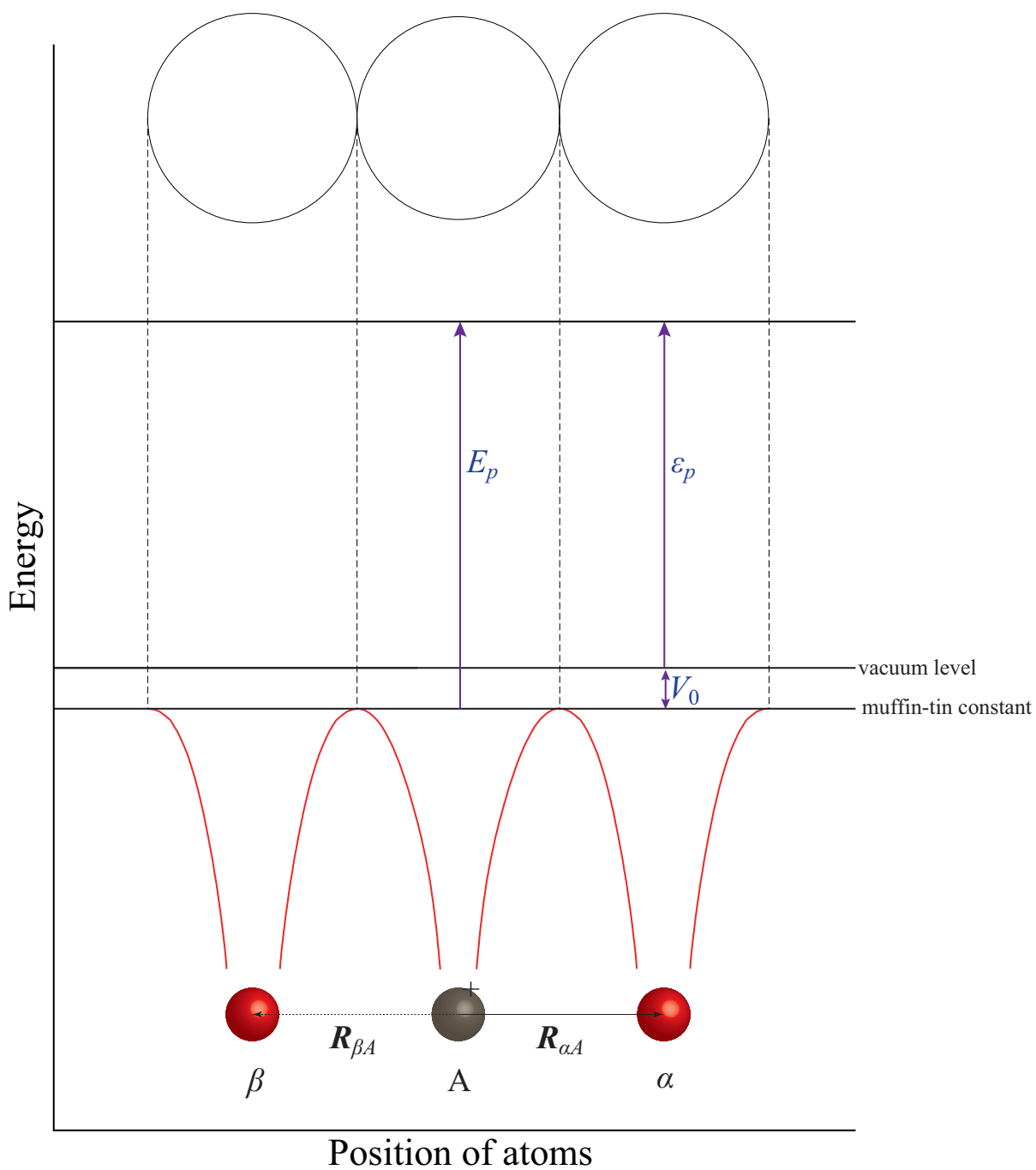
Figure 2.0.3: Muffin-tin potential of a triatomic molecule. ε_p: photoelectron kinetic energy from the vacuum level, V_0: energy between the vacuum level and the muffin-tin constant, and E_p: photoelectron energy in the molecular region.

Chapter 3

Determination of molecular structure in an Nd:YAG laser field

3.1 Introduction

XFELs have considerable potential for determining molecular structures with ångström spatial resolution and for tracing the structural dynamics of molecules and nanoparticles with femtosecond temporal resolution [123]. Over the last decade, groundbreaking experiments on ultrafast X-ray diffraction (UXD) using recently developed femtosecond XFELs, such as the Linac Coherent Light Source [86] at SLAC and SPring-8 Angstrom Compact free electron LAser (SACLA) [88] at SPring-8, have been reported [100, 124–126]. As an alternative to UXD, ultrafast X-ray photoelectron diffraction (UXPD) using XFELs serves as a promising means for investigating femtosecond structural dynamics because the photoionization cross sections of molecules are four to six orders of magnitude greater than those for X-ray scattering. Therefore, the UXPD method extends the time-dependent structure investigations of the UXD method to new classes of samples that are not accessible by any other method, e.g., dilute samples in the gas phase such as aligned, oriented, or conformer-selected molecules. To exploit this capability, several proposals [78, 104, 111] and test experiments [105–108] based on the UXPD methods have been reported. However, results on the transient structure of molecules during chemical reaction, which can be obtained using the UXPD methods, have not yet been reported thus far.

In the UXPD method, the gas-phase molecules must be aligned or oriented in space before the interaction with the XFEL pulses in order to avoid averaging over all possible orientations. In

the pioneering studies on the UXPD method, sample molecules (C_8H_5F [105–107], $C_6H_4Br_2$ [106, 107], and I_2 [108]) were adiabatically aligned by the electric fields of nanosecond Nd:YAG lasers. The reported diffraction profiles for such molecules can be regarded as a snapshot of a "molecular movie" by visualizing the femtosecond structural dynamics in a pump–probe experiment. Here, a fundamental question arises as to whether the structure of a molecule in an intense alignment-laser field is the same as that in its ground state. To answer this question, we applied the UXPD method to a simple I_2 molecule to determine its structure—in other words, its internuclear distance—in the alignment-laser field.

In this Chapter, we report on the profile of I $2p$ photoelectron diffraction from I_2 molecules with a higher degree of alignment compared with our previous work [108], which was obtained using XFEL pulses from SACLA. Owing to the better alignment, we succeeded in determining the average internuclear distance for the I_2 molecular ensemble in alignment Nd:YAG laser fields by applying our molecular structure determination methodology [78] to the newly observed I $2p$ photoelectron diffraction profile. Thus, we established that the internuclear distance of I_2 in the laser field is slightly elongated compared to the equilibrium internuclear distance.

3.2   General formula of PADs

The PAD from a gas of isolated, randomly oriented molecules is of the form

$$\frac{d\sigma}{d\Omega} = \frac{\sigma}{4\pi}[1 + \beta P_2(\cos\theta')], \tag{3.2.1}$$

where σ is the integrated cross section, β is the asymmetry parameter, and θ' is measured from the electric vector of XFEL [46,127]. Further, $P_2(\cos\theta')$ denotes the Legendre polynomial of the second order. On the other hand, if the molecules have a definite orientation, then the angular distribution is described by a different form from that expressed by Eq. (3.2.1). For example, when the molecular axis is parallel to the electric vector of XFEL, the angular distribution in the xz-plane of the molecular frame (see Fig. 3.3.1(b)) is expressed by

$$\frac{d\sigma}{d\Omega} = \frac{\sigma}{4\pi} \sum A_L P_L(\cos\theta), \tag{3.2.2}$$

where the polar angle θ is measured from the molecular z-axis [47,55,128], $P_L(\cos\theta)$ denotes the Legendre polynomial of the Lth order, and the coefficients A_L are calculated from the relevant dipole matrix elements. Owing to the parity selection rule, the summation over L is restricted to even integers for molecules having inversion symmetry (as with the I_2 molecule). When the molecular axis is perpendicular to the electric vector of XFEL, the angular distribution in the xz-plane is written as

$$\frac{d\sigma}{d\Omega} = \frac{\sigma}{4\pi} \sum \left(B_L P_L(\cos\frac{\pi}{2}) + C_L P_L(\cos\frac{\pi}{2})\cos 2\varphi \right), \qquad (3.2.3)$$

where the azimuthal angle φ is measured from the molecular x-axis [47, 55, 128]. Thus, the azimuthal angle distribution is restricted by the conservation of angular momentum projection on the molecular axis for linear molecules. By contrast, the polar angle distribution is dominated by intramolecular photoelectron diffraction. The derivations of Eq. (3.2.2) and (3.2.3) are presented in Appendix 3.9.

Regardless of the degrees of alignment, the polar angle distribution of the XPD profile for linear molecules has the same form as that expressed by Eq. (3.2.2), although the values of the coefficients A_L depend on the degrees of alignment.

3.3 XPD of partially aligned molecules

Consider the photoionization of diatomic molecules in an alignment Nd:YAG laser field with linearly polarized X-ray pulses. The coordinates of the molecular orientation are given by the polar and azimuthal angles of (Θ, Φ) in the laboratory frame (LF), where the polarization direction along the electric field $\boldsymbol{E}$ of the X-ray pulse is taken as the z'-axis and the photon propagation direction $\boldsymbol{q}$ of the pulse is taken as the x'-axis (see Fig. 3.3.1(a)). Hereafter the molecular axis distribution is represented by the function $P(\Theta)$ and the alignment parameter is given by $\left\langle \cos^2\Theta \right\rangle = \int \sin\Theta d\Theta d\Phi \cos^2\Theta P(\Theta)$ [93]. The molecular axis distribution function $P(\Theta)$ is assumed to be normalized in this section. The differential photoionization cross section for a fixed molecular direction is calculated in the molecular frame (MF), where the molecular axis is taken as the z-axis, and the plane spanned by the molecular axis and the polarization of the electric field $\boldsymbol{E}'$ of the X-ray pulse is taken as the zx-plane (see Fig. 3.3.1(b)). The polarization direction and the photon propagation direction in the MF are given by $\hat{\boldsymbol{E}}' = (-\Theta, 0)$
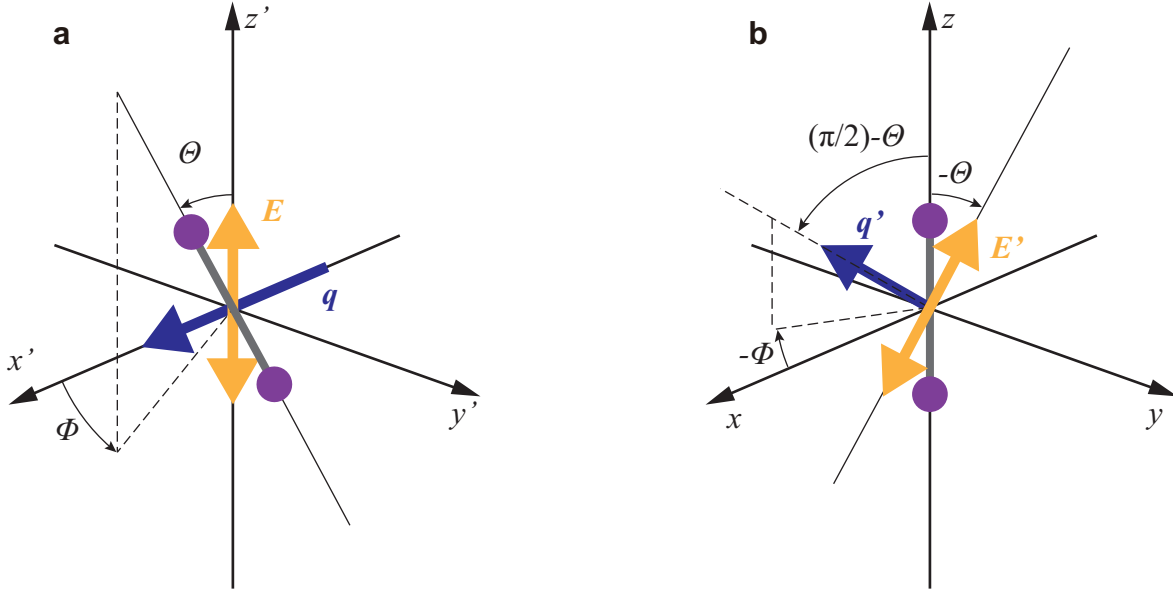
Figure 3.3.1: (a) Laboratory frame (LF) and (b) molecular frame (MF) coordinate systems. The vectors $\boldsymbol{E}$ and $\boldsymbol{q}$ in the LF are the electric field and photon momentum of the X-ray pulse, as is the case for the vectors $\boldsymbol{E}'$ and $\boldsymbol{q}'$ in the MF.

and $\hat{\boldsymbol{q}}' = (\pi/2 - \Theta, \Phi)$, respectively. The orientation of the LF with respect to the MF is characterized by the set of Euler angles

$$R_\gamma = \{0, -\Theta, -\Phi\}. \tag{3.3.1}$$

This causes the MF to be coincident with the LF. The inverse is given by

$$R = R_\gamma^{-1} = \{\Phi, \Theta, 0\}. \tag{3.3.2}$$

Conventions with regard to the Euler angles, rotation matrices, and angular momentum phase factors are the same as those given in Refs. [129, 130].

Hereafter, the electron coordinates $\boldsymbol{r}_A$ and $\boldsymbol{r}'_A$ refer to those in the MF and LF, respectively. The electron photon interaction operator in the dipole approximation is given by

$$\hat{\boldsymbol{e}}' \cdot \boldsymbol{r}'_A = r\sqrt{\frac{4\pi}{3}}Y_{10}(\hat{\boldsymbol{r}}'_A) = r\sqrt{\frac{4\pi}{3}}\sum_{m_\gamma}Y_{1m_\gamma}(\hat{\boldsymbol{r}}_A)D^1_{m_\gamma 0}(R_\gamma) = \hat{\boldsymbol{e}} \cdot \boldsymbol{r}_A. \tag{3.3.3}$$

As explained in Chap. 2, the photoemission amplitude in the MF is given by

$$\langle\psi_{\boldsymbol{k}}^-(\boldsymbol{r}_{\mathrm{A}})|\hat{\boldsymbol{e}}\cdot\boldsymbol{r}_{\mathrm{A}}|\phi_{nl_cm_c}(\boldsymbol{r}_{\mathrm{A}})\rangle = \sum_\alpha e^{-i\boldsymbol{k}\cdot\boldsymbol{R}_{\alpha\mathrm{A}}}\sum_{lm,l'm'}Y_{l'm'}(\hat{\boldsymbol{k}})\{[1-X]^{-1}\}_{l'm',lm}^{\alpha\mathrm{A}}\bar{M}_{lm,l_cm_c}(R_\gamma),$$

(3.3.4)

where

$$\bar{M}_{lm,l_cm_c}(R_\gamma) = \sqrt{\frac{2}{\pi}}i^{-l}e^{i\delta_l^{\mathrm{A}}}\int r_{\mathrm{A}}^2 dr_{\mathrm{A}}R_{\varepsilon l}(r_{\mathrm{A}})r_{\mathrm{A}}R_{nl_c}(r_{\mathrm{A}})$$
$$\times\int d\hat{\boldsymbol{r}}_{\mathrm{A}}Y_{lm}^*(\hat{\boldsymbol{r}}_{\mathrm{A}})\sqrt{\frac{4\pi}{3}}\sum_{m_\gamma}Y_{1m_\gamma}(\hat{\boldsymbol{r}}_{\mathrm{A}})Y_{l_cm_c}(\hat{\boldsymbol{r}}_{\mathrm{A}})D_{m_\gamma0}^1(R_\gamma).$$

(3.3.5)

It should be emphasized that the dipole matrix element in Eq. (2.0.7) for the X-ray pulse polarized along the z-axis is replaced by that for an X-ray pulse polarized along an arbitrary direction. The photoemission amplitude can be simply written in the following form:

$$\langle\psi_{\boldsymbol{k}}^-(\boldsymbol{r}_{\mathrm{A}})|\hat{\boldsymbol{e}}\cdot\boldsymbol{r}_{\mathrm{A}}|\phi_{nl_cm_c}(\boldsymbol{r}_{\mathrm{A}})\rangle = \sum_{l'm'}\bar{C}_{l'm'}(k;R_\gamma)Y_{l'm'}(\hat{\boldsymbol{k}}),$$

(3.3.6)

where

$$\bar{C}_{l'm'}(k;R_\gamma) = \sum_\alpha e^{-i\boldsymbol{k}\cdot\boldsymbol{R}_{\alpha\mathrm{A}}}\sum_{lm}\{[1-X]^{-1}\}_{l'm',lm}^{\alpha M}\bar{M}_{lm,l_cm_c}(R_\gamma)$$

(3.3.7)

and $k = |\boldsymbol{k}|$. The differential photoionization cross section in the MF is given by

$$\frac{d^2\sigma_{nl_cm_c}}{d\boldsymbol{k}dR_\gamma} = 4\pi c\hbar k\alpha\left|\langle\psi_{\boldsymbol{k}}^-(\boldsymbol{r}_{\mathrm{A}})|\hat{\boldsymbol{e}}\cdot\boldsymbol{r}_{\mathrm{A}}|\phi_{nl_cm_c}(\boldsymbol{r}_{\mathrm{A}})\rangle\right|^2$$
$$= 4\pi c\hbar k\alpha\sum_{l'm'}\sum_{\tilde{l}'\tilde{m}'}\bar{C}_{\tilde{l}'\tilde{m}'}^*(k;R_\gamma)\bar{C}_{l'm'}(k;R_\gamma)Y_{\tilde{l}'\tilde{m}'}^*(\hat{\boldsymbol{k}})Y_{l'm'}(\hat{\boldsymbol{k}}),$$

(3.3.8)

where c is the speed of light in vacuum and α is the fine structure constant [131, 132]. With the expansion of products of the spherical harmonics [129, 130],

$$Y_{\tilde{l}'\tilde{m}'}^*(\hat{\boldsymbol{k}})Y_{l'm'}(\hat{\boldsymbol{k}}) = (-1)^{\tilde{m}'}Y_{\tilde{l}'\tilde{m}'}(\hat{\boldsymbol{k}})Y_{l'm'}(\hat{\boldsymbol{k}})$$
$$= (-1)^{\tilde{m}'}\sum_{LM}\sqrt{\frac{(2\tilde{l}'+1)(2l'+1)}{4\pi(2L+1)}}\langle\tilde{l}'0l'0|L0\rangle\langle\tilde{l}'\tilde{m}'l'm'|LM\rangle Y_{LM}(\hat{\boldsymbol{k}}),$$

(3.3.9)

the differential cross section reduces to the simple expansion

$$\frac{d^2\sigma_{nl_cm_c}}{d\boldsymbol{k}dR_\gamma} = \sum_{LM}C_{LM}(k;R_\gamma)Y_{LM}(\hat{\boldsymbol{k}}),$$

(3.3.10)

where

$$C_{LM}(k; R_\gamma) = 4\pi c\hbar k\alpha \sum_{l'm'} \sum_{\tilde{l}'\tilde{m}'} \bar{C}^*_{\tilde{l}'\tilde{m}'}(k; R_\gamma) \bar{C}_{l'm'}(k; R_\gamma)$$
$$\times (-1)^{\tilde{m}'} \sqrt{\frac{(2\tilde{l}'+1)(2l'+1)}{4\pi(2L+1)}} \langle \tilde{l}'0 l'0 | L0 \rangle \langle \tilde{l}'\tilde{m}' l'm' | LM \rangle. \tag{3.3.11}$$

For practical calculations, the expansion coefficient is obtained by the numerical integral of the differential cross section multiplied by the spherical harmonics:

$$C_{LM}(k; R_\gamma) = \int \hat{\boldsymbol{k}} Y^*_{LM}(\hat{\boldsymbol{k}}) \frac{d^2\sigma_{nl_c m_c}}{d\boldsymbol{k} dR_\gamma}. \tag{3.3.12}$$

The photoelectron momentum vector with respect to the LF is related to that with respect to the MF as follows:

$$\boldsymbol{k}' = R_\gamma^{-1} \boldsymbol{k} (= R\boldsymbol{k}). \tag{3.3.13}$$

By substituting the inverse of Eq. (3.3.13), i.e.,

$$\boldsymbol{k} = R^{-1} \boldsymbol{k}' (= R_\gamma \boldsymbol{k}'), \tag{3.3.14}$$

for Eq. (3.3.10), the differential photoionization cross section in the LF is obtained. For a practical calculation to obtain the differential cross section for the photoelectron momentum of $\boldsymbol{k}' = (k, \theta', \phi')$, we first calculate the XPD profile in the MF by Eq. (3.3.4) and obtain the expansion coefficients by Eq. (3.3.12). Then, we also calculate $Y_{LM}(R^{-1}\boldsymbol{k}')$ and substitute them into

$$\frac{d^2\sigma_{nl_c m_c}}{d\boldsymbol{k}' dR_\gamma} = \sum_{LM} C_{LM}(k; R_\gamma) Y_{LM}(R^{-1}\boldsymbol{k}'). \tag{3.3.15}$$

The procedure for obtaining the polar and azimuthal angles as the arguments for the spherical harmonics in Eq. (3.3.15) is as follows. A rotation represented by the Euler angles of $\{\alpha, \beta, \gamma\}$, as shown in Fig. (3.3.2), is expressed by rotations about the initial axes [129, 130]:

$$\tilde{R}(\alpha, \beta, \gamma) = R_Z(\alpha) R_Y(\beta) R_Z(\gamma). \tag{3.3.16}$$

Thus, the components of the photoelectron momentum vectors in the MF and the LF, $\boldsymbol{k}$ and
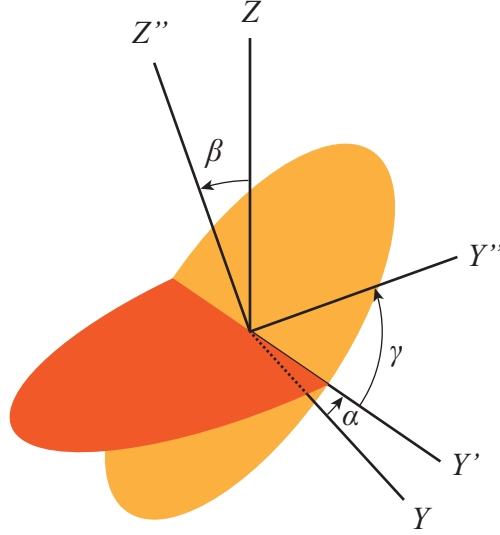
Figure 3.3.2: Euler rotation.

$\boldsymbol{k}'$, are related as

$$
\begin{bmatrix} k_x \\ k_y \\ k_z \end{bmatrix} = \begin{bmatrix} \cos\Theta & 0 & -\sin\Theta \\ 0 & 1 & 0 \\ \sin\Theta & 0 & \cos\Theta \end{bmatrix} \begin{bmatrix} \cos\Phi & \sin\Phi & 0 \\ -\sin\Phi & \cos\Phi & 0 \\ 0 & 0 & 1 \end{bmatrix} \begin{bmatrix} k'_x \\ k'_y \\ k'_z \end{bmatrix}. \tag{3.3.17}
$$

In this manner, the polar and azimuthal angles (θ, ϕ) with respect to the MF, coincident with (θ', ϕ') in the LF, are obtained.

Considering the molecular axis distribution, the weighted sum of the XPD profiles over all the molecular axis directions and the degenerate core orbitals is constructed by

$$
\frac{d\sigma_{nl_c}^{\mathrm{sum}}}{d\boldsymbol{k}'} = \int_0^\pi \sin\Theta d\Theta \int_0^{2\pi} d\Phi P(\Theta) \sum_{m_c=-l_c}^{l_c} \frac{d^2\sigma_{nl_c m_c}}{d\boldsymbol{k}' dR_\gamma}\bigg|_{R_\gamma=\{0,-\Theta,-\Phi\}}. \tag{3.3.18}
$$

For photoionization of a homonuclear diatomic molecule, such as I_2 I $2p$ photoionization in the present study, further correction of Eq. (3.3.18) is necessary. In this case, the differential photoionization cross section for a certain molecular direction is an incoherent superposition of that for the core orbitals localized on the two atomic sites, $\phi_{nl_c m_c}^{\mathrm{L}}$ and $\phi_{nl_c m_c}^{\mathrm{R}}$:

$$
\frac{d^2\sigma_{nl_c m_c}}{d\boldsymbol{k}' dR_\gamma}\bigg|_{R_\gamma=\{0,-\Theta,-\Phi\}} = \frac{d^2\sigma_{nl_c m_c}^{\mathrm{L}}}{d\boldsymbol{k}' dR_\gamma}\bigg|_{R_\gamma=\{0,-\Theta,-\Phi\}} + \frac{d^2\sigma_{nl_c m_c}^{\mathrm{R}}}{d\boldsymbol{k}' dR_\gamma}\bigg|_{R_\gamma=\{0,-\Theta,-\Phi\}}. \tag{3.3.19}
$$

The molecule under consideration has a space inversion symmetry. Thus, for $m_c \neq 0$, the core

orbital $\phi^{\mathrm{L}}_{nl_c m_c}$ for the molecular direction of (Θ, Φ) is related to $\phi^{\mathrm{R}}_{nl_c -m_c}$ for that of $(\pi - \Theta, \Phi + \pi)$ by the space inversion. Therefore, the differential cross section of $d^2\sigma^{\mathrm{L}}_{nl_c m_c}/d\mathbf{k}' dR_\gamma$ for $R_\gamma = \{0, -\Theta, -\Phi\}$ is equivalent to $d^2\sigma^{\mathrm{R}}_{nl_c -m_c}/d\mathbf{k}' dR_\gamma$ for $R_\gamma = \{0, -\pi + \Theta, -\Phi - \pi\}$. Then, the weighted sum of the XPD profiles for the diatomic molecule is corrected as follows:

$$
\begin{aligned}
\frac{d\sigma^{\mathrm{sum}}_{nl_c}}{d\mathbf{k}'} = & \int_0^\pi \sin\Theta d\Theta \int_0^{2\pi} d\Phi P(\Theta) \\
& \times \sum_{\mathrm{L\,and\,R}} \left\{ \frac{d^2\sigma^{\mathrm{L(R)}}_{nl_c 0}}{d\mathbf{k}' dR_\gamma} + \frac{1}{2} \sum_{m_c=1}^{l_c} \left[\frac{d^2\sigma^{\mathrm{L(R)}}_{nl_c m_c}}{d\mathbf{k}' dR_\gamma} + \frac{d^2\sigma^{\mathrm{L(R)}}_{nl_c -m_c}}{d\mathbf{k}' dR_\gamma} \right] \right\} \Big|_{R_\gamma = \{0, -\Theta, -\Phi\}} .
\end{aligned}
\tag{3.3.20}
$$

3.4 Experimental setup and procedure

We will describe the experiment performed by Minemoto *et al.* The details of the experimental procedures are described in the Methods section of Ref. [109]. A pulsed supersonic molecular beam containing sample I_2 was introduced into the interaction region between facing velocity-map imaging spectrometers (VMIs) and was intersected by collinear pulsed lasers (Nd:YAG laser and XFEL) [108] (see Fig. 3.4.1). The 10-ns-long pulses from the Nd:YAG laser adiabatically aligned the I_2 molecules. The polarization vectors of the Nd:YAG laser and the XFEL were parallel to each other along the z-direction, as shown in Fig. 3.4.1. Here, alignment refers to the confinement of a molecular axis along the Nd:YAG laser polarization vector. Electrons produced by the XFEL pulses were accelerated toward one VMI, which was operating in a velocity focusing mode, and then detected by a microchannel plate (MCP) detector backed by a phosphor screen. The two-dimensional (2D) electron images formed on the screen were recorded with a sCMOS camera, and the data acquired for every single XFEL shot were read out by a personal computer (PC). Simultaneously, 2D ion images were measured with the other VMI and a detector system similar to that used for the electrons. From the 2D ion images, the degree of alignment of the I_2 molecules was evaluated. The experiment was performed at the beamline BL3 in the experimental hatch EH4c of SACLA [88,89]. To analyze the XPD profiles within the theoretical framework of a photoelectron diffraction model [78], we selected the photon energy of the XFEL to be 4.7 keV, which is $\sim$140 eV above the ionization threshold of I $2p_{3/2}$ (4.557 keV, Ref. [133]); thus, the kinetic energy ε_p of the I $2p_{3/2}$ photoelectrons was $\sim$140 eV.
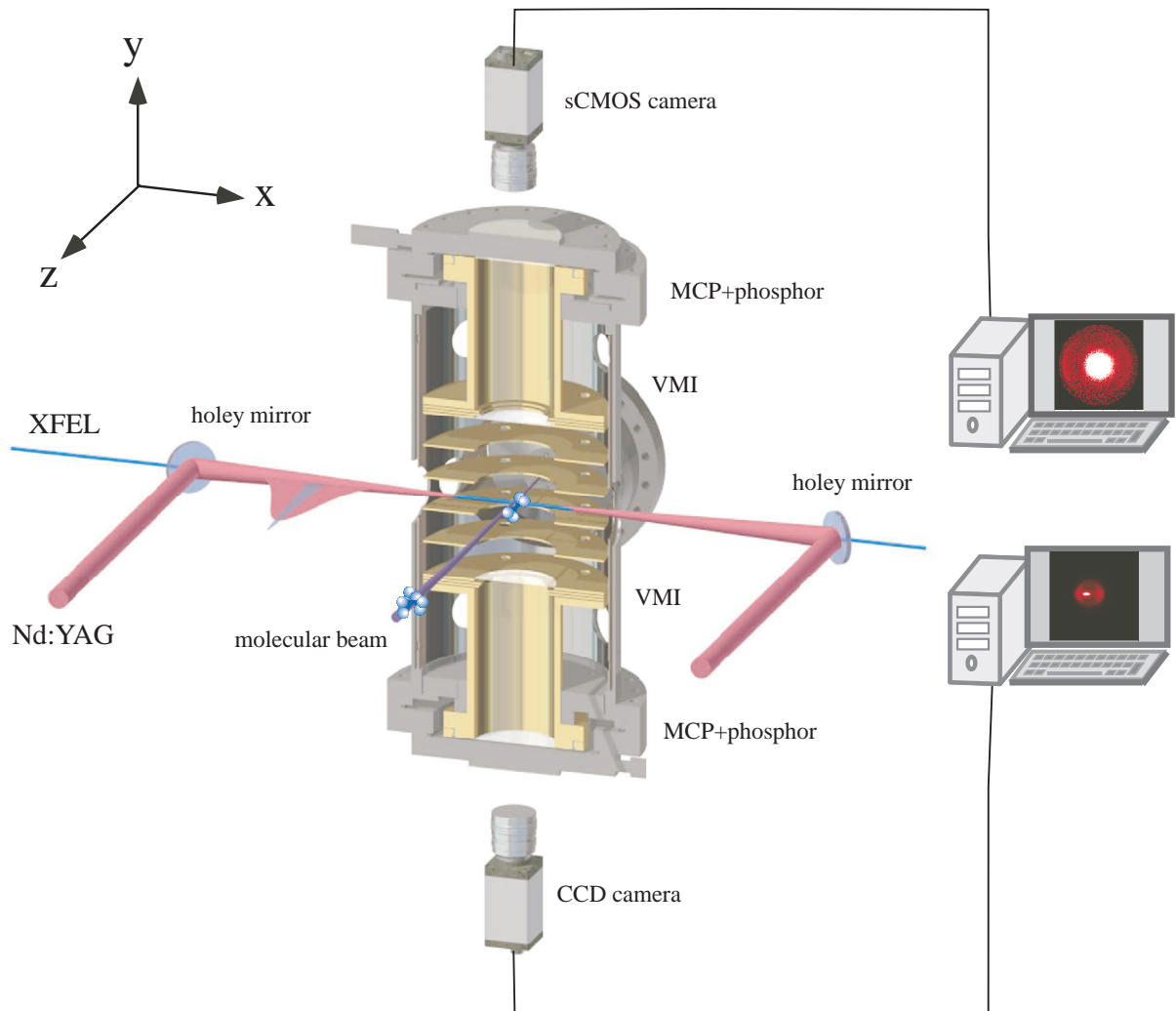
Figure 3.4.1: Schematic of the experimental setup. Two laser beams propagating along the x-axis in a collinear arrangement intersect a supersonic pulsed molecular beam along the z-axis at the center of a vacuum chamber. A Nd:YAG laser is used to adiabatically align the sample I_2 molecules that are probed by the XFEL. XPD images of the photoelectrons are recorded by the upper VMI. The degree of alignment is quantified using the 2D momentum distributions of the ionic fragments, which are registered by the lower VMI. Adapted from Ref. [109].

3.5   Electron and ion images from laser-aligned I_2 molecules

The 2D electron and ion images acquired from the aligned I_2 molecules using the Nd:YAG laser pulses are shown in Fig. 3.5.1(a) and (c), respectively. Each image was obtained by alternative measurements with and without the molecular beam and subtraction of the latter from the former. In the ion image, an intense central spot and an outer ring appear (see Fig. 3.5.1(c)). The central peak is due to both the atomic ions of He^+ in the buffer gas and the molecular ions of I_2^+. The outer ring originates from the Coulomb-exploding fragment ions I^{n+} and is distributed along the polarization direction of the Nd:YAG laser pulses, parallel to the z-axis in Fig. 3.5.1(c). The anisotropic distribution of the fragment ions is due to the alignment of neutral I_2 molecules. Based on a numerical simulation for the 2D ion image, the most probable rotational temperature was estimated to be 5 K and the effective peak intensity of the Nd:YAG laser pulses was 6×10^{11} W/cm^2 in the interaction region. These conditions resulted in a degree of alignment characterized by the alignment parameter [93] $\langle \cos^2 \Theta \rangle = 0.734 \pm 0.003$, where Θ is the angle between the molecular axis and the polarization direction of the Nd:YAG laser. Fig. 3.5.1(d) shows the polar plot of the angular distribution of fragment ions having radii of 5–10 mm, which correspond to the charge states n, where $4 \leq n \leq 6$ (Ref. [108]). The details of the numerical simulation are provided in the Methods section of Ref. [109].

The 2D electron momentum image in Fig. 3.5.1(a) consists of a central part, which originates from low-energy electrons via shake-off processes induced by Auger cascades, and the outer ring, corresponding to I $2p$ photoelectrons. The high kinetic energy ($\sim$140 eV) of the I $2p$ photoelectrons allows distinction between the outer photoelectron ring and the intense low-energy central part. Fig. 3.5.1(b) shows the polar plot of the angular distribution of the I $2p$ photoelectrons (detailed in the Methods section of [109]), which is hereafter referred to as the XPD profile. The XPD profiles of reflection-symmetric molecules, such as the I_2 molecule, that are aligned parallel to the polarization vector of the XFEL pulse can be expressed by a series of even-order Legendre polynomials $P_n(\theta)$ (Refs. [47, 110, 128]), where θ is the photoelectron ejection direction with respect to the molecular axis. In fact, the measured XPD profile is well reproduced by the Legendre polynomials of up to the sixth order (see Fig. 3.5.1(b)). The contributions of higher-order Legendre polynomials, which are responsible for the fine structure expected in the XPD profile, are smeared out owing to the imperfect alignment of the sample molecules. However, because of the higher degree of alignment of $\langle \cos^2 \Theta \rangle = 0.734 \pm 0.003$
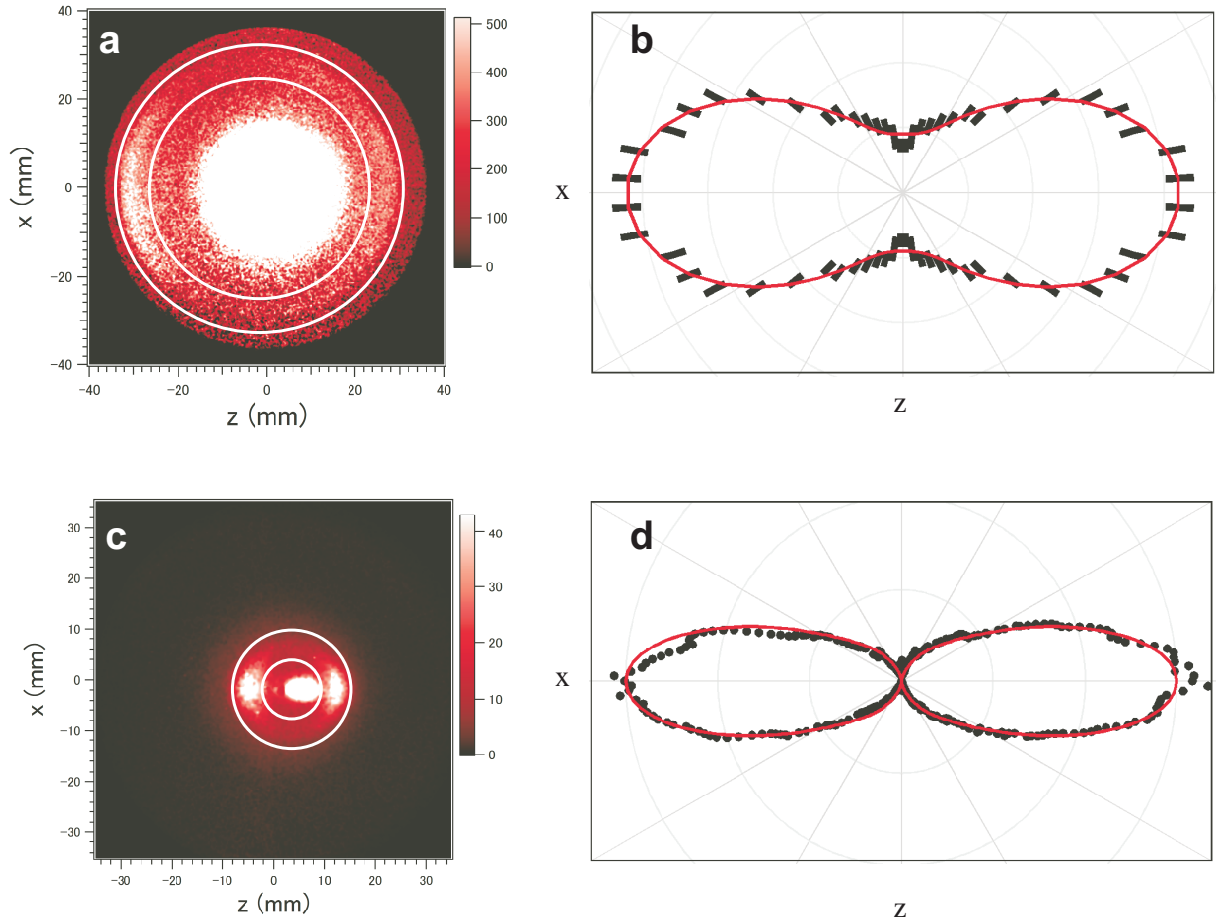
Figure 3.5.1: 2D momentum images of electrons and ions and their polar plots. (a) I $2p$ photo-electron image. The white circles indicate radii of 26 and 30.5 mm to distinguish the central-ring image of low-energy electrons. (b) I $2p$ XPD profile expressed as a polar plot. The short bars denote the statistical errors in the experimental data, and the solid curve represents the fitted result of the Legendre polynomials of $F(\theta) \approx P_0(\theta) + 1.49P_2(\theta) + 0.31P_4(\theta) + 0.24P_6(\theta)$. (c) Fragment-ion image indicating that the molecular axis distributions are aligned along the polarization vector of the Nd:YAG laser parallel to the z-axis. The white circles correspond to radii of 5 and 10 mm. (d) Molecular axis distributions expressed as a polar plot. The dots represent the experimental data, in which the background has been eliminated from the raw image and the solid curve $P(\Theta) = \cos^2\Theta + 1.82\cos^{12}\Theta$ represents the result of the numerical simulation. Adapted from Ref. [109].

compared to that of 0.61 ± 0.03 achieved in Ref. [108], the intensity minima in the XPD profile are observed in directions perpendicular to the polarization vector of the Nd:YAG laser, although the fine structure due to photoelectron diffraction, as will be shown later, cannot be resolved. The improved XPD profile motivated us to analyze our new results on the basis of multiple-scattering XPD (MS-XPD) theory [78] in order to extract the molecular structure of I_2 in the 10-ns-long adiabatic alignment Nd:YAG laser field.

3.6   Simulated XPD profiles

Now, we discuss how the MS-XPD theory enables us to interpret the observed XPD results. Because the $2p$ state is triply degenerate, we consider the photoemission from the $2p_z$ orbital to be aligned along the molecular axis and that from the $2p_x$ ($2p_y$) orbital to be aligned along the x-axis (y-axis) orthogonal to the molecular axis. The theoretical results for the XPD, which were calculated for light polarization along the molecular axis, are depicted as polar plots in the xz-plane in Fig. 3.6.1 (i.e., XPD from the $2p_z$ orbital: Fig. 3.6.1(b), that from the $2p_x$ orbital: Fig. 3.6.1(c), and their sum: Fig. 3.6.1(a)). Here, we take an incoherent superposition of XPD from both the left and the right I atoms. As can be seen in Fig. 3.6.1(a), the difference between XPD by full multiple-scattering calculation and that by single-scattering calculation is small. This implies that at a photoelectron energy of 140 eV, the single-scattering effect predominates over XPD, as reported in the literature [75–78].

To elucidate the interference effect in XPD, the results of the computational experiment for the single-scattering approximation, $|Z_0 + Z_1|^2 = |Z_0|^2 + |Z_1|^2 + 2\Re(Z_0^* Z_1)$, are shown in Fig. 3.6.1(d,e). For the polarization geometry corresponding to light polarized along the molecular axis, the photoionization of the $2p_z$ orbital creates both s- and d_{z^2}-partial waves in the local region of the emitter's atomic site, owing to the dipole selection rule. However, in Fig. 3.6.1(d), the primary photoemission amplitude, $|Z_0|^2$, exhibits the specific shape of the angular function of $d_{z^2} : Y_{20}(\theta, \phi)$, where Y_{20} is a spherical harmonic. This is because the minor component of the s-partial wave makes a negligible contribution, i.e., the magnitude of the dipole radial integral $\int r_A^2 dr_A R_{\varepsilon l}(r_A) r_A R_{21}(r_A)$ in Eq. (3.3.5) for the s-partial wave ($l = 0$) is 100 times smaller than that for d-partial wave ($l = 2$). However, it should be noted that the interference term between s- and d-partial waves, which depends on the phase difference of $\delta_2^A - \delta_0^A$, contributes to the primary photoemission amplitude. Because the neighboring atom lies in the preferential direction of
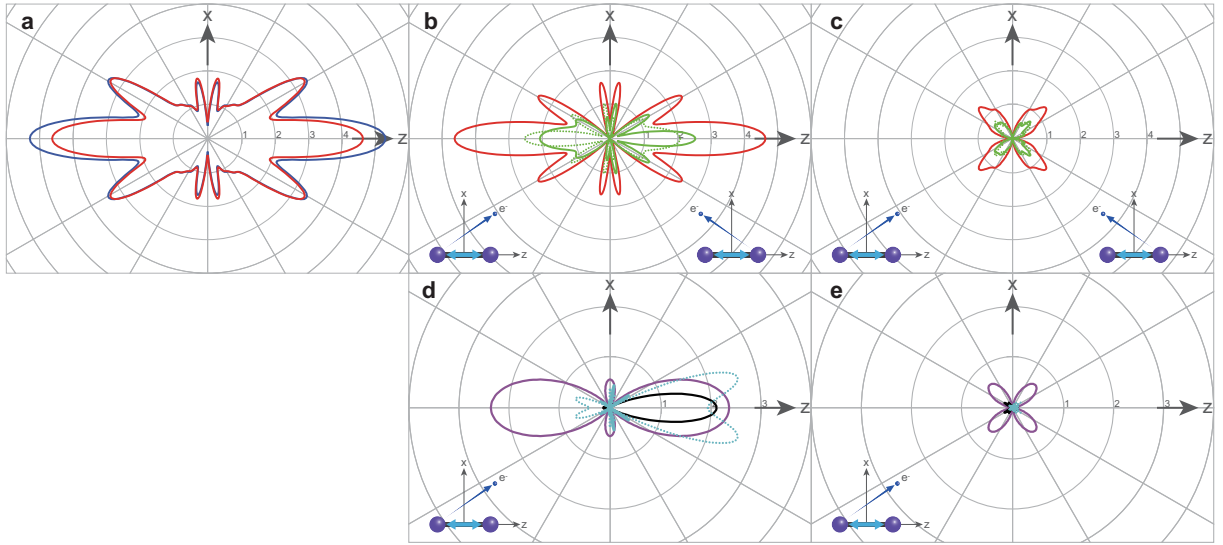
Figure 3.6.1: Calculated I $2p$ XPD patterns. (a) Blue curve: full multiple-scattering calculation; red curve: single-scattering calculation. (b) The green bold and dotted curves are the $2p_z$ XPD patterns from the left and right I atoms under the single-scattering approximation, respectively. The red curve is an incoherent superposition of the two XPD patterns. (c) Same as (b) but for the $2p_x$ XPD pattern. (d) Purple curve: primary photoemission amplitude from the $2p_z$ patterns in the left I atom, $|Z_0|^2$; black curve: single-scattering amplitude, $|Z_1|^2$; and light-blue curve: interference term of $2\Re(Z_0^* Z_1)$ (with positive values expressed by the bold curve and negative values expressed by the dotted curve). (e) Same as (d) but for the $2p_x$. In (e), the black curve for $|Z_1|^2$ and the light-blue curve for $2\Re(Z_0^* Z_1)$ are barely visible. The insets show the polarization geometry, in which the double-headed arrow indicates the polarization vector of the XFEL. Adapted from Ref. [108].

primary photoemission, the appreciable amplitude, $|Z_1|^2$, of the wave scattered by the atom is observed in the forward direction. Thus, a strong interference effect, $2\Re(Z_0^* Z_1)$, can be expected between the primary photoelectron and the scattered waves. In fact, $2\Re(Z_0^* Z_1)$ strongly modulates the shape of $|Z_0 + Z_1|^2$ (see Fig. 3.6.1(b,d)). On the other hand, the photoionization of the $2p_x$ orbital produces a d_{xz}-partial wave at the emitter's atomic site. This is obvious from Fig. 3.6.1(e): the primary photoemission amplitude, $|Z_0|^2$, exhibits the characteristic shape of the angular function of d_{xz}: $(Y_{2-1}(\theta, \phi) - Y_{21}(\theta, \phi))/\sqrt{2}$. In this case, because the neighboring atom resides on the angular node of $|Z_0|^2$, the amplitude, $|Z_1|^2$, of the wave scattered by this atom is quite small: it is barely visible in Fig. 3.6.1(e). Consequently, the interference effect, $2\Re(Z_0^* Z_1)$, between the primary photoelectron and scattered waves appears weakly in the $2p_x$ photoionization (see Fig. 3.6.1(c,e)). Computational experiments were performed to examine the sensitivity of the XPD profiles to the molecular structure. We calculated the XPD profiles by changing the internuclear distances for partially and fully aligned molecules. The profiles for partially aligned molecules are those averaged by the axis distribution expressed by $\langle \cos^2 \Theta \rangle = 0.61 \pm 0.03$, which was achieved in the previous experiment [108]. These results are shown in Fig. 3.6.2. Although the $2p_x$ XPD profile is not sensitive to the internuclear distance owing to the small scattering effect, the total XPD profiles from fully aligned molecules are sensitive to small changes in the internuclear distance of ± 0.5 Å(see Fig. 3.6.2(b)). On the other hand, the XPD profiles averaged by the axis distribution are not particularly sensitive to such small changes in the internuclear distance (see Fig. 3.6.2(a)). Thus, it can be concluded that to definitively determine a molecular structure from a measured XPD profile, a higher degree of alignment of sample molecules is necessary. In other words, the XPD patterns exhibiting interference profiles, which would be measurable for highly aligned molecules, are essential for the application of our molecular-structure-determination methodology, see Ref. [78].

To demonstrate XPD profile dependence on polarization geometries, the XPD profiles dependent on the polarization geometries weighted by the experimentally obtained molecular axis distribution function of $P(\Theta) = \cos^2 \Theta + 1.82 \cos^{12} \Theta$ for the present study as well as their weighted sum are shown in Fig. 3.6.3. Fig. 3.6.3(a) shows the measured XPD profile relative to the polarization vector of the XFEL. Each component of the observed XPD profile, which is illustrated in Fig. 3.6.3(b), depends on the molecular axis because the polarization vector is fixed in the present experimental geometry. As expected, the molecular axis distributions
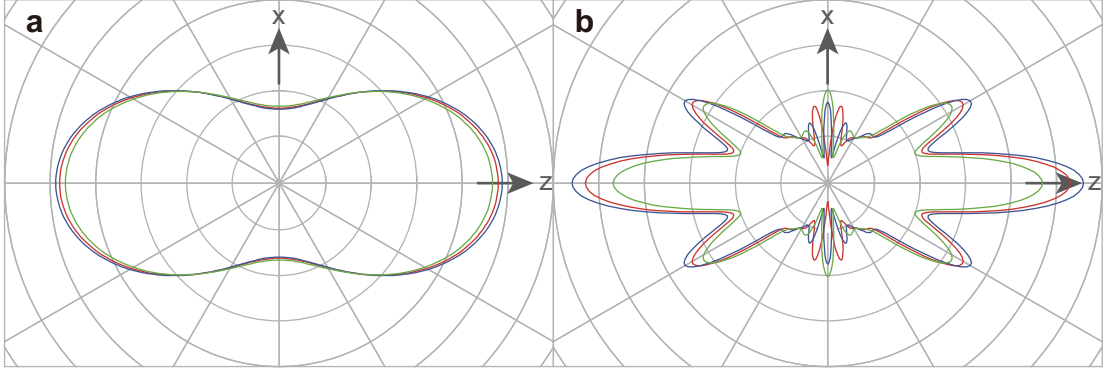
Figure 3.6.2: I $2p$ XPD patterns depending on internuclear distances. Patterns for (a) $\langle \cos^2 \Theta \rangle =$ 0.61 and (b) $\langle \cos^2 \Theta \rangle = 1$. Red curves: equilibrium internuclear distance of 2.666 Å; blue curves: internuclear distance of $(2.666 + 0.5)$ Å; and green curves: internuclear distance of $(2.666 - 0.5)$ Å. Adapted from Ref. [108].

strongly affect the measured XPD profiles. In the extreme case of a fully random alignment, the XPD profiles cannot be measured but the PADs can be observed relative to the polarization vector of the X-rays.

3.7 Molecular structure determination

We employed the muffin-tin approximation for molecular potentials, which considers spherical scattering potentials centered on each atom and a constant value in the interstitial region between atoms (as detailed in Chap. 2). In this model, the photoelectron energy in the molecular region, E_p, is expressed as $E_p = \varepsilon_p + V_0$, where ε_p is the photoelectron kinetic energy measured from the vacuum level, and V_0 is the energy between the vacuum level and the muffin-tin constant. For a given muffin-tin potential—in other words, a certain molecular geometry—we can calculate an XPD profile within the framework of our MS-XPD theory [78] for a given polarization geometry, in which the photoelectron energy E_p and the internuclear distance $R_{\text{I-I}}$ are free parameters. The central photon energies of XFEL pulses fluctuate shot-by-shot, but their standard deviation is much smaller than the bandwidth ΔE (0.5%) at the photon energy of $E = 4.7$ keV [89]. Thus, owing to this bandwidth of $\Delta E \sim 24$ eV, the photoelectron peak with the mean energy of $\varepsilon_p \sim 140$ eV has a width of $|\pm \Delta E/2| \times 2 \sim 24$ eV (full width at half maximum; FWHM). For convenience, we define a parameter range, ΔE_a, for the photon energy, $E = V_0 + \varepsilon_a$, as $\Delta E_a = V_0 \pm \Delta E$. Under this definition, the parameter range of ΔE_a covers the possible range for the muffin-tin zero energy of V_0.
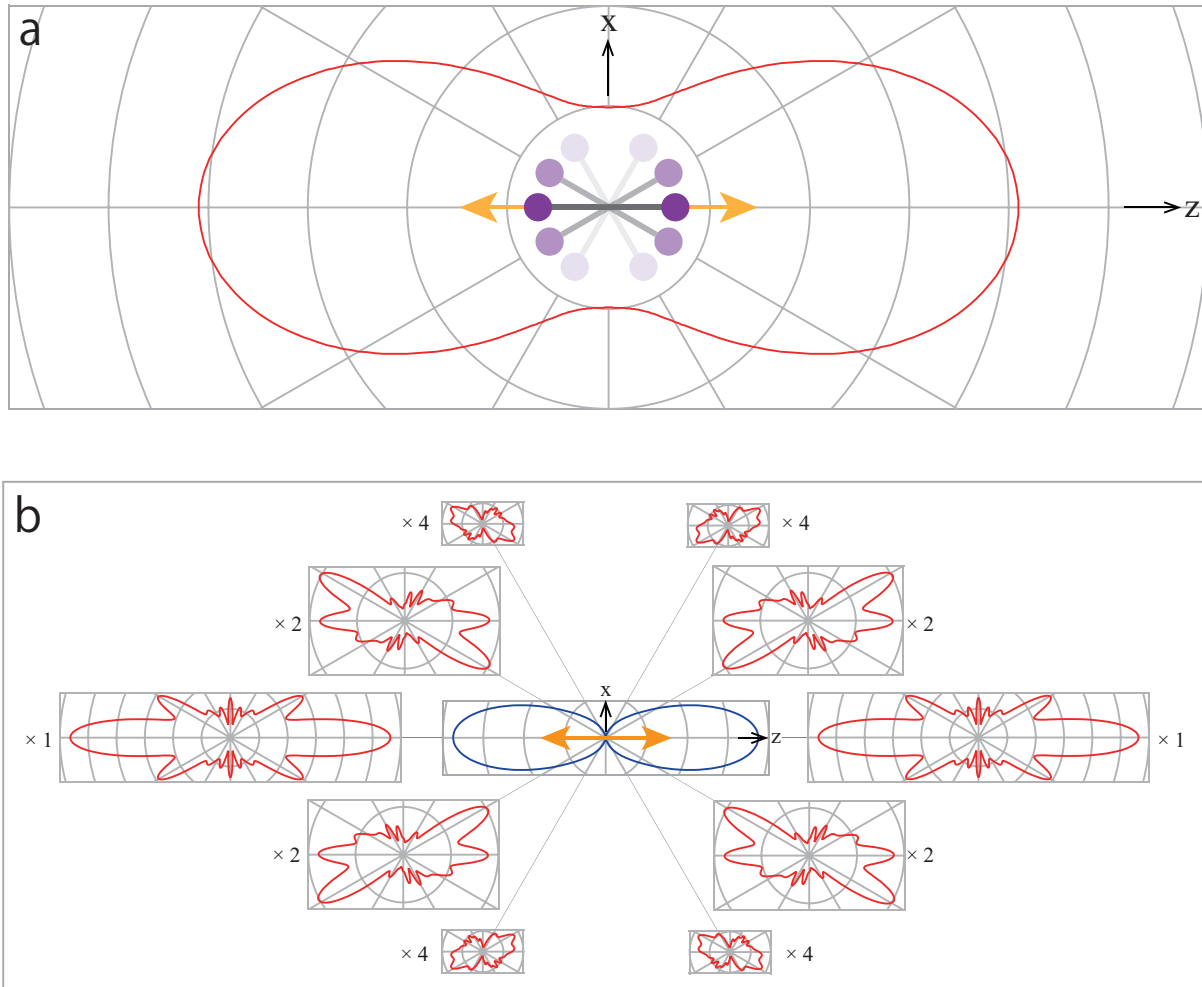
Figure 3.6.3: XPD profile integrated over the molecular axis distributions (a) and its decompositions (b). In (a), the reference axis of the XPD profile is the polarization vector of the XFEL, which is indicated by the double headed arrow. In (b), the central polar plot expresses the molecular axis distribution $P(\Theta) = \cos^2 \Theta + 1.82 \cos^{12} \Theta$. The decomposed XPD profiles exhibit dramatic changes depending on the geometries of the polarization vector of the X-rays and the molecular axis. The numbers on the left and right sides of the figures stand for the respective linear magnifications. Adapted from Ref. [109].

In general, the XPD profiles are controlled by both the kinematical parameters of the polarization geometries and the dynamical parameters of E_p and $R_{\mathrm{I-I}}$. The former are given, whereas the latter are retrieved by the following procedure. First, we calculated the profiles for all geometries by using the set of two dynamical parameters, and we constructed their weighted sum by considering the axis distribution of the sample I_2 molecules (detailed in the Methods section of [109]). Finally, the weighted sum of the XPD profiles was convoluted over the experimental acceptance angles (in plane, $\pm 3°$; out of plane, $\pm 20°$) for the I $2p$ photoelectrons. To retrieve the internuclear distance information from the XPD profile calculated by this procedure, we performed a "trial-and-error" iterative procedure involving a comparison of the experimental XPD profile, $I_{\mathrm{exp}}(\theta)$, with the theoretical ones, $I_{\mathrm{theor}}(\theta)$, given by the set of two parameters, E_p and $R_{\mathrm{I-I}}$. The quality of the fit between the experiment and the theory was evaluated by the reliability factor, or R-factor [78], defined as

$$R = \frac{\sum_\theta [I_{\mathrm{theor}}(\theta) - I_{\mathrm{exp}}(\theta)]^2}{\sum_\theta [I_{\mathrm{theor}}(\theta) + I_{\mathrm{exp}}(\theta)]^2}. \tag{3.7.1}$$

The intensities I_{theor} and I_{exp} are normalized so that the area of each XPD profile is unity. Because $R = 0$ corresponds to perfect agreement, we determined the minimum value of the R-factor to obtain the best solution for the internuclear distance. The R-factor map as a function of the two parameters is shown within interesting parameter ranges of ΔE_a and $(\Delta R_{\mathrm{I-I}})$ in Fig. 3.7.1(a). The area (A) surrounded by the solid curve indicates the valley of the R-factor map. Thus, the best solution for the deviation $((\Delta R_{\mathrm{I-I}}))$ from the equilibrium internuclear distance of 2.666 Åranges from 0.18 to 0.30 Å, i.e., the internuclear distance is elongated by 0.18 to 0.30 Å. Corresponding to this best solution ΔE_a ranges from 45 to 55 eV. By referring to the value of $V_0 = 23$ eV roughly evaluated by us (see the Method section of [109]), $\Delta E \sim +25$ eV is obtained, which is comparable to the bandwidth of the photoelectron peak. Considering both the ambiguity of the V_0 value and the photoelectron energy spread, the best solution of $\Delta E_a \sim 50$ eV is rationalized. To illustrate the quality of the fit, the XPD profiles for the minimum and maximum values of the R-factor are shown in Fig. 3.7.1(b) along with the experimental data. The best-fitted curve reproduces the minima of the experimental XPD profile in the vertical direction. By contrast, the worst-fitted curve reproduces the maxima in the vertical direction. It is not surprising that one cannot observe prominent differences between
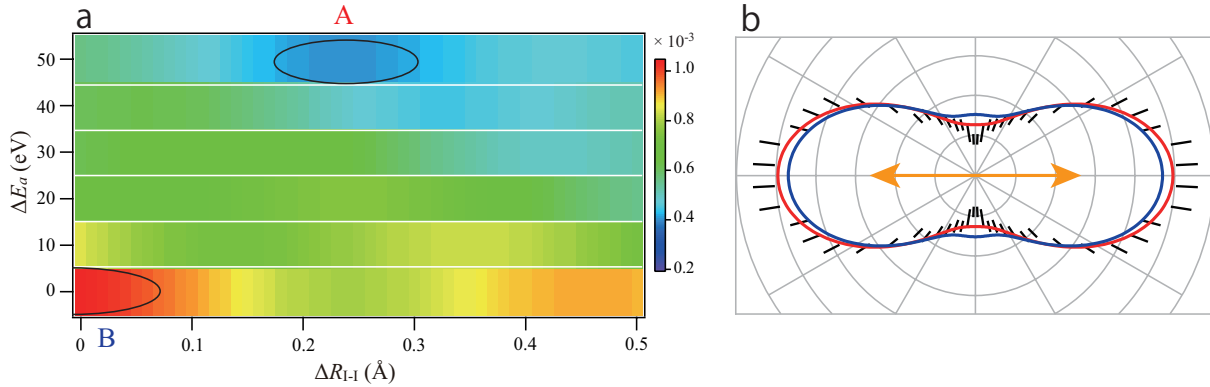
Figure 3.7.1: R-factor map as a function of parameters ΔE_a and $\Delta R_{\mathrm{I-I}}$ (a) and relevant I $2p$ XPD profiles (b). In (a), a valley exists in region A and a hill exists in region B. In (b), simulated XPD profiles at the minimum value of the R-factor in region A and at the maximum value in region B are shown by red and blue curves, respectively. The experimental data are represented by short bars, as with those in Fig. 3.5.1(b). Adapted from Ref. [109].

the best- and the worst-fitted curves because the XPD profile averaged over the molecular axis distribution exhibits a fairly simple structure, compared to the XPD profile for a given geometry (detailed in the Method section of [109]). The slightly insufficient fit between the XPD profile for the minimum value and the experimental data may be due to relativistic effects, which are discussed later.

Based on the molecular structure determination methodology described above, we can conclude that the internuclear distance of the sample I_2 molecules in the alignment Nd:YAG laser fields of 6×10^{11} W/cm^2 is elongated from 0.18 to 0.30 Å " on average", compared to the equilibrium internuclear distance of 2.666 Å.

3.8 Discussions

We successfully determined the internuclear distance of I_2 molecules in alignment-laser fields by applying our molecular structure determination methodology, which is based on non-relativistic MS-XPD theory, to I $2p$ XPD profiles measured with femtosecond XFEL pulses. Consequently, we revealed a bond softening of molecules in the alignment-laser fields. This could be mainly attributed to some portion of the I_2 molecular ensemble being electronically excited via multi-photon processes of the Nd:YAG laser. Although the analysis of the experimental data relies on quantum computations, there is no doubt that the present experiment is a critical step towards the goal of femtosecond imaging of chemical reactions, and it paves a new way for the study of

ultrafast chemical reaction in the gas phase.

Further, we aim to improve the accuracy of the determined internuclear distance. The relatively large errors are attributed to the following two factors. (i) The I $2p$ orbital is triply degenerate; hence, the I $2p$ XPD profiles obtained from the degenerate states are triply folded. More importantly, the I $2p$ XPD profiles are averaged over the axis distributions of the sample I_2 molecules. As a result, the fine structures expected in the XPD profile are smoothed out owing to the axis distributions (see Fig. 3.6.3); however, we observed one maximum and one minimum in the XPD profile. (ii) In the deep inner shells (such as I $2p_{3/2}$ and I $2p_{1/2}$, which have binding energies of 4557 eV and 4852 eV (Ref. [133]), respectively), the relativistic effects, which are not considered in our MS-XPD theory, are non-negligible. In fact, within a relativistic framework, the photoelectron asymmetry parameters for Sb $2p_{3/2}$ and $2p_{1/2}$ (which have binding energies of 4137 eV and 4385 eV, respectively) were calculated as 1.23 and 0.97, respectively, at a photon energy of 4509 eV (Ref. [134]). This implies that the difference in the asymmetry parameters is appreciable, and this difference must be reduced if these parameters are to be compared at the same photoelectron energy. Therefore, the XPD profile determined with our non-relativistic MS-XPD theory may not be fully reliable. Nevertheless, we consider that this issue is not critical, because although relativistic effects affect the primary PADs, they do not influence the scattering in the molecules.

The above-mentioned unfavorable conditions can be easily eliminated by using an XFEL in the soft X-ray region and measuring photoelectrons from non-degenerate s subshells with binding energies below approximately 3 keV. It must be noted that in these conditions, the photoelectron angular distributions are well described with a non-relativistic treatment [135].

On the one hand, the structure of molecules in an intense ($> 10^{14}$ W/cm^2), femtosecond optical laser pulse is known to change dynamically within the pulse duration via, e.g., bond softening [136], Coulomb explosion [137], and charge-resonance-enhanced ionization [138]. On the other hand, the structure of molecules in a moderately intense alignment pulse of the order of 10^{12} W/cm^2 is assumed to remain nearly identical to that of the ground state, except for bending motions along the shallowest potential directions [139]. In contrast to this assumption, our present result demonstrates that the change in the internuclear distance, i.e., the excitation of the stretching motion along the relatively deep potential directions, is likely to be induced by the moderately intense alignment pulse. Ultrafast imaging [140, 141] of molecular orbitals

by observing the spectrum of high-order harmonics has attracted considerable attention from chemists and physicists. The spectrum depends critically on both the shape of the molecular orbitals and the positions of the nuclei. Once the structure of a molecule aligned by an alignment pulse is determined by the XPD measurement, the images of the molecular orbitals that are associated with the deformed molecules can be obtained by retrieving the high-order harmonic spectra [142, 143]. By comparing the orbital images of molecules aligned in the laser fields with those of molecules aligned in field-free conditions by non-adiabatic alignment [144] or by plasma-shutter techniques [145], we can investigate the correlations and couplings between electrons in the ground and excited states using moderately intense laser fields.

3.9   Appendix: Derivation of the general PAD formula

Consider photoionization from the one-electron orbital of $\left|n_0 l_0 \lambda_0\right\rangle$ of oriented diatomic molecules with a fixed direction of the molecular axis $\boldsymbol{n}$, taken as the z-axis of a molecular coordinate system, with linearly polarized light. The angular distribution of photoelectrons ejected from the oriented molecules can be expressed as an expansion in products of spherical harmonics [47, 55, 128, 146]:

$$\frac{d\sigma^{(\lambda_0)}(\omega)}{d\hat{e}d\Omega} = -\sqrt{3}\sigma^{(\lambda_0)}(\omega) \sum_{L,M} \sum_{J}^{2} \begin{pmatrix} 1 & 1 & J \\ 0 & 0 & 0 \end{pmatrix} A_{LM}^{J(\lambda_0)} Y_{LM}(\Omega) Y_{J-M}(\hat{e}), \qquad (3.9.1)$$

where $\hat{e}$ is the polarization vector, Ω is the solid angle of the photoelectron momentum $\boldsymbol{k}$, $\sigma^{(\lambda_0)}(\omega)$ is a partial photoionization cross section for a given photon energy $\hbar\omega$, and $A_{LM}^{J(\lambda_0)}$ are the parameters defined by the following equation:

$$A_{LM}^{J(\lambda_0)} = -\frac{\sqrt{3[L,J]}}{B} \sum_{l_1 l_2} \sum_{\lambda_1 \lambda_2} \sum_{m'm''} \sqrt{[l_1,l_2]}(-1)^{m'+\lambda_2} \begin{pmatrix} l_1 & l_2 & L \\ 0 & 0 & 0 \end{pmatrix} \begin{pmatrix} l_1 & l_2 & L \\ -\lambda_1 & \lambda_2 & -M \end{pmatrix}$$

$$\times \begin{pmatrix} 1 & 1 & J \\ -m' & m'' & -M \end{pmatrix} i^{l_1-l_2} e^{i(\eta_{l_2}-\eta_{l_1})} \langle n_0 l_0 \lambda_0 | d_{m'}^{*} | \varepsilon l_1 \lambda_1 \rangle \langle \varepsilon l_2 \lambda_2 | d_{m''} | n_0 l_0 \lambda_0 \rangle,$$

$$(3.9.2)$$

where $[l] \equiv (2l+1)$. In the derivation of these equations, it is implied that a photoelectron ejected in a definite direction is described by the continuous-spectrum one-electron wave function $\psi_{\boldsymbol{k}}^{-}(\boldsymbol{r})$.

In the asymptotic region of large r, this wave function is constructed as a superposition of a plane wave propagating in the direction of the electron momentum $\boldsymbol{k}$, and a converging spherical wave. For further consideration, it is convenient to present this wave function in the following form:

$$\psi_{\boldsymbol{k}}^{-}(\boldsymbol{r}) = \sum_{l,\lambda} F_{\varepsilon l\lambda}(\boldsymbol{r})i^l \exp(-i\eta_l)Y_{l\lambda}^*(\hat{\boldsymbol{k}}), \tag{3.9.3}$$

where η_l is a Coulomb phase shift. The function $F_{\varepsilon l\lambda}(\boldsymbol{r})$ does not depend on the direction of photoelectron propagation. Moreover, it is normalized to the energy δ-function (the energy ε is connected with the momentum as usual, $\varepsilon = k^2/2$), and it has a complex value that includes the phase shift due to the short-range potential. The dipole matrix elements for Eq.(3.9.2) are reduced to one-electron integrals by using the same one-electron molecular basis for the initial and final states. The operator $d_m = \sqrt{\frac{4}{3}\pi}rY_{1m}(\theta, \varphi)$ is the dipole transition operator. The constant B is given by

$$B = \sum_{l\lambda}\sum_{m}\left|\langle\varepsilon l\lambda|d_m|n_0l_0\lambda_0\rangle\right|^2. \tag{3.9.4}$$

First, consider the molecules ionized by linearly polarized light with the polarization vector $\boldsymbol{e}_z$ parallel to the molecular axis $\boldsymbol{n}$. The process achieves axial symmetry about the molecular axis; therefore, only the spherical harmonics $Y_{J-M}(\hat{\boldsymbol{e}})$ with $M = 0$ in Eq. (3.9.1) are present in the cross section. Consequently, by using explicit forms of the Wigner $3j$ (or $3jm$) symbols [129], Eq. (3.9.1) can be expressed in terms of the Legendre polynomials as

$$\frac{d\sigma^{(\lambda_0)}(\omega)}{d\hat{\boldsymbol{e}}_z d\Omega} = \frac{\sigma^{(\lambda_0)}(\omega)}{4\pi}\sum_{L=0}^{L_{\max}}\sqrt{2L+1}(A_{L0}^{0(\lambda_0)} - \sqrt{2}A_{L0}^{2(\lambda_0)})P_L(\cos\theta). \tag{3.9.5}$$

If the relevant one-electron orbitals are degenerate, the differential cross sections are summed over all the orbitals:

$$\frac{d\sigma(\omega)}{d\hat{\boldsymbol{e}}_z d\Omega} = \frac{\sigma(\omega)}{4\pi}\sum_{L=0}^{L_{\max}}A_L P_L(\cos\theta), \tag{3.9.6}$$

$$A_L \equiv \frac{\sigma^{(\lambda_0)}(\omega)}{\sigma(\omega)}\sqrt{2L+1}\sum_{\lambda_0=-l_0}^{l_0}(A_{L0}^{0(\lambda_0)} - \sqrt{2}A_{L0}^{2(\lambda_0)}). \tag{3.9.7}$$

Now, suppose that light is linearly polarized along the x-axis of the molecular frame. Then,

it follows from Eq. (3.9.1) that

$$
\frac{d\sigma^{(\lambda_0)}(\omega)}{d\hat{e}_x d\Omega}
$$

$$
= -\sqrt{3}\sigma^{(\lambda_0)}(\omega) \sum_L \Bigg[\sqrt{\frac{1}{4\pi}} \begin{pmatrix} 1 & 1 & 0 \\ 0 & 0 & 0 \end{pmatrix} A_{L0}^{0(\lambda_0)} Y_{L0}(\Omega) - \sqrt{\frac{5}{16\pi}} \begin{pmatrix} 1 & 1 & 2 \\ 0 & 0 & 0 \end{pmatrix} A_{L0}^{2(\lambda_0)} Y_{L0}(\Omega)
$$

$$
+ \sqrt{\frac{15}{32\pi}} \begin{pmatrix} 1 & 1 & 2 \\ 0 & 0 & 0 \end{pmatrix} A_{L-2}^{2(\lambda_0)} Y_{L-2}(\Omega) + \sqrt{\frac{15}{32\pi}} \begin{pmatrix} 1 & 1 & 2 \\ 0 & 0 & 0 \end{pmatrix} A_{L2}^{2(\lambda_0)} Y_{L2}(\Omega) \Bigg].
$$

$$(3.9.8)$$

The symmetry relations of the Clebsch-Gordan coefficients [129, 130]

$$
\langle j_1 m_1 j_2 m_2 | j_3 m_3 \rangle = (-1)^{j_1+j_2-j_3} \langle j_1 - m_1 j_2 - m_2 | j_3 - m_3 \rangle \tag{3.9.9}
$$

$$
\langle j_1 m_1 j_2 m_2 | j_3 m_3 \rangle = (-1)^{j_1+j_2-j_3} \langle j_2 m_2 j_1 m_1 | j_3 m_3 \rangle \tag{3.9.10}
$$

and the relation between the Clebsch-Gordan coefficient and the Wigner $3j$ (or $3jm$) symbol [129]

$$
\langle j_1 m_1 j_2 m_2 | j_3 m_3 \rangle = (-1)^{j_1-j_2+m_3} \sqrt{2j_3+1} \begin{pmatrix} j_1 & j_2 & j_3 \\ m_1 & m_2 & -m_3 \end{pmatrix} \tag{3.9.11}
$$

leads to the symmetry relation of the Wigner $3j$ (or $3jm$) symbol:

$$
\begin{pmatrix} j_1 & j_2 & j_3 \\ m_1 & m_2 & m_3 \end{pmatrix} = \begin{pmatrix} j_1 & j_2 & j_3 \\ -m_2 & -m_1 & m_3 \end{pmatrix}. \tag{3.9.12}
$$

By using Eq. (3.9.12), the symmetry relation of the coefficient $A_{L-M}^{J(\lambda_0)}$ is obtained:

$$
A_{L-M}^{J(\lambda_0)} = -\frac{\sqrt{3}[L,J]}{B} \sum_{l_1 l_2} \sum_{\lambda_1 \lambda_2} \sum_{m'm''} \sqrt{[l_1,l_2]} (-1)^{m'+\lambda_2}
\begin{pmatrix} l_1 & l_2 & L \\ 0 & 0 & 0 \end{pmatrix}
\begin{pmatrix} l_1 & l_2 & L \\ -\lambda_1 & \lambda_2 & M \end{pmatrix}
$$

$$
\times
\begin{pmatrix} 1 & 1 & J \\ -m' & m'' & M \end{pmatrix}
i^{l_1-l_2} e^{i(\eta_{l_2}-\eta_{l_1})} \langle n_0 l_0 \lambda_0 | d_{m'}^* | \varepsilon l_1 \lambda_1 \rangle \langle \varepsilon l_2 \lambda_2 | d_{m''} | n_0 l_0 \lambda_0 \rangle
$$

$$
= -\frac{\sqrt{3}[L,J]}{B} \sum_{l_1 l_2} \sum_{\lambda_1 \lambda_2} \sum_{m'm''} \sqrt{[l_1,l_2]} (-1)^{m''+\lambda_1}
\begin{pmatrix} l_2 & l_1 & L \\ 0 & 0 & 0 \end{pmatrix}
\begin{pmatrix} l_2 & l_1 & L \\ -\lambda_2 & \lambda_1 & -M \end{pmatrix}
$$

$$
\times
\begin{pmatrix} 1 & 1 & J \\ -m'' & m' & -M \end{pmatrix}
(-i)^{l_2-l_1} e^{-i(\eta_{l_1}-\eta_{l_2})} \left(\langle n_0 l_0 \lambda_0 | d_{m''}^* | \varepsilon l_2 \lambda_2 \rangle \langle \varepsilon l_1 \lambda_1 | d_{m'} | n_0 l_0 \lambda_0 \rangle \right)^*
$$

$$
= A_{LM}^{J(\lambda_0)*}.
$$

$$(3.9.13)$$

If $\lambda_0 = 0$, all the coefficients for Eq. (3.9.8) are real:

$$
A_{L0}^{J(0)} = -\frac{\sqrt{3}[L,J]}{B} \sum_{l_1 l_2} \sqrt{[l_1,l_2]} i^{l_1-l_2} e^{i(\eta_{l_2}-\eta_{l_1})}
\begin{pmatrix} l_1 & l_2 & L \\ 0 & 0 & 0 \end{pmatrix}
$$

$$
\times \left[
\begin{pmatrix} l_1 & l_2 & L \\ 1 & -1 & 0 \end{pmatrix}
\begin{pmatrix} 1 & 1 & J \\ 1 & -1 & 0 \end{pmatrix}
\langle n_0 l_0 0 | d_{-1}^* | \varepsilon l_1 -1 \rangle \langle \varepsilon l_2 -1 | d_{-1} | n_0 l_0 0 \rangle
\right.
$$

$$
+
\begin{pmatrix} l_1 & l_2 & L \\ 0 & 0 & 0 \end{pmatrix}
\begin{pmatrix} 1 & 1 & J \\ 0 & 0 & 0 \end{pmatrix}
\langle n_0 l_0 0 | d_0^* | \varepsilon l_1 0 \rangle \langle \varepsilon l_2 0 | d_0 | n_0 l_0 0 \rangle
$$

$$
\left.
+
\begin{pmatrix} l_1 & l_2 & L \\ -1 & 1 & 0 \end{pmatrix}
\begin{pmatrix} 1 & 1 & J \\ -1 & 1 & 0 \end{pmatrix}
\langle n_0 l_0 0 | d_1^* | \varepsilon l_1 1 \rangle \langle \varepsilon l_2 1 | d_1 | n_0 l_0 0 \rangle
\right],
$$

$$(3.9.14)$$

$$
A_{L2}^{J(0)} = -\frac{\sqrt{3}[L,J]}{B} \sum_{l_1 l_2} \sqrt{[l_1,l_2]} i^{l_1-l_2} e^{i(\eta_{l_2}-\eta_{l_1})}
\begin{pmatrix} l_1 & l_2 & L \\ 0 & 0 & 0 \end{pmatrix}
$$

$$
\times
\begin{pmatrix} l_1 & l_2 & L \\ 1 & 1 & -2 \end{pmatrix}
\begin{pmatrix} 1 & 1 & J \\ 1 & 1 & -2 \end{pmatrix}
\langle n_0 l_0 0 | d_{-1}^* | \varepsilon l_1 -1 \rangle \langle \varepsilon l_2 -1 | d_{-1} | n_0 l_0 0 \rangle,
$$

$$(3.9.15)$$

because the summations over l_1 and l_2 are symmetric. Equation (3.9.15) is obtained by using the integral

$$\int d\Omega Y_{lm}^*(\Omega)Y_{l_1m_1}(\Omega)Y_{l_2m_2}(\Omega) = \sqrt{\frac{(2l_1+1)(2l_2+1)}{4\pi(2l+1)}}\langle l_10l_20|l0\rangle\langle l_1m_1l_2m_2|lm\rangle \qquad (3.9.16)$$

and Eq. (3.9.9). This is not the case for $\lambda_0 \neq 0$. In the case of $\lambda_0 = 1$, for example,

$$A_{L0}^{J(1)} = -\frac{\sqrt{3[L,J]}}{B}\sum_{l_1l_2}\sqrt{[l_1,l_2]}i^{l_1-l_2}e^{i(\eta_{l_2}-\eta_{l_1})}\begin{pmatrix} l_1 & l_2 & L \\ 0 & 0 & 0 \end{pmatrix}$$

$$\times\left[-\begin{pmatrix} l_1 & l_2 & L \\ 0 & 0 & 0 \end{pmatrix}\begin{pmatrix} 1 & 1 & J \\ 1 & -1 & 0 \end{pmatrix}\langle n_0l_01|d_{-1}^*|\varepsilon l_10\rangle\langle \varepsilon l_20|d_{-1}|n_0l_01\rangle\right.$$

$$\left.-\begin{pmatrix} l_1 & l_2 & L \\ -1 & 1 & 0 \end{pmatrix}\begin{pmatrix} 1 & 1 & J \\ 0 & 0 & 0 \end{pmatrix}\langle n_0l_01|d_0^*|\varepsilon l_11\rangle\langle \varepsilon l_21|d_0|n_0l_01\rangle\right.$$

$$\left.-\begin{pmatrix} l_1 & l_2 & L \\ -2 & 2 & 0 \end{pmatrix}\begin{pmatrix} 1 & 1 & J \\ -1 & 1 & 0 \end{pmatrix}\langle n_0l_01|d_1^*|\varepsilon l_12\rangle\langle \varepsilon l_22|d_1|n_0l_01\rangle\right],$$

(3.9.17)

$$A_{L2}^{J(1)} = \frac{\sqrt{3[L,J]}}{B}\sum_{l_1l_2}\sqrt{[l_1,l_2]}i^{l_1-l_2}e^{i(\eta_{l_2}-\eta_{l_1})}\begin{pmatrix} l_1 & l_2 & L \\ 0 & 0 & 0 \end{pmatrix}$$

$$\times\begin{pmatrix} l_1 & l_2 & L \\ 0 & 2 & -2 \end{pmatrix}\begin{pmatrix} 1 & 1 & J \\ 1 & 1 & -2 \end{pmatrix}\langle n_0l_01|d_{-1}^*|\varepsilon l_10\rangle\langle \varepsilon l_22|d_1|n_0l_01\rangle,$$

(3.9.18)

where $l_2 = 0$ is forbidden for $A_{L2}^{J(1)}$. Thus, the differential cross section $d\sigma^{(\lambda_0)}(\omega)/d\hat{e}_x d\Omega$ is proportional to $\cos(2\varphi + \arg A_{L2}^{J(\lambda_0)})$.

The integral (3.9.16) and the symmetry relation (3.9.9) also give the relation $A_{LM}^{J(-\lambda_0)} = A_{L-M}^{J(\lambda_0)} = A_{LM}^{J(\lambda_0)*}$. This leads to the differential photoionization cross section summed over all

the degenerate one-electron orbitals:

$$
\begin{aligned}
\frac{d\sigma(\omega)}{d\hat{e}_x d\Omega} = -\sqrt{3}\sum_L \Bigg\{ & \sqrt{\frac{1}{4\pi}}\begin{pmatrix} 1 & 1 & 0 \\ 0 & 0 & 0 \end{pmatrix}\Big(\sum_{\lambda_0=-l_0}^{l_0}\sigma^{(\lambda_0)}A_{L0}^{0(\lambda_0)}\Big)Y_{L0}(\Omega) \\
& -\sqrt{\frac{5}{16\pi}}\begin{pmatrix} 1 & 1 & 2 \\ 0 & 0 & 0 \end{pmatrix}\Big(\sum_{\lambda_0=-l_0}^{l_0}\sigma^{(\lambda_0)}A_{L0}^{2(\lambda_0)}\Big)Y_{L0}(\Omega) \\
& +\sqrt{\frac{15}{32\pi}}\begin{pmatrix} 1 & 1 & 2 \\ 0 & 0 & 0 \end{pmatrix}\Big[\sigma^{(0)}A_{L-2}^{2(0)}+2\sum_{\lambda_0=1}^{l_0}\Re\big(\sigma^{(\lambda_0)}A_{L-2}^{2(\lambda_0)}\big)\Big]\big(Y_{L2}(\Omega)+Y_{L-2}(\Omega)\big)\Bigg\} \\
= \frac{1}{4\pi}\sum_L\Bigg\{ & \sqrt{2L+1}\sum_{\lambda_0=-l_0}^{l_0}\sigma^{(\lambda_0)}\Big(A_{L0}^{0(\lambda_0)}+\sqrt{\frac{1}{2}}A_{L0}^{2(\lambda_0)}\Big)P_L(\cos\theta) \\
& -\sqrt{\frac{3(2L+1)(L-2)!}{(L+2)!}}\Big[\sigma^{(0)}A_{L-2}^{2(0)}+2\sum_{\lambda_0=1}^{l_0}\Re\big(\sigma^{(\lambda_0)}A_{L-2}^{2(\lambda_0)}\big)\Big]P_L^2(\cos\theta)\cos2\varphi\Bigg\}.
\end{aligned}
$$

$$(3.9.19)$$

The explicit forms of the associated Legendre functions [120]

$$
P_L^M(z) = (1-z^2)^{M/2}\frac{d^M}{dz^M}P_L(z), \tag{3.9.20}
$$

Legendre's differential equation [120]

$$
(1-z^2)\frac{d^2f}{dz^2}-2z\frac{df}{dz}+L(L+1)f=0, \tag{3.9.21}
$$

and the recursion relation [120]

$$
\frac{dP_{L-1}}{dz}=-LP_L+z\frac{dP_L}{dz} \tag{3.9.22}
$$

lead to a useful relation:

$$
P_L^2(\cos\theta)=-L(L-1)P_L(\cos\theta)+2\sum_{L_1=0(1),2(3),\ldots}^{L-2}(2L_1+1)P_{L_1}(\cos\theta). \tag{3.9.23}
$$

By using Eq. (3.9.23), Eq. (3.9.19) can be transformed into a simpler form:

$$
\frac{d\sigma(\omega)}{d\hat{e}_x d\Omega}=\frac{\sigma}{4\pi}\sum_L\Big\{B_L P_L(\cos\theta)+C_L P_L^2(\cos\theta)\cos2\varphi\Big\}, \tag{3.9.24}
$$

where

$$B_L = \sqrt{2L+1} \sum_{\lambda_0=-l_0}^{l_0} \frac{\sigma^{(\lambda_0)}}{\sigma} \left(A_{L0}^{0(\lambda_0)} + \sqrt{\frac{1}{2}} A_{L0}^{2(\lambda_0)} \right), \qquad (3.9.25)$$

$$\begin{aligned} C_L = {} & L(L-1) \sqrt{\frac{3(2L+1)(L-2)!}{(L+2)!}} \left[\frac{\sigma^{(0)}}{\sigma} A_{L-2}^{2(0)} + 2 \sum_{\lambda_0=1}^{l_0} \Re\left(\frac{\sigma^{(\lambda_0)}}{\sigma} A_{L-2}^{2(\lambda_0)} \right) \right] \\ & - 2(2L+1) \sum_{L'=L+2,L+4,\ldots}^{L_{\max}} \sqrt{\frac{3(2L'+1)(L'-2)!}{(L'+2)!}} \left[\frac{\sigma^{(0)}}{\sigma} A_{L'-2}^{2(0)} + 2 \sum_{\lambda_0=1}^{l_0} \Re\left(\frac{\sigma^{(\lambda_0)}}{\sigma} A_{L'-2}^{2(\lambda_0)} \right) \right]. \end{aligned}$$

$$(3.9.26)$$

Chapter 4

Theory of time-resolved XPD

4.1 Introduction

Direct probing of the atomic structure of matter, whether static or dynamic, plays an essential role in physics, chemistry, and biology [92, 147]. Thus far, most of our knowledge on atomic structures has been derived from X-ray and electron diffraction measurements [10, 11, 148, 149]. However, with the advent of XFELs [86, 88], ultrafast imaging with femtosecond temporal resolution and sub-Ångström spatial resolution has emerged as an active research area with the potential to prove a "molecular movie" of the dynamics of a chemical process. Indeed, besides traditional approaches based on X-ray diffraction [10, 11, 148] and ultrafast electron diffraction [149, 150], new methods using femtosecond pulses from XFELs have been proposed and successfully tested on isolated free molecules. Examples include pump–probe gas phase X-ray scattering [100–102] and femtosecond X-ray photoelectron diffraction [78, 104–112]. Although the analyses of the experimental data in Refs. [100, 109] heavily rely on quantum chemical computations, there is no doubt that these experiments constitute a critical step towards the goal of femtosecond imaging of chemical reactions.

In this Chapter, we report on the theoretical simulation results of time-resolved X-ray photoelectron diffraction (XPD) following the ultrafast dynamics of nuclear wave packets populated by optical laser pulses. In summary, the present method is based on an optical laser pump–XFEL probe scheme, which is illustrated schematically in Fig. 1.4.1 of Chap. 1. Aligned or oriented molecules are first excited electronically by a short optical laser pulse, so that the nuclear wave packets on a specific potential energy surface of an electronically excited state start

to move. Their nuclear dynamics is subsequently probed by means of inner-shell XPD profiles at different time delays τ by ultrafast XFEL pulses. Theoretically, we predict the inner-shell XPD profiles as functions of the time delay τ, in which the nuclear wave packet evolution is taken into account within the Born-Oppenheimer approximation. Because one of the objectives of the present study is to reveal the effects of the shape, i.e., the width and intensity, of the pump-laser pulse on the XPD profiles, we performed the simulations under ideal conditions. In other words, we assumed that the sample molecules are fully aligned and that they are fully excited by the pump-laser pulse. Otherwise, such effects may be blurred by both an insufficient alignment and mixture of the excited and ground states, which depend on the experimental conditions.

The reminder of this chapter is organized as follows. Sec. 4.2 describes the theoretical method, i.e., the numerical calculations of nuclear wave packets, calculations of the XPD profile via multiple-scattering XPD (MS-XPD) theory for a fixed-nuclear geometry, and formulation of the time-resolved XPD on a path of nuclear wave packet evolution. The main results are presented in Sec. 4.3, where we simulate the time-dependent XPD profiles for the dissociation dynamics of I_2 molecules and the bending vibrational dynamics of CS_2 molecules. Finally, Sec. 4.4 summarizes our study.

4.2   Theoretical method

A nuclear wave packet created by an optical pump-laser pulse is obtained by the numerical integral of the time-dependent Schrödinger equation (TDSE). XPD profiles for certain molecular geometries are calculated by the MS-XPD theory described in Chap. 2. Then the XPD profile for the molecule residing on the electronic excited state is the convolution of the XPD profiles weighted by the nuclear wave packet over the molecular geometry within the Chase adiabatic approximation [151].

The nonrelativistic Hamiltonian for an n-electron and N-nuclear molecule coupled with an electromagnetic field is given in atomic units as

$$
\begin{aligned}
H = &\sum_{\alpha=1}^{N} \frac{1}{2M_\alpha} [\boldsymbol{P}_\alpha - Z_\alpha \boldsymbol{A}(\boldsymbol{R}_\alpha, t)]^2 + \sum_{i=1}^{n} \frac{1}{2} [\boldsymbol{p}_i + \boldsymbol{A}(\boldsymbol{r}_i, t)]^2 \\
&- \sum_{i=1}^{n} \sum_{\alpha=1}^{N} \frac{Z_\alpha}{|\boldsymbol{R}_\alpha - \boldsymbol{r}_i|} + \sum_{\alpha > \beta}^{N} \frac{Z_\alpha Z_\beta}{|\boldsymbol{R}_\alpha - \boldsymbol{R}_\beta|} + \sum_{i>j}^{n} \frac{1}{|\boldsymbol{r}_i - \boldsymbol{r}_j|},
\end{aligned}
\tag{4.2.1}
$$

where $\{r_i\}$, $\{R_\alpha\}$, $\{Z_\alpha\}$, $A(r_i, t)$, and $A(R_\alpha, t)$ represent the spatial coordinates of the i-th electron, the spatial coordinates of the α-th nucleus, the charge of the α-th nucleus, and the time-dependent vector potentials of electromagnetic fields at the positions of the i-th electron and α-th nucleus, respectively. Next, by using the abbreviations $R = \{R_1, R_2, \ldots, R_N\}$ and $r = \{r_1, r_2, \ldots, r_n\}$, the TDSE for this system is written as

$$i\frac{\partial}{\partial t}\Psi(R, r, t) = H\Psi(R, r, t). \tag{4.2.2}$$

By implementation of the dipole approximation of $A(R_\alpha, t) \cong A(t)$ and $A(r_i, t) \cong A(t)$ and unitary transformation of $\prod_{\alpha=1}^{N}\exp[-iZ_\alpha A(t) \cdot R_\alpha]\prod_{i=1}^{n}\exp[-iA(t) \cdot r_i]$ to the wave function $\Psi(R, r, t)$ in Eq. (4.2.2), the TDSE is expressed as

$$
\begin{aligned}
i\frac{\partial}{\partial t}\Psi(R, r, t) = \Big[&\sum_{\alpha=1}^{N}\frac{P_\alpha^2}{2M_\alpha} + \sum_{i=1}^{n}\frac{p_i^2}{2} + E(t) \cdot \sum_{i=1}^{n}r_i \\
&- \sum_{i=1}^{n}\sum_{\alpha=1}^{N}\frac{Z_\alpha}{|R_\alpha - r_i|} + \sum_{\alpha>\beta}^{N}\frac{Z_\alpha Z_\beta}{|R_\alpha - R_\beta|} + \sum_{i>j}^{n}\frac{1}{|r_i - r_j|}\Big]\Psi(R, r, t),
\end{aligned}
\tag{4.2.3}
$$

where $E(t) = -\partial A(t)/\partial t$. In Eq. (4.2.3), the interaction between the nucleus and the electromagnetic field is ignored.

Here, we introduce the Hamiltonian for electrons without external fields at the fixed nuclear position of R:

$$H_{\mathrm{el}}(R) = \sum_{i=1}^{n}\frac{p_i^2}{2} - \sum_{i=1}^{n}\sum_{\alpha=1}^{N}\frac{Z_\alpha}{|R_\alpha - r_i|} + \sum_{i>j}^{n}\frac{1}{|r_i - r_j|}. \tag{4.2.4}$$

Next, under the two-level approximation we consider the ground- and excited-state electronic wave functions of $\Phi_g(r; R)$ and $\Phi_e(r; R)$, which satisfy the following time-independent Schrödinger equations:

$$\begin{cases} H_{\mathrm{el}}(R)\Phi_g(r; R) = \varepsilon_g(R)\Phi_g(r; R) \\ H_{\mathrm{el}}(R)\Phi_e(r; R) = \varepsilon_e(R)\Phi_e(r; R) \end{cases}. \tag{4.2.5}$$

In this context, the wave function $\Psi(R, r, t)$, which satisfies the TDSE of Eq. (4.2.3), can be expressed by the superposition of $\Phi_g(r; R)$ and $\Phi_e(r; R)$ as follows:

$$\Psi(R, r, t) = \chi_g(R, t)\Phi_g(r; R) + \chi_e(R, t)\Phi_e(r; R). \tag{4.2.6}$$

By inserting Eq. (4.2.6) into Eq. (4.2.3) and using the orthogonality of $\Phi_g(r; R)$ and $\Phi_e(r; R)$,

we derive the following coupled TDSE for the nuclear wave packets:

$$
i\frac{\partial}{\partial t}\begin{bmatrix} \chi_g(\boldsymbol{R},t) \\ \chi_e(\boldsymbol{R},t) \end{bmatrix} = \begin{bmatrix} \sum_{\alpha=1}^{N}\frac{\boldsymbol{P}_\alpha^2}{2M_\alpha}+V_g(\boldsymbol{R}) & \boldsymbol{E}(t)\cdot\langle\Phi_g|\sum_{i=1}^{n}\boldsymbol{r}_i|\Phi_e\rangle \\ \boldsymbol{E}(t)\cdot\langle\Phi_e|\sum_{i=1}^{n}\boldsymbol{r}_i|\Phi_g\rangle & \sum_{\alpha=1}^{N}\frac{\boldsymbol{P}_\alpha^2}{2M_\alpha}+V_e(\boldsymbol{R}) \end{bmatrix}\begin{bmatrix} \chi_g(\boldsymbol{R},t) \\ \chi_e(\boldsymbol{R},t) \end{bmatrix},
$$
(4.2.7)

where $V_{g(e)}(\boldsymbol{R})$ denotes the potential of the nuclei, i.e.,

$$
V_{g(e)}(\boldsymbol{R}) = \varepsilon_{g(e)}(\boldsymbol{R}) + \sum_{\alpha>\beta}^{N}\frac{Z_\alpha Z_\beta}{|\boldsymbol{R}_\alpha-\boldsymbol{R}_\beta|}.
$$
(4.2.8)

In Eq. (4.2.7), the vibronic interaction is ignored, which may be valid within the framework of the Born-Oppenheimer approximation.

The TDSE of Eq. (4.2.7) for the vibrational wave packets can be integrated for an infinitesimal time step Δt by a standard computational technique, such as a split operator method [152] or a higher-order symplectic integrator method [153]:

$$
\begin{bmatrix} \chi_g(\boldsymbol{R},t+\Delta t) \\ \chi_e(\boldsymbol{R},t+\Delta t) \end{bmatrix} \approx \exp(-i\Delta t T/2)\exp[-i\Delta t V(t)]\exp(-i\Delta t T/2)\begin{bmatrix} \chi_g(\boldsymbol{R},t) \\ \chi_e(\boldsymbol{R},t) \end{bmatrix},
$$
(4.2.9)

where

$$
T \equiv \begin{bmatrix} \sum_{\alpha=1}^{N}\frac{\boldsymbol{P}_\alpha^2}{2M_\alpha} & 0 \\ 0 & \sum_{\alpha=1}^{N}\frac{\boldsymbol{P}_\alpha^2}{2M_\alpha} \end{bmatrix}
$$
(4.2.10)

and

$$
V(t) \equiv \begin{bmatrix} V_g(\boldsymbol{R}) & \boldsymbol{E}(t)\cdot\langle\Phi_g|\sum_{i=1}^{n}\boldsymbol{r}_i|\Phi_e\rangle \\ \boldsymbol{E}(t)\cdot\langle\Phi_e|\sum_{i=1}^{n}\boldsymbol{r}_i|\Phi_g\rangle & V_e(\boldsymbol{R}) \end{bmatrix}.
$$
(4.2.11)

The two exponential functions, $\exp(-i\Delta t T/2)$ and $\exp[-i\Delta t V(t)]$, each involving a matrix as its argument, are evaluated as

$$
\exp(-i\Delta t T/2) = \begin{bmatrix} \exp\left[-i\Delta\frac{t}{2}\sum_{\alpha=1}^{N}\frac{\boldsymbol{P}_\alpha^2}{2M_\alpha}\right] & 0 \\ 0 & \exp\left[-i\Delta\frac{t}{2}\sum_{\alpha=1}^{N}\frac{\boldsymbol{P}_\alpha^2}{2M_\alpha}\right] \end{bmatrix}
$$
(4.2.12)

and

$$\exp[-i\Delta t V(t)] = C(t)C(t)^{-1} \exp[-i\Delta t V(t)]C(t)C(t)^{-1}$$

$$= C(t) \begin{bmatrix} \exp[-i\Delta t v_1(t)] & 0 \\ 0 & \exp[-i\Delta t v_2(t)] \end{bmatrix} C(t)^{-1},$$
(4.2.13)

respectively, where $C(t)$ is a matrix that diagonalizes $V(t)$ such that

$$C(t)^{-1}V(t)C(t) = \begin{bmatrix} v_1(t) & 0 \\ 0 & v_2(t) \end{bmatrix}.$$
(4.2.14)

The initial condition for the iteration of Eq. (4.2.9) is given by

$$\chi_g(\boldsymbol{R}, t = -\infty) = \chi_g(\boldsymbol{R}) \text{ and } \chi_e(\boldsymbol{R}, t = -\infty) = 0.$$
(4.2.15)

Thus, the iteration begins from the ground-state vibrational wave function $\chi_g(\boldsymbol{R})$. Since the norm of $\chi_g(\boldsymbol{R})$ is normalized to unity, the integral of $|\chi_{g(e)}(\boldsymbol{R}, t)|^2$ over the nuclear coordinate $\boldsymbol{R}$ yields the population of the electronic ground (excited) state. In practical nuclear wave packet calculations, the normal coordinates are used instead of the spatial coordinates.

In this study, we assumed a Gaussian-shaped pulse for optical lasers:

$$\boldsymbol{E}(t) = \boldsymbol{E}_0 \exp[-\ln 2(2t/\Gamma)^2] \cos \omega_0 t,$$
(4.2.16)

where $\boldsymbol{E}_0$, ω_0 and Γ represent the electric field strength, the central frequency, and the temporal pulse width of the laser (full width at half maximum, FWHM), respectively. The laser intensity is given by $I_0 = \varepsilon_0 c E_0^2 / 2$, i.e., the electric energy passing through a surface of a unit cube in unit time. The constant ε_0 is the permittivity of vacuum and c is the speed of light in vacuum. The atomic unit of the electric field strength is the field experienced by an electron in the ground state of atomic hydrogen, $E_0 = 5.14 \times 10^9$ V/cm, and the corresponding laser intensity is $I_0 = 3.51 \times 10^{16}$ W/cm^2.

Under sudden approximation, the amplitude of core-level photoemission from an electroni-

cally excited molecule is expressed as [78]:

$$\langle\psi_{\boldsymbol{k}}^{-}(\boldsymbol{r};\boldsymbol{R})\Phi_h(\boldsymbol{r}^{n-1};\boldsymbol{R})\big|\hat{e}\cdot\boldsymbol{r}\big|\Phi_e(\boldsymbol{r};\boldsymbol{R})\rangle \approx \langle\psi_{\boldsymbol{k}}^{-}(\boldsymbol{r}_{\mathrm{A}};\boldsymbol{R})\big|\hat{e}\cdot\boldsymbol{r}_{\mathrm{A}}\big|\phi_c(\boldsymbol{r}_{\mathrm{A}})\rangle, \qquad (4.2.17)$$

where $\psi_{\boldsymbol{k}}^{-}(\boldsymbol{r}_{\mathrm{A}};\boldsymbol{R})$ represents the photoelectron wave function of the momentum $\boldsymbol{k}$ under the influence of the optical potential; $\phi_c(\boldsymbol{r}_{\mathrm{A}})$ represents the wave function of a core orbital localized on the atomic site A; and $\hat{e}$ represents the polarization vector of XFEL. The atomic wave function $\phi_c(\boldsymbol{r}_{\mathrm{A}})$ may hardly be influenced by the molecular structure, whereas it may be assumed that the photoelectron wave function $\psi_{\boldsymbol{k}}^{-}(\boldsymbol{r}_{\mathrm{A}};\boldsymbol{R})$ depends on a transient molecular structure. By assuming these simple descriptions for the wave functions, the one-electron matrix element of Eq. (4.2.17) is calculated on the basis of the MS-XPD theory [39, 40, 77, 78]. By conducting the calculations of the MS-XPD formula explained in Chap. 2, we can obtain an XPD profile $d\sigma(\boldsymbol{R})/d\hat{\boldsymbol{k}}$:

$$\frac{d\sigma}{d\hat{\boldsymbol{k}}}(\boldsymbol{R}) \propt |\langle\psi_{\boldsymbol{k}}^{-}(\boldsymbol{r}_{\mathrm{A}};\boldsymbol{R})\big|\hat{e}\cdot\boldsymbol{r}_{\mathrm{A}}\big|\phi_c(\boldsymbol{r}_{\mathrm{A}})\rangle|^2. \qquad (4.2.18)$$

Theoretically, a time-resolved XPD profile $d\sigma(\boldsymbol{R},\tau)/d\hat{\boldsymbol{k}}$ with ultrafast XFEL pulses at a time delay τ after a pump pulse can be formulated as

$$\frac{d\sigma}{d\hat{\boldsymbol{k}}}(\boldsymbol{R},\tau) \propto \int d\boldsymbol{R}|\chi_e(\boldsymbol{R},\tau)|^2|\langle\psi_{\boldsymbol{k}}^{-}(\boldsymbol{r}_{\mathrm{A}};\boldsymbol{R})\big|\hat{e}\cdot\boldsymbol{r}_{\mathrm{A}}\big|\phi_c(\boldsymbol{r}_{\mathrm{A}})\rangle|^2, \qquad (4.2.19)$$

where $\chi_e(\boldsymbol{R},\tau)$ represents the nuclear wave packet induced by the optical laser pulses and $|\langle\psi_{\boldsymbol{k}}^{-}(\boldsymbol{r}_{\mathrm{A}};\boldsymbol{R})\big|\hat{e}\cdot\boldsymbol{r}_{\mathrm{A}}\big|\phi_c(\boldsymbol{r}_{\mathrm{A}})\rangle|^2$ represents the XPD profile for the molecular structure described by the set of position vectors $\boldsymbol{R}$. The above equation can be derived within the Chase adiabatic approximation [151] under the assumption that the nuclei are frozen during the probe pulse. For the applications of Eq. (4.2.19), we used $\chi_e(\boldsymbol{R},\tau)$, which was obtained by solving Eq. (4.2.7) numerically for typical intensities and pulse widths of available optical lasers. Next, we used the $\boldsymbol{R}$-dependent XPD profiles, which were calculated using Eq. (4.2.18) by assuming muffin-tin potentials. It should be noted that we assumed that the phase shift $\delta_l^{\alpha}(k)$ was constant over $\boldsymbol{R}$.

A few remarks on our simulations are in order. The duration of the ultrafast XFEL pulses was not taken into account, and the convolution of XPD profiles $d\sigma(\boldsymbol{R})/d\hat{\boldsymbol{k}}$ over the photon spectral bandwidth was not carried out. The effects of these two factors on the XPD profiles need to be examined later for time-dependent XPD data analyses.

Classical trajectories for the relevant photochemical reactions were also calculated by the numerical integral of Newton's equations of motion:

$$\begin{cases} \boldsymbol{R}(t + dt) = \boldsymbol{R}(t + dt) + \boldsymbol{v}(t)dt \\ \boldsymbol{v}(t + dt) = \boldsymbol{v}(t) - \frac{1}{\mu}\frac{dV_e(\boldsymbol{R})}{d\boldsymbol{R}} \end{cases}, \tag{4.2.20}$$

where $\boldsymbol{v}(t)$ are the classical velocities of $d\boldsymbol{R}(t)/dt$ and μ is the reduced mass of the relevant normal coordinates. The potential energy surface $V_e(\boldsymbol{R})$ is the same as that for Eq. (4.2.7), i.e., Eq. (4.2.8). The initial nuclear positions $\boldsymbol{R}(t = 0)$ are those for the equilibrium molecular geometry of the ground state. The initial velocities are given by $|\boldsymbol{v}(t = 0)| = \sqrt{2\{E_0 + \omega_0 - V_e[\boldsymbol{R}(t = 0)]\}/\mu}$, where E_0 is the zero-point vibrational energy for the ground state, and $\boldsymbol{v}(t = 0)/|\boldsymbol{v}(t = 0)| = \frac{dV_e[\boldsymbol{R}(t=0)]}{d\boldsymbol{R}}/|\frac{dV_e[\boldsymbol{R}(t=0)]}{d\boldsymbol{R}}|$. It should be emphasized that iterations of photoabsorption and photoemission for the duration of the optical lasers were not taken into account for the classical trajectory calculations within the sudden approximation, as a result of which the trajectories were independent of the laser intensity I_0 and the temporal pulse width Γ.

4.3 Simulation of time-dependent XPD profiles

4.3.1 I$_2$ molecules

We considered time-resolved XPD imaging for the photoexcited dissociation process of I$_2$ molecules with the ultrafast XFEL pulses: Aligned I$_2$ molecules are first excited electronically to the $B\,^3\Pi_u^+$ state by optical laser pulses with center wavelength $\lambda_0 = 485$ nm (206×10^2 cm^{-1}) and temporal width $\Gamma = 50$ fs [154]. Owing to this pump laser, nuclear wave packets created on the specific potential energy surface start to move. Their nuclear dynamics is later probed at a different time delay by means of I $3s$ XPD profiles of I$_2$ molecules with XFEL pulses. In this pump–probe scheme, the polarization vectors of the two lasers are parallel to the molecular axis of the aligned I$_2$ molecules.

To calculate the vibrational wave packets on the $B\,^3\Pi_u^+$ state, we used the spectroscopic constants of the dissociation energy D_e, equilibrium internuclear distance R_e, and fundamental frequency ω_e for the infrared spectrum given in Refs. [155, 156], and the analytical forms of transition moments given in Ref. [157]. The relevant potential energy curves in the form of the Morse potential [158–161], $V(R) = D_e\{\exp[-\alpha(R - R_e)] - 1\}^2$, where $\alpha = \sqrt{\mu\omega_e^2/2D_e}$, are
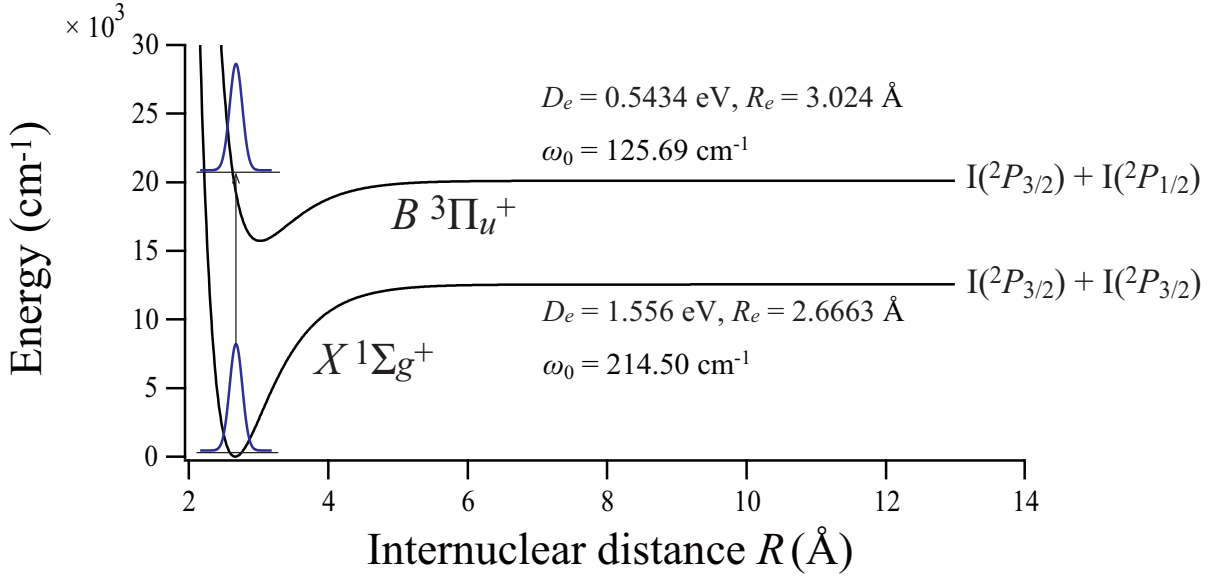
Figure 4.3.1: Potential energy curves of an I_2 molecule. A vibrational wave packet is induced on the $B\,{}^3\Pi_u^+$ state.

shown in Fig. 4.3.1. The reduced mass of I_2 molecules is half of the atomic mass of an iodine atom. To examine the laser intensity I_0 dependence of vibrational wave packet evolution, we calculated the vibrational wave packets for both $I_0 = 1.0 \times 10^{12}$ W/cm^2 and $I_0 = 1.0 \times 10^{13}$ W/cm^2. Fig. 4.3.2 shows the simulation results of the vibrational wave packet evolution. For $I_0 = 1.0 \times 10^{12}$ W/cm^2, the nuclear wave packets simply spread and move on the potential curve. By contrast, for $I_0 = 1.0 \times 10^{13}$ W/cm^2, the nuclear wave packet splits into two peaks. This interesting phenomenon may be due to Rabi oscillations for two-level systems with radiation fields satisfying resonant conditions [162]. The time evolution of the probability densities, which are obtained by integrals of $|\chi_{g(e)}(\boldsymbol{R}, \tau)|^2$ over the stretching nuclear coordinate $\boldsymbol{R}$, are examined and plotted in Fig. 4.3.3. The molecular ensemble irradiated by the optical laser pulse with $I_0 = 1.0 \times 10^{13}$ experiences photoabsorption process and successive photoemission process, whereas that irradiated by the pulse with $I_0 = 1.0 \times 10^{12}$ only undergoes photoabsorption process. This dependence to the laser intensity is consistent with that of the angular frequency for the Rabi's formula [162].

In our calculations of the XPD profile $d\sigma(\boldsymbol{R})/d\hat{\boldsymbol{k}}$, we selected an XFEL photon energy of 1222 eV, which is 150 eV above the I $3s$ ionization threshold of 1072 eV [163]. Photoemissions from the gerade and ungerade molecular orbitals of the I_2 molecules cannot be resolved with the broad band-pass characteristic of XFEL; hence, the XPD profile was calculated as the incoherent sum
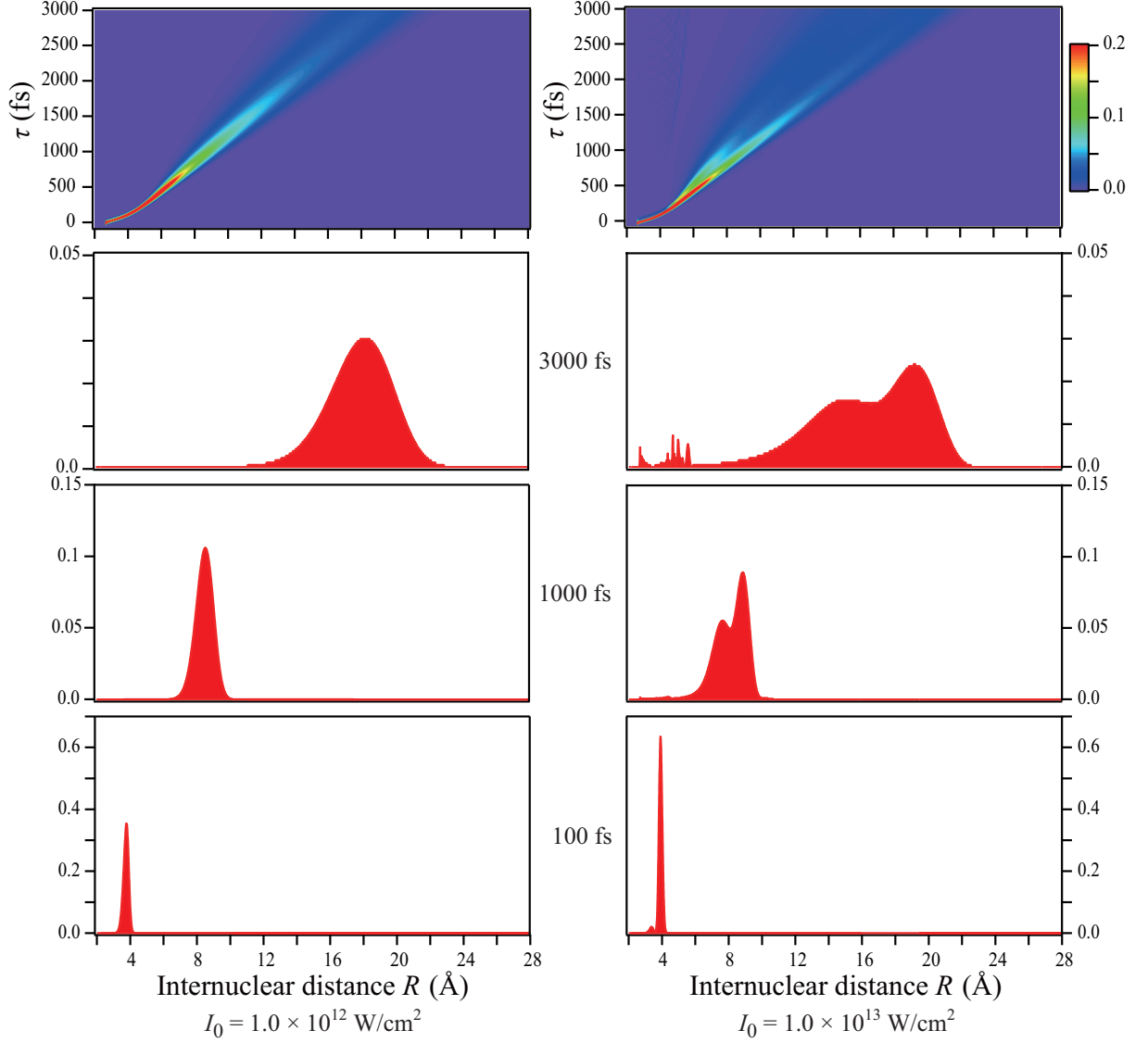
Figure 4.3.2: Nuclear wave packet evolutions on the $B\,^3\Pi_u^+$ state of the I_2 molecule. Left column: laser intensity $I_0 = 1.0 \times 10^{12}$ W/cm^2 with pulse width $\Gamma = 50$ fs. Right column: laser intensity $I_0 = 1.0 \times 10^{13}$ W/cm^2 with pulse width $\Gamma = 50$ fs. Upper panels: wave packet evolutions expressed as functions of the delay time τ and internuclear distance R. Lower panels: cross sections at $\tau = 100$, 1000 and 3000 fs of the upper panels. The vertical scales of $|\chi_e(\boldsymbol{R},\tau)|^2$ are normalized intensities. The norm of $\chi_g(\boldsymbol{R},\tau)$ is normalized to unity so that the integral of $|\chi_e(\boldsymbol{R},\tau)|^2$ over the stretching nuclear coordinate $\boldsymbol{R}$ yields the population of the electronic excited state.
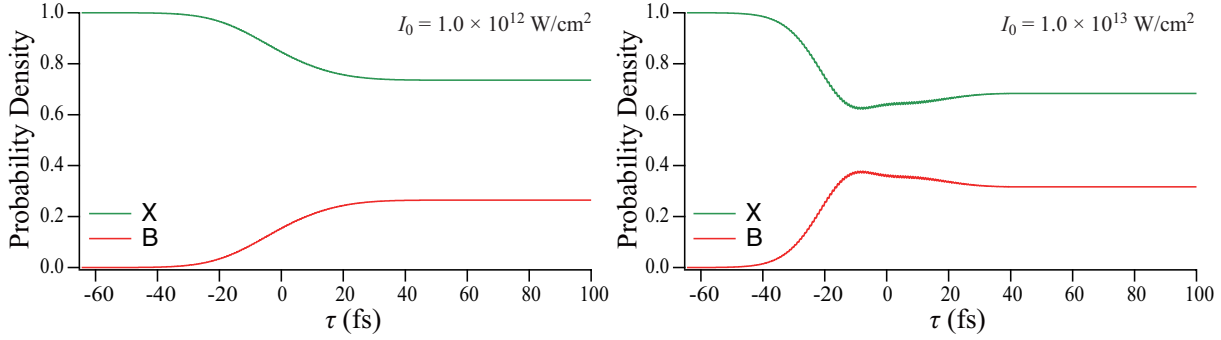
Figure 4.3.3: Time evolution of the probability densities among the $X\,^1\Sigma_g^+$ and $B\,^3\Pi_u^+$ electronic states of I_2 molecules for the laser intensity $I_0 = 1.0 \times 10^{12}$ W/cm^2 and $I_0 = 1.0 \times 10^{13}$ W/cm^2.

of the profiles from the left and right I atoms in the I_2 molecules. Next, by using the vibrational wave packet evolution results on the $B\,^3\Pi_u^+$ state and the XPD profile $d\sigma(\boldsymbol{R})/d\hat{\boldsymbol{k}}$, we simulated the time-resolved I 3s XPD profiles of the I_2 molecules probed by the ultrafast XFEL pulses as functions of the pump–probe delay time τ. The time-resolved I 3s XPD profiles, induced by the pump laser with $I_0 = 1.0 \times 10^{12}$ W/cm^2 and $I_0 = 1.0 \times 10^{13}$ W/cm^2 are shown in Fig. 4.3.4. For comparison, the XPD profiles for a classical trajectory of the nuclear motions are also shown. The integrated areas of the XPD profiles are normalized to unity. As can be observed from Fig. 4.3.4, overall, the time-resolved XPD profiles on a path of the nuclear wave packet evolution and those on the classical trajectory are similar to each other. However, we can observe that the fine structures of the XPD profiles for the classical trajectory are blurred compared to those based on the wave packet calculations owing to the conspicuous spreads of the nuclear wave packets at $\tau = 1000$ and 3000 fs, particularly for $I_0 = 1.0 \times 10^{13}$ W/cm^2 (see Fig. 4.3.4).

4.3.2   CS$_2$ molecules

In this section, we discuss the time-resolved XPD imaging of photochemical reactions of CS_2 molecules. In these molecules, bending vibrational motions are induced by $^1\Sigma_g^+ \rightarrow {}^1B_2\,(^1\Sigma_u^+)$ excitation using optical laser pulses with center wavelength $\lambda_0 = 198$ nm $(505 \times 10^2$ cm$^{-1})$ and laser intensity $I_0 = 3.0 \times 10^{11}$ W/cm^2 [164]. The nuclear dynamics is probed by means of time-resolved C 1s XPD profiles of CS_2 molecules with ultrafast XFEL pulses at different time delays. The polarization vector of the pump laser is perpendicular to the S–S direction of CS_2 molecules and that of the probe laser is parallel to the direction in the simulations. We used the potential energy curve of a 1D quadrupole curve along the S–C–S bond angle, which was derived by Douglas *et al.* [164] and Arendt *et al.* [165]. Such a potential curve is plotted in Fig. 4.3.5.
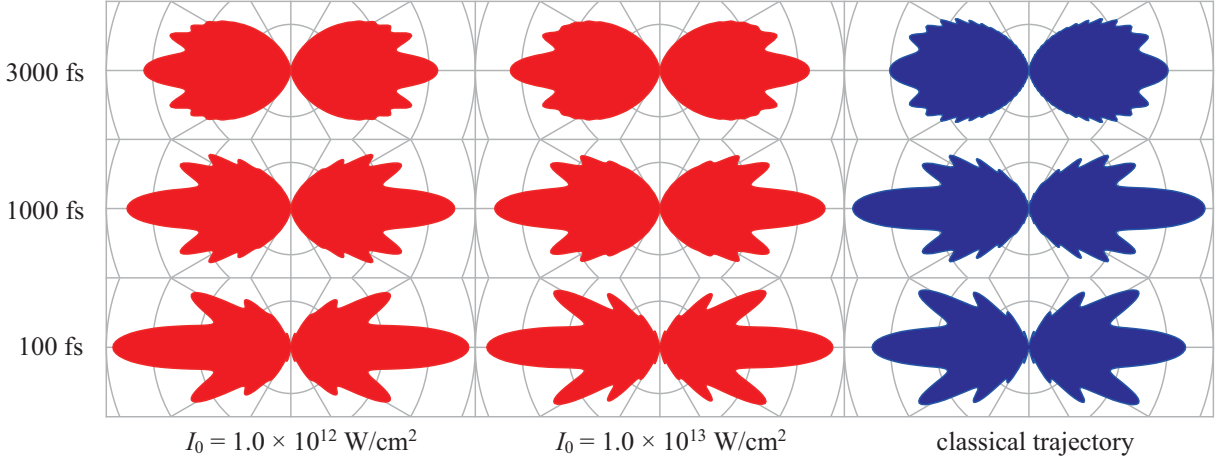
Figure 4.3.4: Time-resolved I $3s$ X-ray photoelectron diffraction (XPD) profiles of I_2 molecules. The delay times are stated on the left of the panel. Left: laser intensity $I_0 = 1.0 \times 10^{12}$ W/cm^2 with pulse width $\Gamma = 50$ fs, middle: laser intensity $I_0 = 1.0 \times 10^{13}$ W/cm^2 with pulse width $\Gamma = 50$ fs, and right: a classical trajectory.

Further, we used the dipole moment for the $^1\Sigma_g^+ \rightarrow {}^1B_2\,(^1\Sigma_u^+)$ transition, i.e., the oscillator strength ($f = 1.024$) averaged over all the geometries in the Franck-Condon region in Ref. [166]. The normal coordinates for the bending vibration of a molecule in the $D_{\infty h}$ symmetry point group are derived in Appendix A. To investigate the pulse width dependence on vibrational wave packet evolutions, we calculated the vibrational wave packets for $\Gamma = 7$ fs and $\Gamma = 20$ fs at laser intensity $I_0 = 3.0 \times 10^{11}$ W/cm^2. Fig. 4.3.6 shows the simulation results. The nuclear wave packets exhibit oscillatory motions for both cases: for $\Gamma = 7$ fs, the wave packet concentrated on the linear structure at $\tau = 80$ fs nearly revives at $\tau = 160$ fs, and for $\Gamma = 20$ fs, the wave packet concentrated on the linear structure at $\tau = 50$ fs nearly revives at $\tau = 130$ fs. The interval of 80 fs is consistent with the experimentally observed periods of the oscillation in the results of time-resolved photoelectron imaging by Horio *et al.* [167, 168], who prepared the wave packets by means of a pump laser with $\Gamma = 7$ fs and $I_0 = 3.0 \times 10^{11}$ W/cm^2. However, it should be emphasized that the oscillation phases of the nuclear wave packets for $\Gamma = 7$ fs and $\Gamma = 20$ fs are different from each other. In order to clarify the effect of the temporal pulse width Γ of the optical laser pulse on the photoexcitation process, the time evolution of the probability densities, which are obtained by integrals of $|\chi_{g(e)}(\boldsymbol{R}, \tau)|^2$ over the bending nuclear coordinate $\boldsymbol{R}$ are examined and plotted in Fig. 4.3.7. The molecular ensemble irradiated by the optical laser pulse with $\Gamma = 20$ fs experiences both photoabsorption and photoemission processes, this is not the case for that irradiated by the pulse with $\Gamma = 7$ fs. This indicates that not only the
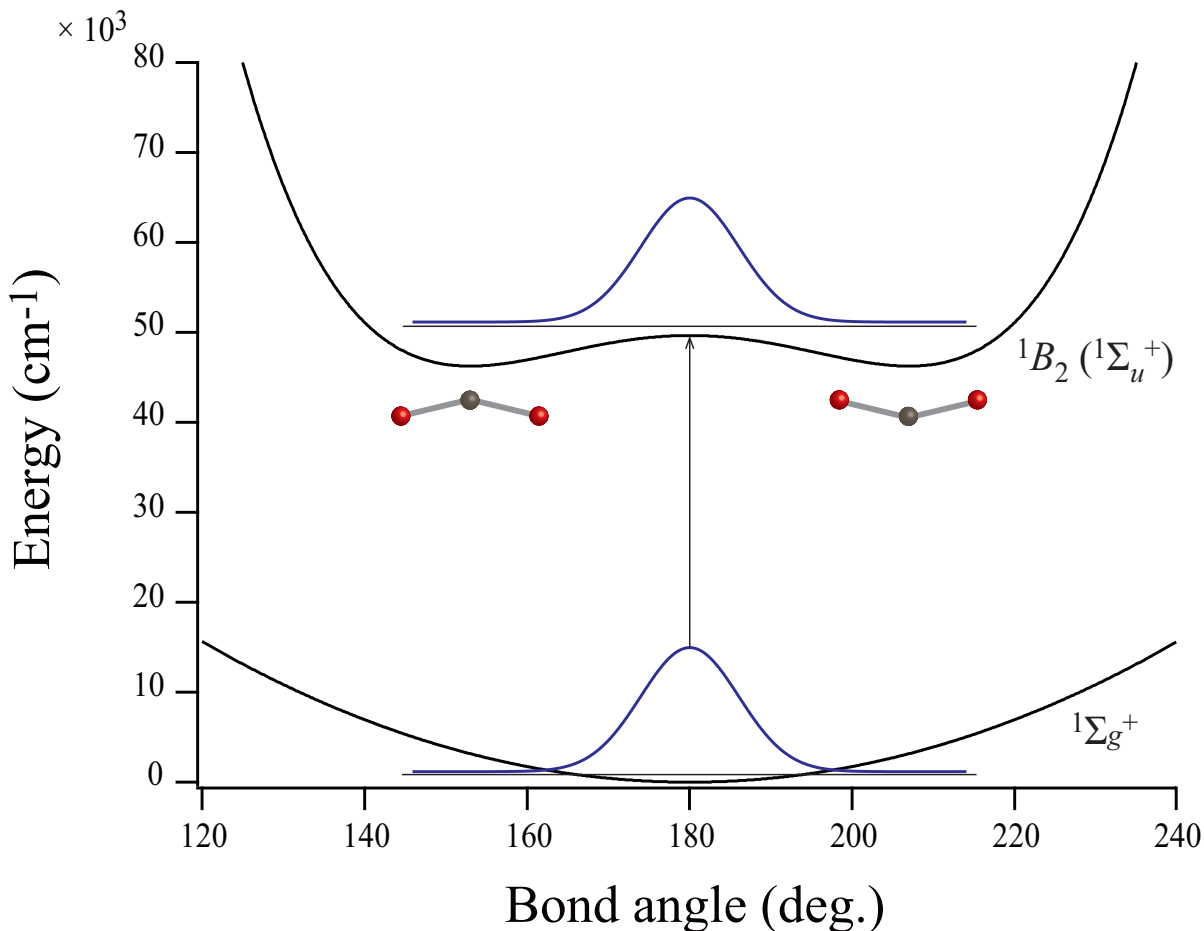
Figure 4.3.5: Potential energy curves of a CS_2 molecule. A vibrational wave packet is induced on the $^1B_2$ state.

laser intensity but also the temporal pulse width dominate the time evolution processes when the pulse width is comparable with the period of Rabi oscillation [162].

We simulated the time-resolved C $1s$ XPD profiles of CS_2 molecules probed by ultrafast XFEL pulses as functions of the pump–probe delay time τ by using the vibrational wave packet evolutions on the $^1B_2\,(^1\Sigma_u^+)$ state and the XPD profiles $d\sigma(\boldsymbol{R})/d\hat{\boldsymbol{k}}$. In the calculations of the XPD profiles at a fixed bond angle, we selected an XFEL photon energy of 413 eV, which is 120 eV above the C $1s$ ionization threshold of 293 eV [169]. Figure 4.3.8 shows the simulation results of the time-resolved C $1s$ XPD profiles. The areas surrounding the XPD profiles are normalized to unity. In the classical trajectory calculations, we prepared the excited states through the sudden approximation. In this approximation, the relevant trajectories are irrelevant to the pulse width.

The time-resolved XPD profiles for $\Gamma = 7$ fs and $\Gamma = 20$ fs and the classical-trajectory exhibit
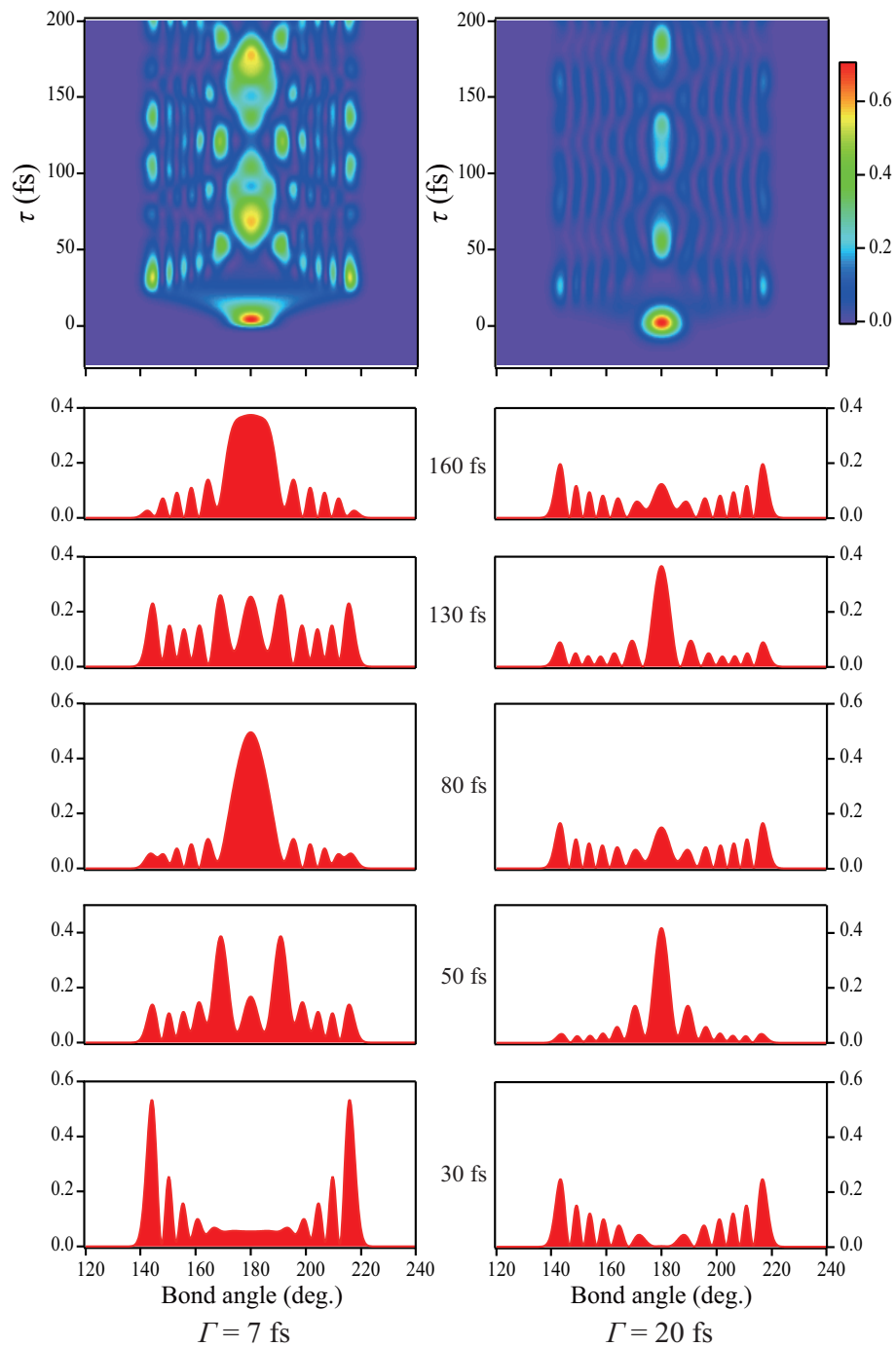
Figure 4.3.6: Nuclear wave packet evolutions on the $^1B_2$ state of the CS_2 molecule. Left column: laser intensity $I_0 = 3.0 \times 10^{11}$ W/cm^2 with pulse width $\Gamma = 7$ fs. Right column: laser intensity $I_0 = 3.0 \times 10^{11}$ W/cm^2 with pulse width $\Gamma = 20$ fs. Upper panels: wave packet evolutions expressed as functions of the delay time τ and S–C–S bond angle. Lower panels: cross sections at delay times $\tau = 30, 50, 80, 130$, and 160 fs of the upper panels. The vertical scales of $|\chi_e(\boldsymbol{R}, \tau)|^2$ are normalized intensities; the norm of $\chi_g(\boldsymbol{R}, \tau)$ is normalized to unity so that the integral of $|\chi_e(\boldsymbol{R}, \tau)|^2$ over the bending nuclear coordinate $\boldsymbol{R}$ yields the population of the electronic excited state.
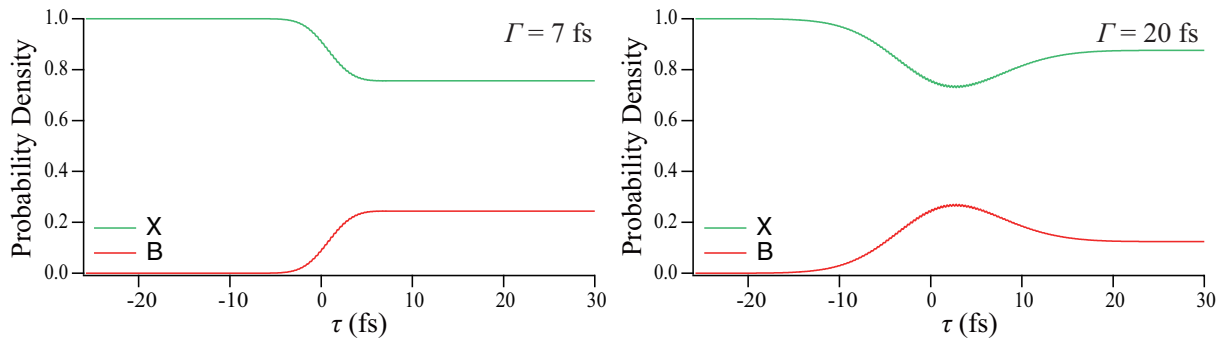
Figure 4.3.7: Time evolution of the probability densities among the $^1\Sigma_g^+$ and $^1B_2$ ($^1\Sigma_u^+$) electronic states of CS_2 molecules for the temporal pulse width of $\Gamma = 7$ fs and $\Gamma = 20$ fs.

striking differences in terms of their oscillation phases and shapes, reflecting the remarkable differences in the nuclear wave packet evolutions for $\Gamma = 7$ fs and $\Gamma = 20$ fs. In contrast to the vibrational wave packets of the I_2 molecules, the bending vibrational wave packets of the CS_2 molecules change the molecular symmetry from $D_{\infty h}$ to C_{2v}. This necessarily causes a considerable change in the overall molecular structure of the CS_2 molecules. Consequently, the time-dependent XPD profiles $d\sigma(\boldsymbol{R}, \tau)/d\hat{\boldsymbol{k}}$ of the CS_2 molecules are highly sensitive to changes in the molecular structure, as can be observed from Figs. 4.3.6 and 4.3.8. This is because the time-dependent XPD profiles $d\sigma(\boldsymbol{R}, \tau)/d\hat{\boldsymbol{k}}$ reflect the transient molecular structure at the delay time τ, which varies considerably during the molecular symmetry change from $D_{\infty h}$ to C_{2v}.
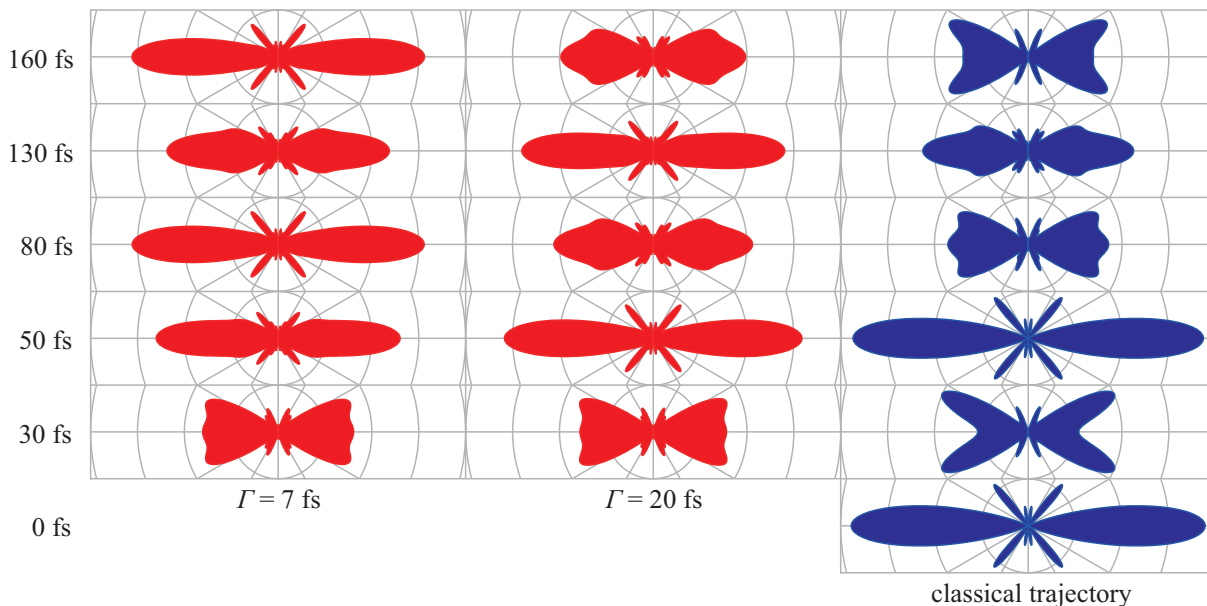
Figure 4.3.8: Time-resolved C $1s$ X-ray photoelectron diffraction (XPD) profiles of CS_2 molecules. The delay times are stated on the left of the panel. Left: laser intensity $I_0 = 3.0 \times 10^{11}$ W/cm^2 with pulse width $\Gamma = 7$ fs, middle: laser intensity $I_0 = 3.0 \times 10^{11}$ W/cm^2 with pulse width $\Gamma = 20$ fs, and right: a classical trajectory.

4.4 Summary

Based on both the nuclear wave packet and the MS-XPD calculations, we performed simulations of the time-dependent XPD profiles, which can be measured by the pump–probe experimental scheme. Our results raise the following points of interest. The time-dependent I_2 I $3s$ XPD profiles obtained using the nuclear wave packet evolutions are similar to those predicted by the classical trajectory for nuclear motions, although the fine structures in the latter are blurred in the former by the spread of the nuclear wave packet. For CS_2 molecules, the bending vibrational wave packets depending on the temporal pulse widths of the pump lasers exhibit complicated shapes, and their oscillation periods differ from that for the classical trajectory. Accordingly, the time-dependent C $1s$ XPD profiles based on the wave packet calculations are strikingly different from those of the classical motions.

Recently, direct measurements of vibrational wave packets of I_2 molecules have been reported by means of ultrafast electron diffraction [114] and X-ray diffraction [113]. The former has demonstrated high sensitivity not only to the position but also to the shape of the periodic vibrational wave packets. The latter approach has succeeded in visualizing dispersion, dissociation, and rotational dephasing of the wave packets. These promising results encourage researchers, who are developing ultrafast XPD in gas-phase molecules in their imaging studies, because the photoionization cross sections are considerably larger than the cross sections of X-ray scattering and high-energy electron scattering.

4.5 Appendix: General formula for the time-resolved XPD

Consider a time-resolved XPD experiment in an optical-laser pump–XFEL probe scheme. The optical laser pulse appears at $t = -t_{\mathrm{op}}$ and vanishes at $t = t_{\mathrm{op}}$. The XFEL pulse appears at t_{pr}, which is later than t_{op}, and the photoelectron is detected at $\tau > t_{\mathrm{pr}}$.

The interaction representation of wave functions and operators are introduced as

$$\varphi_I(t) = e^{iH_0 t} \varphi(t), \tag{4.5.1}$$

$$A_I(t) = e^{iH_0 t} A(t) e^{-iH_0 t}, \tag{4.5.2}$$

where H_0 is the Hamiltonian for the molecule without radiation field, $\varphi(t)$ and $A(t)$ are a wave

function and an operator in the Schrödinger representation, respectively. Time evolution from t_1 to t_2 of a wave function in the interaction representation is achieved by the operator given in Dyson series as

$$U_I(t_2, t_1) = \sum_{m=0}^{\infty} (-i)^m \int_{t_1}^{t_2} dt' \int_{t_1}^{t'} dt'' \cdots \int_{t_1}^{t^{(n-1)}} dt^{(n)} V_I(t') V_I(t'') \cdots V_I(t^{(n)}), \qquad (4.5.3)$$

where $V_I(t)$ is the perturbation potential in the interaction representation.

The molecular wave function $\Psi(\boldsymbol{R}, \boldsymbol{r}, t)$, where $\boldsymbol{R}$ and $\boldsymbol{r}$ represent the spacial coordinates of nuclei and electrons, respectively, is expanded by the Born-Oppenheimer basis set $\{\Phi_n(\boldsymbol{r}; \boldsymbol{R})\chi_v^{(n)}(\boldsymbol{R})\}_{nv}$. With the initial condition of

$$\Psi_I(\boldsymbol{R}, \boldsymbol{r}, t = -t_{\mathrm{op}}) = \Phi_0(\boldsymbol{r}; \boldsymbol{R})\chi_0^{(0)}(\boldsymbol{R}), \qquad (4.5.4)$$

the molecular wave function at a certain delay time t ($t_{\mathrm{pr}} > t > t_{\mathrm{op}}$) in the interaction representation is given by

$$
\begin{aligned}
\Psi_I(\boldsymbol{R}, \boldsymbol{r}, t) &= U_I(t_{\mathrm{op}}, -t_{\mathrm{op}})\Phi_0(\boldsymbol{r}; \boldsymbol{R})\chi_0^{(0)}(\boldsymbol{R}) \\
&= \int d\boldsymbol{r}' \int d\boldsymbol{R}' \delta(\boldsymbol{r} - \boldsymbol{r}')\delta(\boldsymbol{R} - \boldsymbol{R}')U_I(t_{\mathrm{op}}, -t_{\mathrm{op}})\Phi_0(\boldsymbol{r}; \boldsymbol{R})\chi_0^{(0)}(\boldsymbol{R}) \\
&= \sum_n \sum_v \left(\int d\boldsymbol{r}' \int d\boldsymbol{R}' \chi_{I,v}^{(n)*}(\boldsymbol{R}')\Phi_{I,n}^*(\boldsymbol{r}'; \boldsymbol{R}')U_I(t_{\mathrm{op}}, -t_{\mathrm{op}})\Phi_0(\boldsymbol{r}'; \boldsymbol{R}')\chi_0^{(0)}(\boldsymbol{R}') \right) \\
&\quad \times \Phi_{I,n}(\boldsymbol{r}; \boldsymbol{R})\chi_{I,v}^{(n)}(\boldsymbol{R}) \\
&= \sum_n \sum_v c_{nv}^{\mathrm{op}} \Phi_{I,n}(\boldsymbol{r}; \boldsymbol{R})\chi_{I,v}^{(n)}(\boldsymbol{R}),
\end{aligned}
$$

$$(4.5.5)$$

where the closure relations

$$\sum_n \Phi_{I,n}(\boldsymbol{r}; \boldsymbol{R})\Phi_{I,n}^*(\boldsymbol{r}'; \boldsymbol{R}') = \delta(\boldsymbol{r} - \boldsymbol{r}'), \qquad (4.5.6)$$

$$\sum_v \chi_{I,v}^{(n)}(\boldsymbol{R})\chi_{I,v}^{(n)*}(\boldsymbol{R}') = \delta(\boldsymbol{R} - \boldsymbol{R}'), \qquad (4.5.7)$$

are used and the coefficients

$$c_{nv}^{\mathrm{op}} = \int d\boldsymbol{r}' \int d\boldsymbol{R}' \chi_{I,v}^{(n)*}(\boldsymbol{R}')\Phi_{I,n}^*(\boldsymbol{r}'; \boldsymbol{R}')U_I(t_{\mathrm{op}}, -t_{\mathrm{op}})\Phi_0(\boldsymbol{r}'; \boldsymbol{R}')\chi_0^{(0)}(\boldsymbol{R}') \qquad (4.5.8)$$

are introduced. Then the molecular wave function at the time τ of photoelectron detection is expanded as

$$
\begin{aligned}
\Psi_I(\boldsymbol{R},\boldsymbol{r},\tau) &= U_I(\tau,t)\Psi_I(\boldsymbol{R},\boldsymbol{r},t) \\
&= U_I(\tau,t_{\mathrm{pr}})\Psi_I(\boldsymbol{R},\boldsymbol{r},t) \\
&= \sum_n \sum_v c_{nv}^{\mathrm{op}} U_I(\tau,t_{\mathrm{pr}})\Phi_{I,n}(\boldsymbol{r};\boldsymbol{R})\chi_{I,v}^{(n)}(\boldsymbol{R}) \\
&= \int d\boldsymbol{r}'' \int d\boldsymbol{R}'' \delta(\boldsymbol{r}-\boldsymbol{r}'')\delta(\boldsymbol{R}-\boldsymbol{R}'') \sum_n \sum_v c_{nv}^{\mathrm{op}} U_I(\tau,t_{\mathrm{pr}})\Phi_{I,n}(\boldsymbol{r}'';\boldsymbol{R}'')\chi_{I,v}^{(n)}(\boldsymbol{R}'') \\
&= \int d\boldsymbol{k} \sum_{n'} \sum_{v'} \Big[\int d\boldsymbol{r}'' \int d\boldsymbol{R}'' \chi_{I,v'}^{(n')*}(\boldsymbol{R}'') \det\!\big(\psi_{\boldsymbol{k}}^- \Phi_{h,n'}\big)_I^*(\boldsymbol{r}'';\boldsymbol{R}'') \\
&\quad \times \sum_n \sum_v c_{nv}^{\mathrm{op}} U_I(\tau,t_{\mathrm{pr}})\Phi_{I,n}(\boldsymbol{r}'';\boldsymbol{R}'')\chi_{I,v}^{(n)}(\boldsymbol{R}'') \Big] \det\!\big(\psi_{\boldsymbol{k}}^- \Phi_{h,n'}\big)_I(\boldsymbol{r};\boldsymbol{R})\chi_{I,v'}^{(n')}(\boldsymbol{R}),
\end{aligned}
$$

$$(4.5.9)$$

where $\det\!\big(\psi_{\boldsymbol{k}}^- \Phi_{h,n'}\big)(\boldsymbol{r};\boldsymbol{R})$ is the Slater determinant of the photoelectron wave function $\psi_{\boldsymbol{k}}^-$ and the electronic wave function of the residue ion $\Phi_{h,n'}$.

Suppose that the electronic and vibrational states of the residue ion are not resolved for the photoelectron detection. Then the photoionization cross section is an incoherent superposition of those for all electronic and vibrational states, because the system composed of the photoelectron and the residue ion contracts to an energy eigenstate for the photoelectron detection. In this case, the differential cross section is simplified using the closure relation Eq. (4.5.7) as

$$
\begin{aligned}
\frac{d\sigma(\tau)}{d\boldsymbol{k}} &\propto \sum_{n'} \sum_{v'} \Big| \int d\boldsymbol{r}'' \int d\boldsymbol{R}'' \chi_{I,v'}^{(n')*}(\boldsymbol{R}'') \det\!\big(\psi_{\boldsymbol{k}}^- \Phi_{h,n'}\big)_I^*(\boldsymbol{r}'';\boldsymbol{R}'') \\
&\quad \times \sum_n \sum_v c_{nv}^{\mathrm{op}} U_I(\tau,t_{\mathrm{pr}})\Phi_{I,n}(\boldsymbol{r}'';\boldsymbol{R}'')\chi_{I,v}^{(n)}(\boldsymbol{R}'') \Big|^2 \\
&= \sum_{n'} \int d\boldsymbol{R}'' \Big| \int d\boldsymbol{r}'' \det\!\big(\psi_{\boldsymbol{k}}^- \Phi_{h,n'}\big)_I^*(\boldsymbol{r}'';\boldsymbol{R}'') \sum_n \sum_v c_{nv}^{\mathrm{op}} U_I(\tau,t_{\mathrm{pr}})\Phi_{I,n}(\boldsymbol{r}'';\boldsymbol{R}'')\chi_{I,v}^{(n)}(\boldsymbol{R}'') \Big|^2.
\end{aligned}
$$

$$(4.5.10)$$

If the same one-electron molecular basis set is used for the wave functions of the electronic excited state $\Phi_{I,n}(\boldsymbol{r}'';\boldsymbol{R}'')$ and the final state $\det\!\big(\psi_{\boldsymbol{k}}^- \Phi_{h,n'}\big)_I(\boldsymbol{r}'';\boldsymbol{R}'')$, the n-electron integral reduces to a one-electron integral in Eq. (4.5.10). Using the relation between the interaction and the Schrödinger representations Eq. (4.5.1, 4.5.2), and applying the sudden approximation,

the differential cross section is recast as

$$\frac{d\sigma(\tau)}{d\boldsymbol{k}} \propto \sum_{n'} \int d\boldsymbol{R}'' \left| \int d\boldsymbol{r}_A \psi_{\boldsymbol{k}}^{-*}(\boldsymbol{r}_A; \boldsymbol{R}'') V^{\mathrm{pr}} \phi_c(\boldsymbol{r}_A) \right|^2 \left| \mathrm{X}^{(n')}(\boldsymbol{R}'', \tau) \right|^2, \tag{4.5.11}$$

where $\phi_c(\boldsymbol{r}_A)$ is the core orbital from which the photoelectron is ejected, and V^{pr} is the interaction potential between the core electron and the XFEL. The nuclear wave packet of the electronic state n', $\mathrm{X}^{(n')}(\boldsymbol{R}'', \tau)$, is defined by

$$\mathrm{X}^{(n')}(\boldsymbol{R}'', \tau) = \sum_v c_{n'v}^{\mathrm{op}} \exp(-iE_v^{(n')}\tau) \chi_v^{(n')}(\boldsymbol{R}''), \tag{4.5.12}$$

where $E_v^{(n')}$ is the energy eigenvalue corresponding to the vibrational wave function $\chi_v^{(n')}(\boldsymbol{R}'')$. The Chase adiabatic approximation [151] is employed in Eq. (4.5.11), i.e., it is assumed that the magnitudes of the expansion coefficients of the nuclear wave packets are unchanged th the instant of photoionization.

For the practical calculation, the nuclear wave packets are obtained by the numerical integral of the time-dependent Schrödinger equation under the two-level approximation. The procedure is described in Sec. 4.2.

Appendix A

C $1s$ PAD in recoil frame for CO$^+$–O$^+$
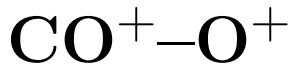
A.1   Introduction

In an axial recoil approximation process, the two fragments of diatomic molecules fly off exactly anti-parallel to each other. If the dissociation is initiated by the ejection of an electron, and that electron is detected in coincidence with one and/or two ionic fragments, then the electron is tied to the direction of the molecular axis at the moment of dissociation. If we assume that this entire process takes place on a timescale that is shorter than a rotational period, the measurement of the RFPAD is equivalent to that ot the MFPAD referenced in the direction of the breaking bond [51–53]. This basic idea to obtain the MFPAD has been applied to polyatomic molecules having linear equilibrium geometry [65, 68–72]. Here a question arises as to whether PADs detected in coincidence with the fragment ion pairs of the linear polyatomic molecules are equivalent to the MFPAD. This is mainly because on the one hand, the instantaneous character of the photoemission samples the entire geometries for an ensemble of molecules having zero-point vibrational motions, whereas on the other hand, the two-body fragmentation measurement of the linear polyatomic molecules does not provide information about the relevant geometries (see Fig. A.1.1).

Since, for example, the CO$_2$ molecule is a "linear" molecule, at first grance, one might expect the most probable bond angle to be 180°for an ensemble of molecules. However, the CO$_2$ molecule has three zero-point vibrational motions: symmetric stretching, anti-symmetric
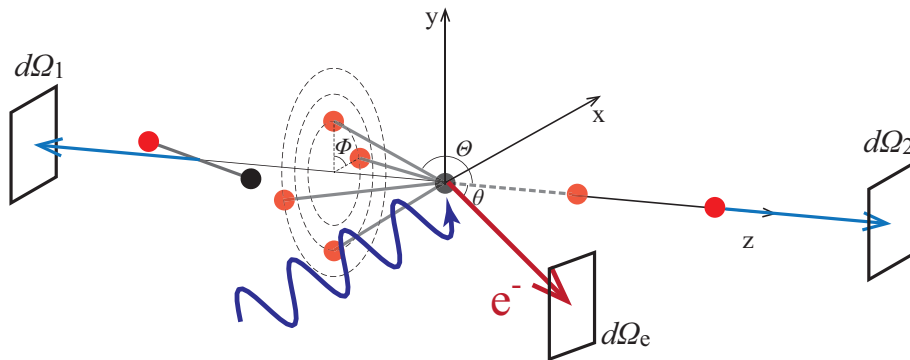
Figure A.1.1: Conceptual drawing of photoelectron–photoion coincidence measurement for a 'linear' triatomic molecule. The solid angles $d\Omega_e, d\Omega_1, d\Omega_2$ are acceptance angles of the photoelectron and fragment ions, respectively.

stretching, and two degenerate bending motions. Then, a snapshot of the molecule at the instant of photoionization will only show a linear geometry if both bending vibrations pass through the equilibrium configuration at that time, which is quite improbable. In reality, although the bending vibration function has a peak at the bond angle of 180°, the bond-angle population function has a peak at a somewhat smaller angle than 180°, see Fig. A.2.3 and also Refs. [170–174]. As a natural consequence, in previous studies [66, 67] on C 1s, PADs detected in coincidence with the fragment ion pairs of CO^+–O^+ are not MFPADs but RFPADs. Thus, the azimuthal angle distributions of the CO^+ fragment relative to the recoil axis are averaged in the experimental data of the previous studies. It should be emphasized that this geometrical effect on the zero-point motion has been overlooked thus far.

In this Appendix, we report the experimental results on C 1s RFPADs for the CO^+–O^+ fragment ion pair, which were obtained by Adachi *et al.* by using the undulator beam line BL-2C of the Photon Factory multi-coincidence velocity-map imaging spectrometer [73, 74]. These measurements were carried out at photoelectron energies of 85, 120 and 150 eV to avoid the broad shape resonance peak centered at ∼20 eV [175]. To account for our left-right asymmetric C 1s RFPADs from CO^+–O^+, we propose a simple model based on the MS-XPD theory [39, 40]. Photoelectron scattering within a molecule in the high-energy off-resonance region is well described by the proposed model [75, 76, 78]. Using the model, we calculated C 1s PADs by considering the entire geometries for an ensemble of molecules having zero-point vibrational motions. The experimentally obtained asymmetric C 1s RFPADs are well reproduced by the calculated results. More importantly, in contrast to the theoretical results of Miyabe *et al.* [176, 177], our theoretical results reveal that the issue of the asymmetric C 1s RFPADs is not

due to the anti-symmetric zero-point stretching vibration but due to the two degenerate zero-point bending vibrations.

A.2 Bond-angle population function of CO$_2$ molecules

The classical Hamiltonian for vibration of a multi-atomic molecule is given by

$$
\begin{aligned}
H = & \sum_{\alpha i} \frac{p_{\alpha i}^2}{2m_\alpha} + V_0 + \sum_\alpha \sum_{i=x,y,z} \left(\frac{\partial V}{\partial x_{\alpha i}}\right)\Big|_0 (x_{\alpha i} - x_{\alpha i 0}) \\
& + \frac{1}{2} \sum_\alpha \sum_{i=x,y,z} \sum_\beta \sum_{j=x,y,z} \left(\frac{\partial^2 V}{\partial x_{\alpha i} \partial x_{\beta j}}\right)\Big|_0 (x_{\alpha i} - x_{\alpha i 0})(x_{\beta j} - x_{\beta j 0}) + \cdots .
\end{aligned}
\tag{A.2.1}
$$

To quantize the molecular vibration, cross terms for the potential must be eliminated as follows:

$$
H = \sum_k \frac{P_k^2}{2} + \sum_k \frac{\omega_k^2 Q_k^2}{2}
\tag{A.2.2}
$$

under the harmonic approximation. The coordinate Q_k has the dimension $(\text{mass})^{1/2}(\text{length})$ and is called the normal coordinate. The normal coordinate is given by a linear combination of atomic displacements. The conjugate momentum of Q_k is represented by P_k.

CO$_2$ is a linear triatomic molecule having four degrees of freedom. Although normal coordinates are generally given by linear combinations of atomic displacements in Cartesian coordinates [158, 178–180], the GF-matrix method using internal coordinates is more elegant in the cases of small molecules [178]. In the following subsections, the general description of the GF-matrix method is given, and the normal coordinates of CO$_2$ are derived in the subsequent subsection.

A.2.1 GF-matrix method

The coordinate s_t represents an internal coordinate such as bond length and bond angle. The matrix B relating s_t and atomic infinitesimal displacement in the Cartesian coordinate ξ_i is defined by

$$
s_t = \sum_{i=1}^{3N} B_{ti}\xi_i \quad t = 3N - 6.
\tag{A.2.3}
$$

Displacements $\{\xi_i\}_{i=1}^{3N-6}$ refer to $(\Delta x_{1x}, \Delta x_{1y}, \Delta x_{1z}, \Delta x_{2x}, \cdots, \Delta x_{Ny}, \Delta x_{Nz})$. The number of internal coordinates is $3N-6$ even if the molecule is linear at the minimum vibrational potential.

Using the mass-weighed Cartesian coordinate $q_i = \sqrt{m_i}\xi_i$, the kinetic energy is given by

$$T = \frac{1}{2}\sum_i \dot{q}_i{}^2. \tag{A.2.4}$$

A dot over a symbol denotes the time derivative, i.e., $\dot{q}_i = \frac{dq_i}{dt}$. Introducing the conjugate momentum of q_i as

$$p_i = \frac{\partial T}{\partial \dot{q}_i} = \dot{q}_i \tag{A.2.5}$$

gives

$$T = \frac{1}{2}\sum_i p_i^2. \tag{A.2.6}$$

By defining the transformation from the mass-weighted coordinates to the internal coordinates as

$$s_t = \sum_i D_{ti} q_i, \tag{A.2.7}$$

the kinetic energy T is derived as a function of the internal velocity $\dot{s}_t$. Using the chain rule

$$\begin{aligned}
p_i &= \frac{\partial T}{\partial \dot{q}_i} = \sum_t \frac{\partial T}{\partial \dot{s}_t}\frac{\partial \dot{s}_t}{\partial \dot{q}_i} \\
&= \sum_t \frac{\partial T}{\partial \dot{s}_t}\frac{\partial s_t}{\partial q_i} = \sum_t P_t D_{ti}
\end{aligned} \tag{A.2.8}$$

and substituting Eq. (A.2.8) into Eq. (A.2.6) gives

$$T = \frac{1}{2}\sum_t \sum_{t'} \sum_i P_t D_{ti} D_{t'i} P_{t'}, \tag{A.2.9}$$

where P_t is the conjugate momentum of s_t. By defining matrix G as

$$G_{tt'} = \sum_{i=1}^{3N} \frac{1}{m_i} B_{ti} B_{t'i}, \tag{A.2.10}$$

it is related to matrix D in Eq. (A.2.7) and matrix B in Eq. (A.2.3):

$$\sum_i D_{ti} D_{t'i} = \sum_i \frac{1}{m_i} B_{ti} B_{t'i} = G_{tt'}. \tag{A.2.11}$$

Then, the molecular kinetic energy is expressed by

$$T = \frac{1}{2} \sum_{tt'} G_{tt'} P_t P_{t'}.$$ (A.2.12)

By implementing the harmonic approximation as

$$V = \frac{1}{2} \sum_{tt'} F_{tt'} s_t s_{t'},$$ (A.2.13)

the Hamiltonian is expressed in terms of the internal coordinates and their conjugate momenta:

$$H = T + V = \frac{1}{2} \sum_{tt'} G_{tt'} P_t P_{t'} + \frac{1}{2} \sum_{tt'} F_{tt'} s_t s_{t'}.$$ (A.2.14)

The Hamilton equation

$$\dot{s}_t = \frac{\partial H}{\partial P_t}, \quad \dot{P}_t = -\frac{\partial H}{\partial s_t}$$ (A.2.15)

gives the equations of motion for the internal coordinates:

$$\begin{aligned}
\ddot{s}_t &= \frac{d}{dt}\left(\frac{\partial H}{\partial P_t}\right) = \sum_{t'} G_{tt'} \dot{P}_{t'} \\
&= \sum_{t'} G_{tt'}\left(-\frac{\partial H}{\partial s_{t'}}\right) = -\sum_{t'}\sum_{t''} G_{tt'} F_{t't''} s_{t''} \\
&= -\sum_{t''} (GF)_{tt''} s_{t''}.
\end{aligned}$$ (A.2.16)

By representing the internal coordinates in periodic displacements as

$$s_t = s_t^0 e^{i\omega t}$$ (A.2.17)

and substituting them into Eq. (A.2.16), the simultaneous equation

$$\sum_{t'} (GF)_{tt'} s_{t'}^0 = \omega^2 s_t^0$$ (A.2.18)

is derived. Then the proper frequencies are obtained by solving the secular equation

$$|GF - \omega^2 I| = 0.$$ (A.2.19)

To obtain the normal coordinates, a matrix L that relates them to the internal coordinates

as

$$s_t = \sum_k n_k A_{tk} Q_k = \sum_k L_{tk} Q_k \tag{A.2.20}$$

is required, where the vectors $\boldsymbol{A}$ are the eigenvectors of the matrix GF and the factor n_k is

the normalization factor of the normal coordinates. In general, the matrix L is not a diagonal

matrix. Substituting Eq. (A.2.20) into Eq. (A.2.13) transforms the potential:

$$V = \frac{1}{2} \sum_{tt'} \sum_{kk'} F_{tt'} n_k n_{k'} A_{tk} A_{t'k'} Q_k Q_{k'}. \tag{A.2.21}$$

By comparing it with the potential in the harmonic form of the normal coordinates,

$$V = \sum_s \frac{\omega_s^2 Q_s^2}{2}, \tag{A.2.22}$$

the normalization factor of the vector $\boldsymbol{A}$ is obtained:

$$n_k = e^{i\delta} \frac{\omega_k}{\sum_{tt'} F_{tt'} A_{tk} A_{t'k}}. \tag{A.2.23}$$

The phase factor of the normal coordinate $e^{i\delta}$ is arbitrary. By determining the matrix L in this

manner, the normal coordinates are obtained:

$$Q_k = \sum_t (L^{-1})_{kt} s_t. \tag{A.2.24}$$

A.2.2   Application of the GF-matrix method to a CO_2 molecule

Assume that a CO_2 molecule is on the z-axis in its equilibrium geometry and displaces with its

center of mass fixed   (Fig. A.2.1) . The bond lengths Δr_R and Δr_L are of the right and left

C–O bonds in Fig. A.2.1, respectively, and their equilibrium value is represented by r_e. Assume

that all of the constituent atoms are fixed on the zx-plane and the positive direction of the

O–C–O bond angle Θ is from the first quadrant toward the second quadrant. Displacements of
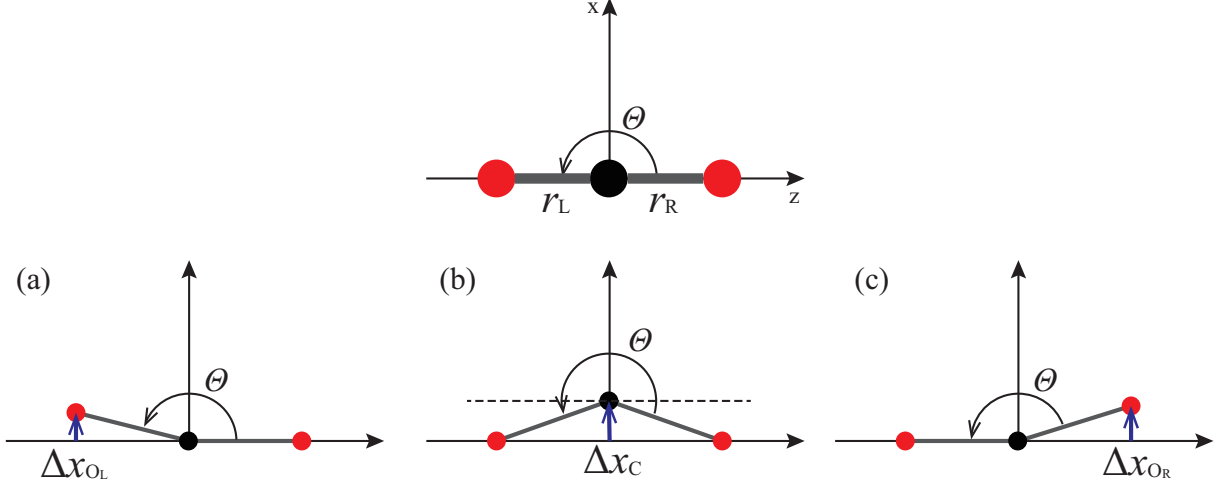
Figure A.2.1: Definitions of the internal coordinates and infinitesimal displacement of the bond angle by positive infinitesimal displacement along the x-axis of (a) the left O, (b) the C, and (c) the right O atoms

the bond angle are related to the atomic displacements in Cartesian coordinates:

$$\Delta r_{\mathrm{R}} = \Delta z_{\mathrm{O_R}} - \Delta z_{\mathrm{C}} \tag{A.2.25}$$

$$\Delta r_{\mathrm{L}} = \Delta z_{\mathrm{C}} - \Delta z_{\mathrm{O_L}}. \tag{A.2.26}$$

Each infinitesimal atomic displacement along the x direction changes the bond angle as

$$\frac{\partial \Theta}{\partial x_{\mathrm{O_R}}} = -\frac{1}{r_e}, \quad \frac{\partial \Theta}{\partial x_{\mathrm{C}}} = \frac{2}{r_e}, \quad \frac{\partial \Theta}{\partial x_{\mathrm{O_L}}} = -\frac{1}{r_e} \tag{A.2.27}$$

with the equilibrium bond length r_e. In this context, the total differential of the bond angle is

$$
\begin{aligned}
\Delta \Theta &= \left(\frac{\partial \Theta}{\partial x_{\mathrm{O_R}}}\right)\Delta x_{\mathrm{O_R}} + \left(\frac{\partial \Theta}{\partial x_{\mathrm{C}}}\right)\Delta x_{\mathrm{C}} + \left(\frac{\partial \Theta}{\partial x_{\mathrm{O_L}}}\right)\Delta x_{\mathrm{O_L}} \\
&= \frac{1}{r_e}(-\Delta x_{\mathrm{O_R}} + 2\Delta x_{\mathrm{C}} - \Delta x_{\mathrm{O_L}}).
\end{aligned}
\tag{A.2.28}
$$

Group-theoretical consideration simplifies the eigenvalue problem of the matrix GF. An atomic displacement along the z-axis direction is invariant under rotation about the molecular axis, whereas displacements along the x- and y-axis directions are transformed under such a rotation

by an azimuthal angle Φ:

$$x \longrightarrow x' = x \cos \Phi - y \sin \Phi$$

$$y \longrightarrow y' = x \sin \Phi + y \cos \Phi. \tag{A.2.29}$$

Thus, the displacement along the z-axis direction is a basis of a one-dimensional irreducible representation of the $D_{\infty h}$ point group, whereas the displacements along the x- and y-axis span a two-dimensional irreducible representation. Because normal coordinates constitute a basis of the relevant point group [180], the former and the latter displacements form separate normal coordinates. Furthermore, the infinitesimal atomic displacements along and perpendicular to the z-axis only change the bond lengths and the bond angle for the equilibrium molecular geometry, respectively. These factors imply that the GF-matrix method can be applied to the changes in the bond lengths and bond angle separately.

First, the GF-matrix method is applied to the bond length displacement. The rows and columns of the matrix B_{bond} are correlated with $\Delta r_{\text{R}}, \Delta r_{\text{L}}$, and $\Delta z_{\text{O}_{\text{R}}}, \Delta z_{\text{C}}, \Delta z_{\text{O}_{\text{L}}}$, respectively:

$$B_{\text{bond}} = \begin{bmatrix} 1 & -1 & 0 \\ 0 & 1 & -1 \end{bmatrix} \tag{A.2.30}$$

Then the matrix G_{bond} is given by

$$G_{\text{bond}} = \begin{bmatrix} \dfrac{1}{m_{\text{O}}} + \dfrac{1}{m_{\text{C}}} & -\dfrac{1}{m_{\text{C}}} \\[3mm] -\dfrac{1}{m_{\text{C}}} & \dfrac{1}{m_{\text{O}}} + \dfrac{1}{m_{\text{C}}} \end{bmatrix}, \tag{A.2.31}$$

where m_{O} and m_{C} are the masses of O and C atoms, respectively. The molecular symmetry imposes the relations

$$\left.\frac{\partial^2 V}{\partial r_{\text{R}}^2}\right|_0 = \left.\frac{\partial^2 V}{\partial r_{\text{L}}^2}\right|_0 = f_{\text{RR}}$$

$$\left.\frac{\partial^2 V}{\partial r_{\text{R}} \partial r_{\text{L}}}\right|_0 = f_{\text{RL}} \tag{A.2.32}$$

on the force constants. Then the matrix F_{bond} is of the form

$$F_{\text{bond}} = \begin{bmatrix} f_{\text{RR}} & f_{\text{RL}} \\ f_{\text{RL}} & f_{\text{RR}} \end{bmatrix}. \tag{A.2.33}$$

Then, the matrix GF is obtained:

$$G_{\text{bond}}F_{\text{bond}} = \begin{bmatrix} f_{\text{RR}}\left(\dfrac{1}{m_{\text{O}}} + \dfrac{1}{m_{\text{C}}}\right) - \dfrac{f_{\text{RL}}}{m_{\text{C}}} & -\dfrac{f_{\text{RR}}}{m_{\text{C}}} + f_{\text{RL}}\left(\dfrac{1}{m_{\text{O}}} + \dfrac{1}{m_{\text{C}}}\right) \\[4mm] -\dfrac{f_{\text{RR}}}{m_{\text{C}}} + f_{\text{RL}}\left(\dfrac{1}{m_{\text{O}}} + \dfrac{1}{m_{\text{C}}}\right) & f_{\text{RR}}\left(\dfrac{1}{m_{\text{O}}} + \dfrac{1}{m_{\text{C}}}\right) - \dfrac{f_{\text{RL}}}{m_{\text{C}}} \end{bmatrix}. \tag{A.2.34}$$

Solving the eigenvalue problem gives two eigenvalues:

$$\omega_1^2 = \frac{f_{\text{RR}} + f_{\text{RL}}}{m_{\text{O}}}, \quad \omega_3^2 = (f_{\text{RR}} - f_{\text{RL}})\left(\frac{1}{m_{\text{O}}} + \frac{2}{m_{\text{C}}}\right). \tag{A.2.35}$$

By fixing the eigenvectors for the normal modes for $G_{\text{bond}}F_{\text{bond}}$ as

$$\boldsymbol{A}_1 = \begin{bmatrix} 1 \\ 1 \end{bmatrix}, \quad \boldsymbol{A}_3 = \begin{bmatrix} 1 \\ -1 \end{bmatrix}, \tag{A.2.36}$$

Eq. (A.2.23) gives the normalization factors:

$$n_1 = \sqrt{\frac{1}{2m_{\text{O}}}}, \quad n_3 = \sqrt{\frac{1}{2}}\sqrt{\frac{1}{m_{\text{O}}} + \frac{2}{m_{\text{C}}}}. \tag{A.2.37}$$

Thus, the matrix that relates the normal coordinates to the internal coordinates is given by

$$L_{\text{bond}} = \begin{bmatrix} \sqrt{\dfrac{1}{2m_{\text{O}}}} & \sqrt{\dfrac{1}{2}}\sqrt{\dfrac{1}{m_{\text{O}}} + \dfrac{2}{m_{\text{C}}}} \\[4mm] \dfrac{1}{2m_{\text{O}}} & -\sqrt{\dfrac{1}{2}}\sqrt{\dfrac{1}{m_{\text{O}}} + \dfrac{2}{m_{\text{C}}}} \end{bmatrix}, \tag{A.2.38}$$

where the rows and columns are correlated with $\Delta r_{\text{R}}, \Delta r_{\text{L}}$ and vibrational modes 1, 3, respec-

tively. Further, its inverse matrix is given by

$$L_{\text{bond}}^{-1} = \begin{bmatrix} \sqrt{\dfrac{m_\text{O}}{2}} & \sqrt{\dfrac{m_\text{O}}{2}} \\ \sqrt{\dfrac{1}{2}}\sqrt{\dfrac{m_\text{O} m_\text{C}}{2m_\text{O} + m_\text{C}}} & -\sqrt{\dfrac{1}{2}}\sqrt{\dfrac{m_\text{O} m_\text{C}}{2m_\text{O} + m_\text{C}}} \end{bmatrix}. \tag{A.2.39}$$

Next, the same procedure is applied to the bond angle displacement. The matrix that relates the bond angle displacement to $\Delta x_{\text{O}_\text{R}}, \Delta x_\text{C}, \Delta x_{\text{O}_\text{L}}$ is given by

$$\boldsymbol{B}_{\text{angle}} = \begin{bmatrix} -\dfrac{1}{r_e}, & \dfrac{2}{r_e}, & -\dfrac{1}{r_e} \end{bmatrix}. \tag{A.2.40}$$

Here, the 1×1 "matrix"

$$g_{\text{bond}} = \frac{1}{m_\text{O}} \frac{2}{r_e^2} + \frac{1}{m_\text{C}} \frac{4}{r_e^2} \tag{A.2.41}$$

corresponds to Eq. (A.2.10). By giving the force constant with the bond angle displacement f_{bond}, the proper frequency is

$$\omega_2^2 = g_{\text{bond}} f_{\text{bond}} = f_{\text{bond}} \left(\frac{1}{m_\text{O}} \frac{2}{r_e^2} + \frac{1}{m_\text{C}} \frac{4}{r_e^2} \right). \tag{A.2.42}$$

Then, Eq. (A.2.23) gives the factor that transforms the normal coordinate to the bond angle displacement:

$$l_{\text{angle}} = \frac{1}{r_e} \sqrt{\frac{2}{m_\text{O}} + \frac{4}{m_\text{C}}}, \tag{A.2.43}$$

and its inverse is

$$l_{\text{angle}}^{-1} = \frac{r_e}{2} \sqrt{\frac{2m_\text{O} m_\text{C}}{2m_\text{O} + m_\text{C}}}. \tag{A.2.44}$$

Equations (A.2.24), (A.2.39), and (A.2.44) give the normal coordinates of total symmetric vibration, bending vibration, and anti-symmetric vibration of a CO_2 molecule, as shown in Fig.
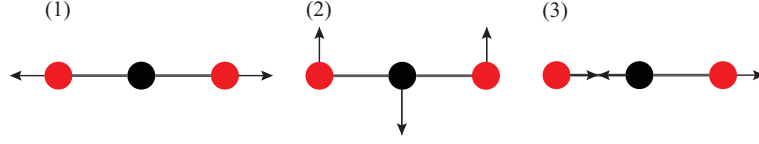
Figure A.2.2: Displacement along the normal coordinates of CO$_2$: (1) total symmetric, (2) bending, and (3) anti-symmetric vibration.

A.2.2. The normal coordinates are generally chosen to be real:

$$Q_1 = \sqrt{m_O} \frac{\Delta r_R + \Delta r_L}{\sqrt{2}}, \quad \omega_1 = \sqrt{\frac{f_{RR} + f_{RL}}{m_O}} \tag{A.2.45}$$

$$Q_2 = \sqrt{\frac{2m_O m_C}{2m_O + m_C}} \frac{r_e}{2} |\Delta\Theta|, \quad \omega_2 = \sqrt{f_{bond}\left(\frac{1}{m_O}\frac{2}{r_e^2} + \frac{1}{m_C}\frac{4}{r_e^2}\right)} \tag{A.2.46}$$

$$Q_3 = \sqrt{\frac{2m_O m_C}{2m_O + m_C}} \frac{\Delta r_R - \Delta r_L}{2}, \quad \omega_3 = \sqrt{(f_{RR} - f_{RL})\left(\frac{1}{m_O} + \frac{2}{m_C}\right)}. \tag{A.2.47}$$

For convenience, the range of the bond angle is defined as $\Theta = [0°, 360°]$ for the derivation of Eq. (A.2.28). In reality, Q_2 is proportional to $|\Delta\Theta|$.

A.2.3 Derivation of bond-angle distribution function

For a linear triatomic molecule such as CO$_2$, the degrees of freedom of translation, rotation and vibration are considered to be three, two, and four, respectively. Then, four degrees of freedom are assigned to the normal vibrational modes: one total symmetric vibration, two degenerate bending vibrations, and one anti-symmetric vibration. The two degenerate bending vibration correspond to the bond angle displacement and rotation about the z-axis [181]; thus, the normal coordinates of Eq. (A.2.46) represent the bond angle deviation. The wave function of Q_2 under the harmonic approximation is given by

$$\chi_0^{(2)}(Q_2) \propto \exp\left(-\frac{\omega_2 Q_2^2}{2}\right), \tag{A.2.48}$$

which is derived in Appendix C. Although the wave function intensity $\left|\chi_0^{(2)}\right|^2$ has its peak at $Q_2 = 0$, i.e., at the linear molecular geometry, the bond-angle population function has its peak at an angle somewhat smaller than 180°. The reason is explained below.

For simplicity, the right C–O bond of a CO$_2$ molecule is fixed to the z-axis and is regarded as the rotational axis (see the inset of Fig. A.2.3). This is possible because the bond-angle distribution function does not depend on rotational axis selection. The C–O bond length of the
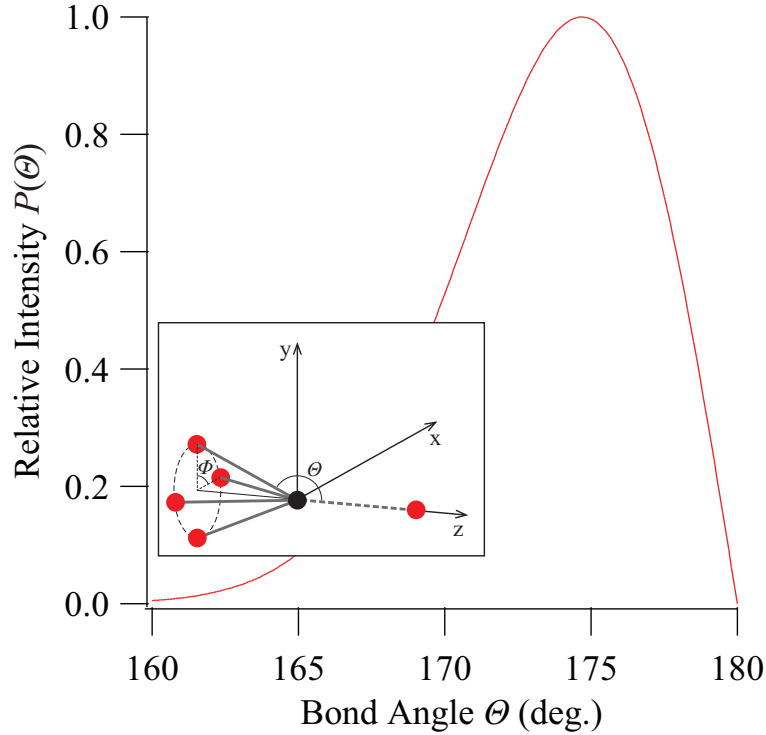
Figure A.2.3: Bond-angle population function of the CO_2 molecule in the vibrational "ground state". Its peak position is not 180°but 174.7°even though the equilibrium structure of CO_2 molecules is linear. The inset shows the definition of the coordinate system. Adapted from Ref. [118].

CO_2 molecule is fixed at $r_e = 1.1600$ Å [182]. Then, the coordinate of the left O atom is given by the polar axis frame of the z-axis and the bond angle. The area element of the left O atom's position is $\sin\Theta d\Theta d\Phi$ and the bond-angle distribution function is given by $\left|\chi_0^{(2)}\right|^2 \sin\Theta d\Theta d\Phi$. By the integral over the azimuthal angle Φ and normalization with respect to the integration over the polar angle Θ, the analytical form of the bond-angle population function results in

$$P(\Theta) = 2\omega_2 \frac{r_e^2}{4} \frac{2m_O m_C}{2m_O + m_C} \exp(-\omega_2 Q_2^2) \sin\Theta. \qquad (A.2.49)$$

The approximation $\sin\Theta \approx |\Delta\Theta|$ holds for the width of $\exp(-\omega_2 Q_2^2)$, and the integral is performed in $[0, \pi]$ for normalization:

$$\int_0^\pi \exp(-\omega_2 Q_2^2)|\Delta\Theta|d|\Delta\Theta|. \qquad (A.2.50)$$

The bond-angle population function $P(\Theta)$ is plotted in Fig. A.2.3. It has a peak at the bond
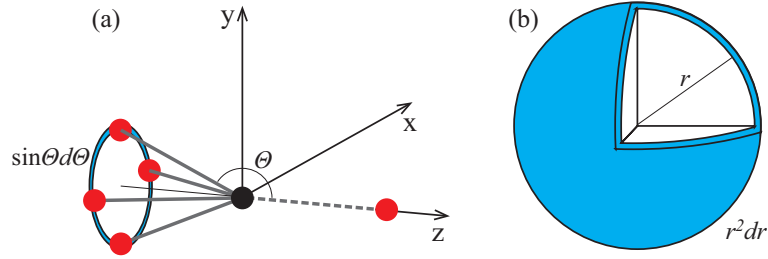
Figure A.2.4: (a) Circular area element for observation of a CO_2 molecule with fixed bond length and (b) spherical volume element for observation of $1s$ electron in a hydrogen atom.

angle of 174.7°and bending molecules rather than linear structures are expected to contribute to RFPAD profiles for C $1s$ photoelectron detection in the recoil frame for CO^+–O^+. The character of the bond-angle population function originates from the circular area element $\sin\Theta d\Theta$ for the left O atom (see Fig. A.2.4). The relation between the wave function of Q_2 and the bond-angle population function is similar to that between the wave function and the radial population function of the $1s$ electron in a hydrogen atom. The wave function of the electron is

$$\Psi_{1s}(\mathbf{r}) = R_{1s}(r)Y_{00}(\Omega) = 2\frac{1}{\sqrt{4\pi}}\exp(-r). \tag{A.2.51}$$

If the position of the electron is observed in Cartesian coordinate, i.e., the volume element is $dxdydz$, the most probable position of the $1s$ electron is the nuclear position. If the distance of the electron from the nuclear position is considered, the volume element is $r^2\sin\Theta d\Theta d\Phi$ and the wave function intensity is integrated over Θ and Φ, thus the volume element becomes r^2dr (see Fig. A.2.4). In this manner, the radial distribution function

$$P_{\text{radial}}(r) = |R_{1s}(r)|^2 r^2 = 4r^2\exp(-2r) \tag{A.2.52}$$

has a peak at the Bohr radius.

The bond-angle population function $P(\Theta)$ is derived for the fixed C–O bond length even though the normal coordinate and the proper frequency (A.2.46) vary with the bond length. Furthermore, the zero-point vibration of the anti-symmetric mode may skew the symmetry of a CO_2 molecule in a snapshot from $D_{\infty h}$ to $C_{\infty v}$. Then, the normal coordinate and the proper

frequency become

$$Q_2 = \sqrt{\frac{m_O m_C (r_R + r_L)^2}{m_O(r_R + r_L)^2 + m_C(r_R^2 + r_L^2)}} \frac{r_R r_L}{r_R + r_L} |\Delta\Theta| \tag{A.2.53}$$

$$\omega_2 = \sqrt{f_{bond}\left[\frac{1}{m_O}\frac{1}{r_R^2} + \frac{1}{m_O}\frac{1}{r_L^2} + \frac{1}{m_C}\left(\frac{1}{r_R} + \frac{1}{r_L}\right)^2\right]}. \tag{A.2.54}$$

Thus the bond-angle population function $P(\Theta)$ depends on the instantaneous structure of the CO_2 molecule. However, there is no visible difference between $P(\Theta)$ of the fixed bond-length molecule and that of the stretching bond-length. Thus, for further discussion, we take only the zero-point bending vibrational motion into consideration.

A.3   RFPAD considering the degenerate bending vibration

In our theoretical model, to account for the target vibrational motions, we obtain the Born-Oppenheimer approximation for the initial state and the final scattering state, and we express them as the products of electronic and vibrational functions: the former is expressed as $\Psi_i(r; Q)\chi_{i,0}(Q)$ and the latter is expressed as $\Psi_f(r^{n-1}; Q)\psi_k^-(r; Q)\chi_{f,v'}(Q)$, where r and Q represent n-electron coordinates and the normal coordinates for the vibrational motions, respectively. The photoelectron is represented by $\psi_k^-(r; Q)$ for the final state. Here, the dipole approximation is employed. It is also assumed that the ionization and Auger decay are described separately (two-step approximation). Then, the RFPAD formula considering the molecular vibration is obtained:

$$I(\hat{k}) = \sum_{v'}\left|\left\langle\Psi_f(r^{n-1}; Q)\psi_k^-(r; Q)\chi_{f,v'}(Q)\middle|\hat{e}\cdot r\middle|\Psi_i(r; Q)\chi_{i,0}(Q)\right\rangle\right|^2. \tag{A.3.1}$$

As the vibrational levels are not resolved in C $1s$ photoelectron measurements for the present study, we can sum over the final vibrational levels of v' to compute the photoemission intensity and can the closure relation

$$\sum_{v'}\chi_{f,v'}(Q)\chi_{f,v'}(Q') = \delta(Q - Q'). \tag{A.3.2}$$

Then, the RFPAD formula reduces to

$$I(\hat{\boldsymbol{k}}) = \int \left| \left\langle \Psi_f(\boldsymbol{r}^{n-1}; \boldsymbol{Q}) \psi_{\boldsymbol{k}}^-(\boldsymbol{r}; \boldsymbol{Q}) \middle| \hat{\boldsymbol{e}} \cdot \boldsymbol{r} \middle| \Psi_i(\boldsymbol{r}; \boldsymbol{Q}) \right\rangle \right|^2 \left| \chi_{i,0}(\boldsymbol{Q}) \right|^2 d\boldsymbol{Q}. \tag{A.3.3}$$

In the molecular ground state, the totally symmetric stretching frequency ω_1, the two-degenerate bending frequency ω_2, and the anti-symmetric stretching frequency ω_3 are 165, 83, and 291 meV, respectively [182]. At room temperature, the bending modes with higher vibration levels than $v = 0$ are populated less than 4%. Therefore, it was assumed that all the modes are in the ground state of $v = 0$ because the temperature in the molecular beam is lower than room temperature. In this context, the RFPAD intensity is the integration of static photoelectron intensities over all molecular structures in the zero-point vibrational ensemble for the initial electronic state.

As stated in Sec. A.2, only the bending vibration is taken into account hereafter. Because the recoil axis along the line from the center of gravity of O–C$^+$ to O$^+$ differs slightly from the direction of the C–O bond that dissociates because of Coulomb explosion, their geometrical relation needs to be examined. Suppose that a CO_2 molecule bears an infinitesimally bent structure with a fixed center of gravity. It is assumed that the fragment ion O–C$^+$ is a rigid body and that both the ions obey the classical momentum conservation law. Then, the recoil axis is at the center of gravity of the parent CO_2 molecule. The equilibrium bond length is $r_e = 1.1600$ Å [182], the geometrical relation shown in Fig. A.3.1, and the relations

$$\Delta x_{\mathrm{C}} = \frac{2m_{\mathrm{O}}}{2m_{\mathrm{O}} + m_{\mathrm{C}}} \frac{r_e}{2} \Delta\Theta \tag{A.3.4}$$

$$\Delta x_{\mathrm{O}} = -\frac{2m_{\mathrm{C}}}{2m_{\mathrm{O}} + m_{\mathrm{C}}} \frac{r_e}{2} \Delta\Theta, \tag{A.3.5}$$

derived from Eq. (A.2.27), give the angle between the recoil axis and the dissociationg C–O bond. The angles are 1.8°and 3.7°when the bond angles are 175°and 170°, respectively. These values are much smaller than the relevant experimental acceptance angles of the recoil ions (in plane, $\pm 10°$; out of plane, $\pm 20°$), hence, we approximate the dissociation bond direction by the recoil axis.

Under these circumstances, the RFPADs for observing CO$^+$ going to the left and O$^+$ going to the right, for the light polarization parallel ($\hat{\boldsymbol{z}} \parallel \hat{\boldsymbol{n}}$) and perpendicular ($\hat{\boldsymbol{x}} \perp \hat{\boldsymbol{n}}$) to the molecular
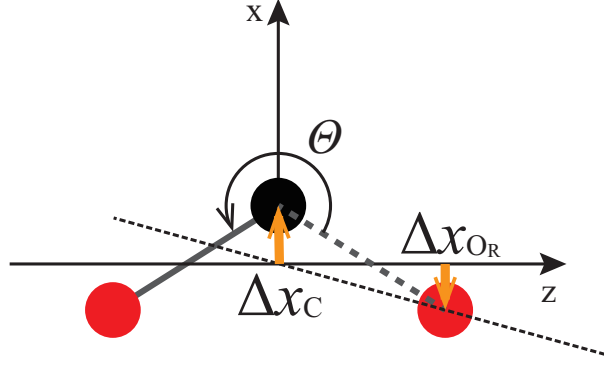
Figure A.3.1: CO_2 molecule bearing infinitesimally bent structure with fixed center of gravity. The broken line at the center of gravity is the recoil axis for the OC^+–O^+ dissociation.

axis $\hat{\boldsymbol{n}}$, are given by

$$I(\hat{\boldsymbol{k}})|_{\hat{\boldsymbol{z}}\|\hat{\boldsymbol{n}}(\hat{\boldsymbol{x}}\perp\hat{\boldsymbol{n}})} \sim \int P(\Theta)d\Theta \left| \left\langle \Psi_f(\boldsymbol{r}^{n-1};\Theta)\psi_{\boldsymbol{k}}^-(\boldsymbol{r};\Theta) \left| z(x) \right| \Psi_i(\boldsymbol{r};\Theta) \right\rangle \right|^2. \qquad (A.3.6)$$

Thus, we arrive at the intuitive result that the observed RFPAD is obtained by integrating the fixed-nuclei RFPAD over the entire internal geometries weighted by the bond-angle population function. The use of the same one-electron molecular basis for the initial and final electronic states reduces the n-electron integral to a one-electron integral in Eq. (A.3.6), which is the case in our calculations. The molecular-geometry-dependent RFPADs for the photoemission from the C atom were calculated by our XPD theory described in Chap. 2 [39,40]. Here, we assumed that within the framework of the two-step approximation the probabilities of the left and right bond dissociations after the Auger decay following the C $1s$ photoemission are the same, because the two O atoms in CO_2^+ with the C $1s^{-1}$ hole are identical in the zero-point bending vibration motion.

The calculation results for parallel and perpendicular RFPADs at photoelectron kinetic energies (KEs) of 85, 120, and 150 eV are shown in Fig. A.3.2. The left-right asymmetry is well reproduced at all the photoelectron energies and for both the parallel geometry (Fig. A.3.2 (a), (c) and (e)) and the perpendicular geometry (Fig. A.3.2 (b), (d) and (f)). The observed asymmetry for the parallel geometry can be interpreted as follows: (i) the bond-angle population function reflects the fact that the contribution of nonlinear structures at the instant of photoemission is much more than that of linear structures (see Fig. A.2.3). (ii) Furthermore, for KEs greater than approximately 100 eV, the photoelectrons from the central C atom are emitted
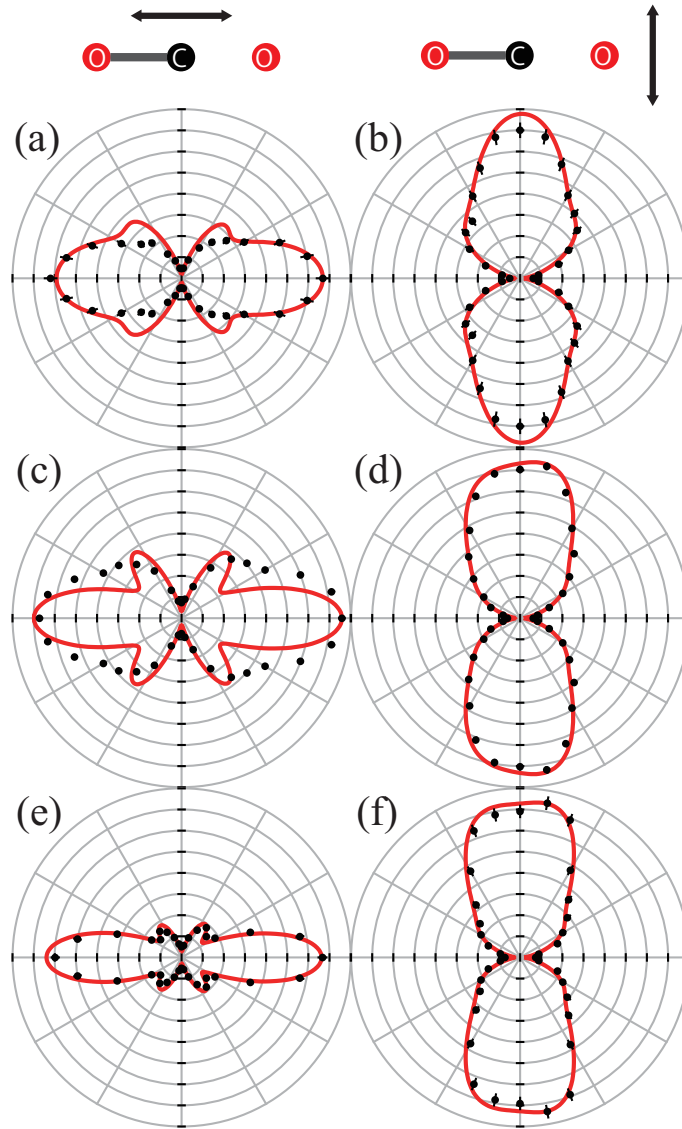
Figure A.3.2: Polar plots of the C $1s$ RFPADs from CO_2 at the photoelectron kinetic energies of 85 eV (a), (b), 120 eV (c), (d), and 150 eV (e), (f). The filled circles with statistical error bars indicate the experimental data. The bold solid curves indicate the theoretical results. The theoretical results are convoluted by the relevant experimental acceptance angles for the electrons and ions (in plane, $\pm10°$; out of plane, $\pm20°$; for both photoelectrons and fragment ions). The experimental results are normalized to the theoretical maximum. The polarization vector of the incident photons and the dissociation directions of the fragment ion pairs of CO^+–O^+ are indicated in the figure. Adapted from Ref. [118].

predominantly toward the O atom of the C–O⁺ fragment, which is slightly tilted from the z-axis, owing to the forward-focusing effect [27]. For the perpendicular geometry, the forward-focusing effect due to the finite-volume O atomic potential has a greater bearing on the broader lobes of the left half than on those of the right half in Fig. A.3.2 (d) and (f), although the effect is not significantly strong.

A.4   Reexamination of previous suggestions

Miyabe *et al.* suggested that the asymmetric RFPADs measured by Liu *et al.* [66] at KE = 14.2 and 23.3 eV can be reasonably explained if the zero-point anti-symmetric stretching vibration is properly treated [176, 177]. To confirm the validity of their model, we examined the influence of the zero-point anti-symmetric vibrational motion using our model. To describe the observation of the asymmetric ion pair of CO⁺–O⁺ in the experiment, we introduced the parameters P_{long} and P_{short}, which satisfy $P_{\text{long}} + P_{\text{short}} = 1$, where P_{long} is the probability of the longer dissociated C–O bond, and P_{short} is that of the shorter C–O bond (details are provided in Appendix B). Thus, the parallel RFPAD for observing CO⁺ going to the left and O⁺ going to the right is given by

$$I(\hat{\boldsymbol{k}})|_{\hat{\boldsymbol{z}}\|\hat{\boldsymbol{n}}} = \int_{-\infty}^{0} P_{\text{short}} \left| \left\langle \Psi_f \psi_{\boldsymbol{k}}^- \middle| z \middle| \Psi_i \right\rangle \right|^2 \left| \chi_0^{(3)}(Q_3) \right|^2 dQ_3$$
$$+ \int_{0}^{\infty} P_{\text{long}} \left| \left\langle \Psi_f \psi_{\boldsymbol{k}}^- \middle| z \middle| \Psi_i \right\rangle \right|^2 \left| \chi_0^{(3)}(Q_3) \right|^2 dQ_3,$$
(A.4.1)

where the positive value of Q_3 corresponds to the structure in which the right C–O bond is longer than the left one, and vice versa (see A.2.47). The calculation results for parallel RFPADs at KE = 85 and 150 eV are shown in Fig. A.4.1. On the one hand, the asymmetric parallel RFPAD at KE = 85 eV is well reproduced when we set $P_{\text{long}} = 0.7$ and $P_{\text{short}} = 0.3$. On the other hand, the RFPAD at KE = 150 eV is explained when we set $P_{\text{long}} = 0$ and $P_{\text{short}} = 1.0$. Further, P_{long} and P_{short} are independent of the incident photon energy within the two-step model. Thus, this inconsistency of the P_{long} and P_{short} values implies that the issue of the left-right asymmetry of CO_2 C $1s$ RFPAD is not due to the zero-point anti-symmetric vibration.

Sturm *et al.* measured the parallel RFPADs at KE = 24.3 eV and found that their asymmetry depends on the kinetic energy release (KER) of the fragment ion pair of CO⁺–O⁺ [67]. In their measurement, the recoil-ion acceptance angle was constant at 21°despite different KERs. Thus,

it is obvious that the effective acceptance angle of the ions in the momentum space changes according to KER. The zero-point bending vibrational effect on the left-right asymmetry is influenced by the acceptance angle of the recoil ions; hence, the KER-dependent asymmetry may not be due to the zero-point anti-symmetric vibration but due to the bending vibrational effect.
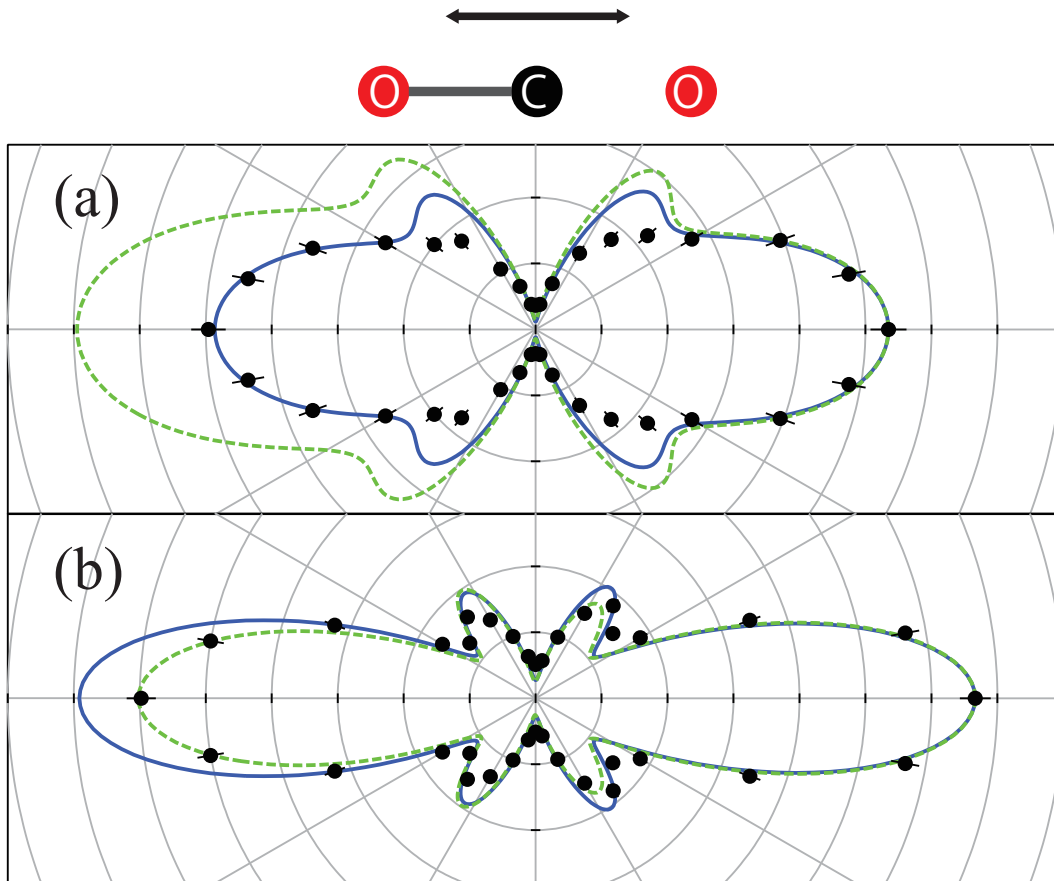
Figure A.4.1: Polar plots of the C $1s$ RFPADs from CO_2 considering the zero-point anti-symmetric stretching motions at the photoelectron energy of 85 eV (a) and 150 eV (b). The filled circles with statistical error bars represent the same experimental data as that in Figure A.3.2 (a) and (c). The solid and dashed lines are the theoretical results for $P_{long} = 0.7$ and $P_{short} = 0.3$ and for $P_{long} = 0$ and $P_{short} = 1.0$, respectively (see text). The theoretical results are convoluted by the relevant experimental acceptance angles for the electrons and ions (in plane, $\pm 10°$; out of plane, $\pm 20°$; for both photoelectrons and fragment ions). The experimental results are normalized to the theoretical maximum. The polarization vector of the incident photons and the dissociation directions of the fragment ion pairs of CO^+–O^+ are indicated in the figure. Adapted from Ref. [118].

A.5   Summary

We calculated C $1s$ PADs detected in coincidence with the fragment ion pairs of CO^+–O^+ of CO_2 molecules by considering the zero-point vibrations to explain the observed left-right asymmetry. Our calculations revealed that the issue of asymmetry is not due to the zero-point anti-symmetric vibration and concomitant selective C–O bond dissociation but due to both the two degenerate zero-point bending vibrations and the CO^+–O^+ two-body fragmentation detection. Thus, C $1s$ PADs detected in coincidence with the fragment ion pairs of CO^+–O^+ of CO_2 molecules should be considered as RFPADs, although they have long been considered as MFPADs.

Appendix B

O $1s$ PAD in recoil frame for CO$^+$–O$^+$
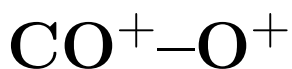
B.1   Introduction

In conventional angle-resolved photoelectron spectroscopy of gaseous molecules, detailed information on photoionization dynamics is washed out by the freely rotating molecules. A breakthrough in this field was achieved in mid-1990s by the application of angle-resolved electron-ion coincidence techniques, which allow the selection of molecules with a well-defined spatial orientation from an ensemble of randomly oriented molecules [48–50]. Photoelectron angular distributions measured by such coincidence techniques are called recoil frame photoelectron angular distributions (RFPADs). In an axial recoil dissociation process, the two fragment ions fly off exactly anti-parallel to one another. If the dissociation is initiated by the ejection of a photoelectron from a core orbital, which is followed by the Auger decay, and also from a valence orbital, then the photoelectron is tied to the direction of the molecular axis at the moment of photoionization. Assuming that this entire process takes place on a timescale that is shorter than a rotational period, the measurement of the RFPAD is equivalent to the molecular frame PAD (MFPAD) referenced in the direction of the breaking bond. Nowadays, MFPAD measurements are growing in importance owing to their sensitivity to photoionization dynamics [51–53, 183].

In this scenario, the fragment ion pair detection has two roles: one is to record the LF direction of the molecular axis, and the other is to select a specific dissociation channel after the Auger decay. The former is necessarily used in the RFPAD/MFPAD measurements. How-

ever, the latter has not been intensively considered thus far, although several studies have been conducted [64, 66, 67, 72, 176, 177, 185–187]. In this context, we manage the latter as well as the former to usher in a new era of RFPADs, by considering the site-specific fragmentation. A simple illustration of the dissociation channel selected RFPADs of CO_2 molecules is given in Fig. B.2.1. At the instant of photoionization ($t = 0$), the O $1s$ photoelectron is ejected from either the left or right the O atom as a result of the dynamical symmetry breaking because of vibronic coupling and concomitant core-hole localization [188, 189]. The Auger decay ($t > 0$) can generally leave the CO_2^{2+} ions in any number of dissociative electronic states. Then, if one focuses on the two-body fragmentation of CO_2^{2+}, the ensemble of the core-ionized molecules splits into two sub-ensembles: one is the right bond breaking (*Channel 1* and *Channel 2*) and the other is the left bond breaking (*Channel 3* and *Channel 4*). Thus, it is evident that the RFPAD obtained by the CO$^+$–O$^+$ fragment ion pair is the incoherent superposition of the RFPAD initiated by the electron ejection from the right O (*Channel 1*) and that from the left O (*Channel 2*). The purpose of the present work is to account for the left-right asymmetric RFPADs from the CO$^+$–O$^+$ fragment ion pair and to determine the factor responsible for the site-specific fragmentation, which will be defined later. To the best of our knowledge, such a factor has not been determined by Auger-electron–fragment ion coincidence studies thus far, e.g., [190, 191].

In this Appendix, we report the experimental results on O $1s$ RFPADs for the CO$^+$–O$^+$ fragment ion pair, which were obtained by Adachi *et al.* by using the undulator beam line BL-2C of the Photon Factory multi-coincidence velocity-map imaging spectrometer [73, 74]. These measurements were carried out at the photoelectron energies of 90, 120, and 150 eV to avoid the broad shape resonance peak centered at $\sim$20 eV [175]. To account for our left-right asymmetric RFPADs for CO$^+$–O$^+$, we propose a simple model based on the MS-XPD theory [39, 40]. Photoelectron scattering within a molecule in the high-energy off-resonance region is well described by the proposed model [75–78].

B.2 Introducing a semi-empirical model

To account for the target vibrational motion, we obtain the Born-Oppenheimer approximation for the initial state and the final scattering state, and we express them as the products of electronic and vibrational functions: the former is expressed as $\Psi_i(\boldsymbol{r}; \boldsymbol{Q})\chi_{i,0}(\boldsymbol{Q})$ and the latter is expressed as $\Psi_f^{\mathrm{R(L)}}(\boldsymbol{r}^{n-1}; \boldsymbol{Q})\psi_{\boldsymbol{k}}^-(\boldsymbol{r}; \boldsymbol{Q})\chi_{f,v'}(\boldsymbol{Q})$, where $\boldsymbol{Q}$ is the normal coordinate and the

superscript R(L) stands for the $(1s)^{-1}$ hole site localized on the right(left) O atom of CO_2. As individual vibrational levels are not resolved in our O $1s$ photoelectron measurements, we can sum over the final vibrational levels of v' to compute the photoemission intensity and use the closure relation Eq. (A.3.2).

In the molecular ground state, the asymmetric stretching frequency is 291 meV [182]. Hence, it was assumed that the stretching mode is in the ground vibrational state of $v = 0$ because the temperature in the molecular beam is lower than room temperature. Furthermore, to describe the observation of the asymmetric ion pair of CO^+–O^+ in the experiment, we introduced the partial Auger decay width $\Gamma_{R(L)\to R}(\boldsymbol{Q})$, leading to the right C–O bond scission of CO_2^+ having the $(1s)^{-1}$ hole on the right(left) O atom. The equilibrium structures for the two diabatic states for the right and left O $(1s)^{-1}$ hole occur at $\pm Q_{3,\mathrm{eq}}$ (see Fig. B.2.1). Note that in the equilibrium structures for the diabatic states, the bond between the C atom and the O atom with the O $(1s)^{-1}$ hole is longer than the other CO bond [192]. Keeping the time scale—[the Auger decay period ($\sim$4 fs [188]) is shorter than the vibrational period ($\sim$13.5 fs [188]) of the anti-symmetric stretching mode]—in mind and from Fig. B.2.1, one can discuss the O 1s RFPAD in coincidence with the asymmetric ion pair of CO^+–O^+ from a time-dependent point of view. The vibrational wave packet of CO_2^+, formed at the instant of the O $1s$ photoionization, starts to move in the $+Q_{3,\mathrm{eq}}$ direction in the diabatic potential or in the $-Q_{3,\mathrm{eq}}$ direction; then, during its motion, the Auger decay leads to the destruction of the initially localized wave packet. For the wave packets moving in the $\pm Q_{3,\mathrm{eq}}$ directions, two different right-bond dissociation channels are possible: one is the longer C–O bond dissociation $\Gamma_{R\to R}(\boldsymbol{Q})$, *Channel 1* and the other is the shorter C–O bond dissociation $\Gamma_{L\to R}(\boldsymbol{Q})$, *Channel 2*.

Under these circumstances and the two-step approximation, the RFPAD for observing O^+ going to the right and CO^+ going to the left, for light polarization parallel to the recoil axis, is given by the incoherent superposition of the RFPAD for *Channel 1* and that for *Channel 2* in Fig. B.2.1:

$$I^{R}(\hat{\boldsymbol{k}})|_{\hat{\boldsymbol{z}}\|\hat{\boldsymbol{n}}} \sim \int \Gamma_{R\to R}(\boldsymbol{Q})\left|\left\langle\Psi_f^R\psi_{\boldsymbol{k}}^-\left|z\right|\Psi_i\right\rangle\right|^2\left|\chi_{i,0}(\boldsymbol{Q})\right|^2 d\boldsymbol{Q}$$
$$+ \int \Gamma_{L\to R}(\boldsymbol{Q})\left|\left\langle\Psi_f^L\psi_{\boldsymbol{k}}^-\left|z\right|\Psi_i\right\rangle\right|^2\left|\chi_{i,0}(\boldsymbol{Q})\right|^2 d\boldsymbol{Q}. \tag{B.2.1}$$

The use of the same one-electron molecular basis for the initial and final electronic states
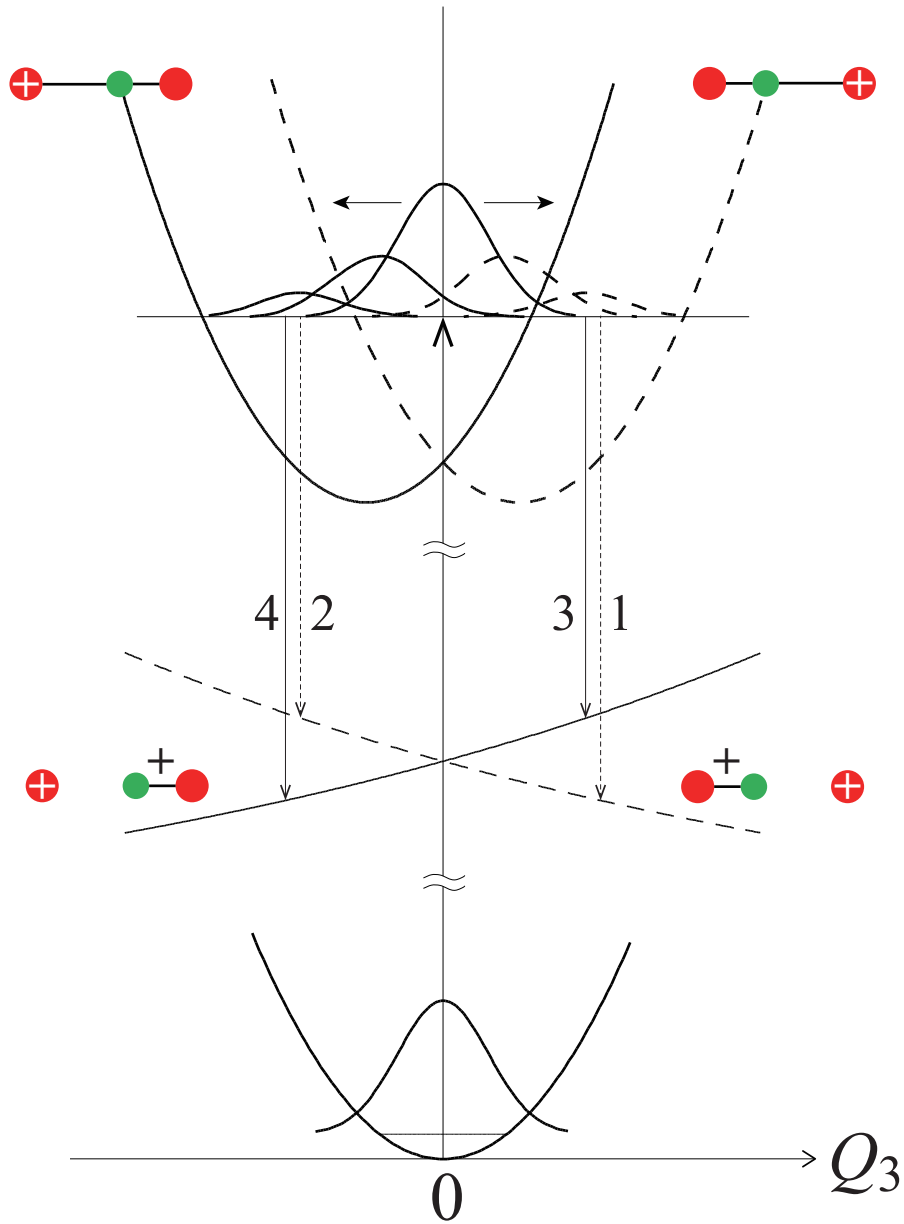
Figure B.2.1: Vibrational potential energy curves of CO_2, CO_2^{+*} and CO_2^{2+} in the direction of the anti-symmetric vibration Q_3. The diabatic potential of CO_2^{+*} and vibrational wave packets for CO_2^{+*} are constructed using the experimental results of Ref. [188]. The vibrational wave packets are destroyed by the Auger decay of 1&3 and 2&4 during their motion. Adapted from Ref. [119].

reduces the n-electron integral to a one-electron integral in Eq. (B.2.1), which is the case in our calculations. Here we approximate the initial vibrational wave function $\chi_{i,0}$ as a harmonic-oscillator function using the force constant of Ref. [182]. The molecular geometry ($\boldsymbol{Q}$) dependent RFPADs for the photoemission from the left O and right O atoms were calculated by the MS-XPD theory described in Chap. 2 [39,40]. It is noteworthy that we could not find any significant difference between the RFPADs obtained by integrating the dipole matrix elements over the entire internal geometry of the vibrational ground state, with each geometry weighted by the square of $\chi_{i,0}$, and those obtained by fixed-nuclei calculations at the equilibrium geometry (see Appendix B.5). Moreover, the ratio of the integral of the partial Auger decay width $\Gamma(\boldsymbol{Q})$ over the molecular geometry ($\boldsymbol{Q}$), i.e., the bond breaking probability of the C–O without the O $(1s)^{-1}$ hole relative to that of the C–O with the O $(1s)^{-1}$ hole in Eq. (B.2.1), is treated as a free parameter: $\frac{\int \Gamma_{\mathrm{L}\to\mathrm{R}}(\boldsymbol{Q})d\boldsymbol{Q}}{\int \Gamma_{\mathrm{R}\to\mathrm{R}}(\boldsymbol{Q})d\boldsymbol{Q}} = R_{\mathrm{R}\to\mathrm{R}}^{\mathrm{L}\to\mathrm{R}}$. Then, Eq. (B.2.1) is recast as

$$I^{\mathrm{R}}(\hat{\boldsymbol{k}})|_{\hat{\boldsymbol{z}}\|\hat{\boldsymbol{n}}} \sim \left|\langle\psi_{\boldsymbol{k}}^-|z|\psi_{1s}^{\mathrm{R}}\rangle_{\boldsymbol{Q}=0}\right|^2 + R_{\mathrm{R}\to\mathrm{R}}^{\mathrm{L}\to\mathrm{R}}\left|\langle\psi_{\boldsymbol{k}}^-|z|\psi_{1s}^{\mathrm{L}}\rangle_{\boldsymbol{Q}=0}\right|^2. \tag{B.2.2}$$

B.3 RFPAD calculations dependent on the parameter

The RFPADs for the photoemission from the left O and right O atoms are mirror-symmetric with respect to a plane containing the central C atom; hence, their sum results in the left-right symmetric RFPAD, if the ratio of the decay probabilities $R_{\mathrm{R}\to\mathrm{R}}^{\mathrm{L}\to\mathrm{R}}$ is unity. This implies that the left-right asymmetry of the RFPAD observed in coincidence with the asymmetric fragment ion pair of CO^+–O^+ is the result of $R_{\mathrm{R}\to\mathrm{R}}^{\mathrm{L}\to\mathrm{R}} \neq 1$. In fact, the best results shown in Fig. B.3.1 were obtained as $R_{\mathrm{R}\to\mathrm{R}}^{\mathrm{L}\to\mathrm{R}} = 0.70$.

Thus, we arrive at the following intuitive interpretation. The photoelectron will have left the vicinity of the molecule within a fraction of a femtosecond; thus, the molecular structure sampled by the photoelectron is the initial-state equilibrium geometry. Then, the dissociation, which is controlled by the partial Auger decay probability, occurs at $Q_3 \neq 0$ for $t > 0$ in the diabatic potential. This effect is incorporated in the free parameter that describes the decay probability. From the nearly complete agreement between experiment and theory, we conclude that site-specific fragmentation, which is characterized by the parameter $R_{\mathrm{R}\to\mathrm{R}}^{\mathrm{L}\to\mathrm{R}}$, plays an essential role in the observed left-right asymmetric RFPADs.

To examine the effect of the site-specific fragmentation on the RFPADs in greater detail,
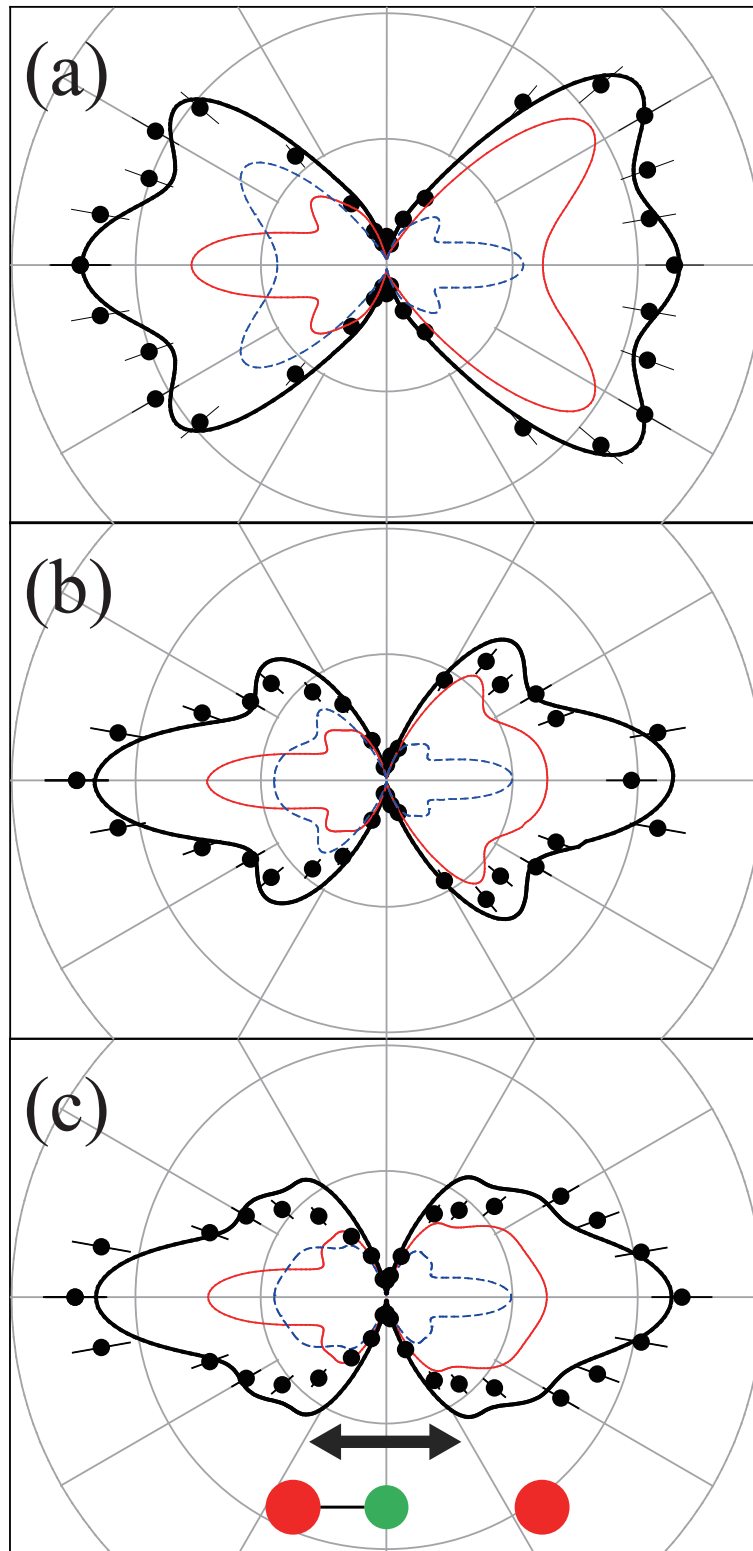
Figure B.3.1: Polar plots of the O $1s$ RFPADs from CO_2 at the photoelectron energies of 90 (a), 120 (b), and 150 eV (c). The filled circles with error bars represent the experimental data. The bold solid curves represent the theoretical results, which have been constructed by incoherent superposition of the RFPAD (thin solid curve) for photoemission from the right O atom and that (thin broken curve) for photoemission from the left O atom. The latter is multiplied by 0.70. The theoretical results are convoluted by the relevant experimental acceptance angles for the electrons and ions (in plane, $\pm 5°$, and out of plane, $\pm 20°$, for photoelectrons; in plane, $\pm 10°$, and out of plane, $\pm 20°$, for fragment ions). The polarization vector of the incident X-ray and the dissociation directions of the fragment ion pairs of CO^+–O^+ are indicated in the figure. Adapted from Ref. [119].
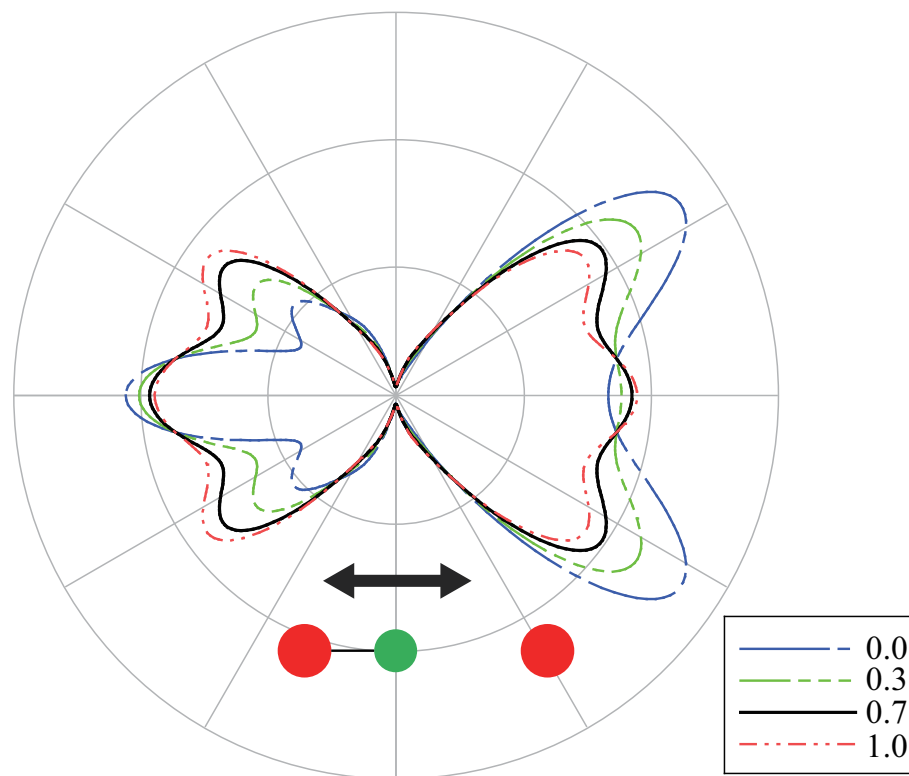
Figure B.3.2: Dependence of the O $1s$ RFPADs from CO_2, at the photoelectron energy of 90 eV, on the ratio of the partial Auger decay width. The numbers in the legend are the ratios of $R_{R \to R}^{L \to R}$ (see text). The polarization vector of the incident X-ray and the dissociation directions of the fragment ion pairs of CO^+–O^+ are indicated in the figure. Adapted from Ref. [119].

we calculated them by changing the values of $R_{R \to R}^{L \to R}$ (see Fig. B.3.2). As can be understood from Eq. (B.2.2), at $R_{R \to R}^{L \to R} = 0$ the photoelectron is emitted exclusively from the right O atom; hence, the RFPAD exhibits the strongest left-right asymmetric profile. In the other extreme case of $R_{R \to R}^{L \to R} = 1$, the photoelectrons emitted from the left and right atoms contribute equally to the RFPAD; then, it becomes the symmetric profile. At $R_{R \to R}^{L \to R} = 0.70$, the experimental RFPADs were extremely well reproduced by our model. Owing to the theory based on the lifetime-vibrational interference, the most probable relevant ratio is 0.33 [185]. This value is simply obtained from the partial Auger decay width of 27.726 meV, leading to the direct fragmentation states of CO_2^{2+} and that of 26.732 meV, which in turn lead to the pre-dissociation states of CO_2^{2+}, under the assumption that in the former case, the longer O–C bond dissociates with 100% probability, and in the latter case, the two O–C bonds dissociate with equal probability. The difference between 0.70 of the present result and 0.33 of Ref. [185] is not surprising, because the two approaches are totally different. In Ref. [185], $R_{R \to R}^{L \to R}$ was calculated under some restricted conditions: (i) not all the Auger final states were taken into account; (ii) a highly simplistic dissociation mechanism for the Auger final states was assumed without calculations of the potential energy surfaces of CO_2^{2+}; and (iii) the partial Auger decay widths were assumed to be independent of the molecular geometry expressed by $\boldsymbol{Q}$. By contrast, in the present work, $R_{R \to R}^{L \to R}$ has been parameterized as shown in Eq. (B.2.2), which has been determined from the experimental data. Assuming that the RFPADs for the photoemission from the O atom by our XPD theory are correct, the uncertainty of our $R_{R \to R}^{L \to R}$ value is estimated to be less than ±0.20. It should be noted that the experimental left-right asymmetric RFPADs were approximately reproduced by the theoretical ones [185] in the shape resonance region, although there are some noticeable differences between theory and experiment. The discrepancy may be due to the inaccurate resonance mechanism itself for polyatomic molecules, e.g., [65, 68, 71].

B.4   Summary

The observed left-right asymmetric O 1s RFPADs were reproduced nearly completely by our semi-empirical model based on the MS-XPD theory. From the excellent agreement between the experimental RFPADs and those from theoretical calculations, we have derived the ratio of $R_{R \to R}^{L \to R} = 0.70$, i.e., the site-specific fragmentation probability: The bond breaking probability of the C–O without the O $(1s)^{-1}$ hole is 70% of that of the C–O with the O $(1s)^{-1}$ hole. Because all

previous studies of site-specific fragmentation after inner-shell excitation/ionization have been limited to qualitative discussions, for example [184], the present quantitative result on the site-specific fragmentation is of great significance, and it is a breakthrough in the important area of physical and chemical studies of unique bond cleavage.

B.5 Appendix: Dipole matrix element as a function of normal coordinates

There is no visible difference between the RFPADs integrated over the molecular geometry and those at a fixed geometry. This is because the variances of the zero-point vibration are sufficiently small compared to the de Broglie wavelength of the photoelectron. As derived in Appendix A, the normal coordinates of the total-symmetric vibration Q_1 and the anti-symmetric vibration Q_3 are represented by normal coordinates having dimensions of

$$Q_1 = \sqrt{\mu_1} X_1$$

$$\mu_1 = m_O \tag{B.5.1}$$

$$X_1 = \frac{\Delta z_{O_R} - \Delta z_{O_L}}{\sqrt{2}} = \frac{\Delta r_R + \Delta r_L}{\sqrt{2}} \tag{B.5.2}$$

$$Q_3 = \sqrt{\mu_3} X_3$$

$$\mu_3 = \frac{2 m_O m_C}{2 m_O + m_C} \tag{B.5.3}$$

$$X_3 = \frac{\Delta z_{O_R} - 2\Delta z_C + \Delta z_{O_L}}{2} = \frac{\Delta r_R - \Delta r_L}{2}, \tag{B.5.4}$$

$$\tag{B.5.5}$$

and the wave functions of the vibrational ground states are given by

$$\chi_0^{(1)}(X_1) = \left(\frac{\omega_1}{\pi}\right)^{1/4} \exp\left(-\frac{\mu_1 \omega_1 X_1^2}{2}\right) \tag{B.5.6}$$

$$\chi_0^{(3)}(X_3) = \left(\frac{\omega_3}{\pi}\right)^{1/4} \exp\left(-\frac{\mu_3 \omega_3 X_3^2}{2}\right). \tag{B.5.7}$$

The displacement of the bond length is related to the normal coordinates as

$$\Delta r_R = \frac{1}{\sqrt{2}} X_1 + X_3. \tag{B.5.8}$$

Then, its variance is

$$\langle(\Delta r_{\mathrm{R}})^2\rangle = \left\langle \left(\frac{1}{\sqrt{2}}X_1 + X_3\right)^2 \right\rangle$$

$$= \frac{1}{2}\langle X_1^2\rangle + \langle X_3^2\rangle = \frac{1}{4\mu_1\omega_1} + \frac{1}{2\mu_3\omega_3}. \tag{B.5.9}$$

The variance of the C–O bond length of a CO_2 molecule in the vibrational ground states is 0.03489 Å, which is of the order of 10^{-2} compared to the de Broglie wavelength of 1.29, 1.12 and 1.00 Åfor photoelectrons of KE = 90, 120, and 150 eV. Thus, the dipole matrix element does not depend on the molecular geometry for the symmetric zero-point vibrational ensemble.

Appendix C

Bending vibration of linear triatomic molecules

In this Appendix, the quantization procedure of the degenerate bending vibration of triatomic molecules, such as CO_2, and the derivations of the energy eigenvalues and eigenfunctions are reviewed. Although the two degrees of freedom actually represent the bond-angle deviation and rotation, quantization is achieved by replacing the position coordinates and their conjugate momenta with quantum-mechanical operators of the classical Hamiltonian in Cartesian coordinates. Thus, the normal coordinates should be represented by Q_{2x}, Q_{2y}, which coincide with displacements in the x and y directions, respectively. The coordinates

$$Q_2 = \sqrt{\frac{2m_O m_C}{2m_O + m_C}} \frac{r_e}{2} |\Delta\Theta| \tag{C.1}$$

$$\Delta\Theta = \frac{1}{r_e}(-\Delta\rho_{O_R} + 2\Delta\rho_C - \Delta\rho_{O_L}) \tag{C.2}$$

$$\omega_2 = \sqrt{f_{bond}\Big(\frac{1}{m_O}\frac{2}{r_e^2} + \frac{1}{m_C}\frac{4}{r_e^2}\Big)} \tag{C.3}$$

derived in Appendix A are related to Q_{2x}, Q_{2y} as

$$Q_{2x} = Q_2 \cos\alpha$$

$$Q_{2y} = Q_2 \sin\alpha, \tag{C.4}$$

where α is the azimuthal angle of the rotation about the z-axis. Here $\Delta\rho_{O_R}, \Delta\rho_C, \Delta\rho_{O_L}$ are the amplitudes of the atomic deviation in the periodic bending vibration without mass-center

displacement nor rotation. Their projections to the x- and y-axis are given by

$$\Delta x = \Delta\rho\cos\alpha,$$

$$\Delta y = \Delta\rho\sin\alpha. \tag{C.5}$$

Equations (C.4) and (C.5) give

$$Q_{2x} = \sqrt{\frac{2m_\mathrm{O}m_\mathrm{C}}{2m_\mathrm{O}+m_\mathrm{C}}}\frac{1}{2}(-\Delta x_{\mathrm{O_L}} + 2\Delta x_\mathrm{C} - \Delta x_{\mathrm{O_R}}), \tag{C.6}$$

$$Q_{2y} = \sqrt{\frac{2m_\mathrm{O}m_\mathrm{C}}{2m_\mathrm{O}+m_\mathrm{C}}}\frac{1}{2}(-\Delta y_{\mathrm{O_L}} + 2\Delta y_\mathrm{C} - \Delta y_{\mathrm{O_R}}). \tag{C.7}$$

Further,

$$Q_{2x}^2 = \frac{2m_\mathrm{O}m_\mathrm{C}}{2m_\mathrm{O}+m_\mathrm{C}}\frac{1}{4}[(\Delta x_{\mathrm{O_L}})^2 + 4(\Delta x_\mathrm{C})^2 - (\Delta x_{\mathrm{O_R}})^2], \tag{C.8}$$

$$Q_{2y}^2 = \frac{2m_\mathrm{O}m_\mathrm{C}}{2m_\mathrm{O}+m_\mathrm{C}}\frac{1}{4}[(\Delta y_{\mathrm{O_L}})^2 + 4(\Delta y_\mathrm{C})^2 - (\Delta y_{\mathrm{O_R}})^2] \tag{C.9}$$

must hold to satisfy $Q_2 = \sqrt{Q_{2x}^2 + Q_{2y}^2}$. Thus, the restrictions

$$\Delta x_{\mathrm{O_L}} = \Delta x_{\mathrm{O_R}} = 4\Delta x_\mathrm{C}, \tag{C.10}$$

$$\Delta y_{\mathrm{O_L}} = \Delta y_{\mathrm{O_R}} = 4\Delta y_\mathrm{C} \tag{C.11}$$

are imposed on the atomic displacement amplitudes. Under these restrictions, the classical Hamiltonian of the degenerate bending vibration in Cartesian coordinates is obtained:

$$H_2 = \frac{P_{Q_{2x}}^2}{2} + \frac{P_{Q_{2y}}^2}{2} + \frac{\omega_2^2 Q_{2x}^2}{2} + \frac{\omega_2^2 Q_{2y}^2}{2}. \tag{C.12}$$

where $P_{Q_{2x}}, P_{Q_{2y}}$ are the conjugate momenta of Q_{2x}, Q_{2y}. Quantization is accomplished by replacing

$$P_{Q_{2x}} \to -i\frac{\partial}{\partial Q_{2x}}, \quad P_{Q_{2y}} \to -i\frac{\partial}{\partial Q_{2y}} \tag{C.13}$$

for Eq. (C.12). The fundamental commutation relations

$$[Q_{2x}, P_{2y}] = [Q_{2y}, P_{2x}] = 0, \tag{C.14}$$

$$[Q_{2x}, P_{2x}] = [Q_{2y}, P_{2y}] = i \tag{C.15}$$

hold. The Hamiltonian is transformed as

$$H_2 = \frac{1}{2}\left[-\left(\frac{\partial^2}{\partial Q_2^2} + \frac{1}{Q_2}\frac{\partial}{\partial Q_2} + \frac{1}{Q_2^2}\frac{\partial^2}{\partial\alpha^2}\right) + \omega_2^2 Q_2^2\right] \tag{C.16}$$

by using the differential chain rule for Eq. (C.4). An analytical method [159] and an algebraic [181, 193] method are available to obtain the energy eigenvalues and the corresponding wave functions in the coordinates of Q_2, α. Here, the algebraic method is introduced.

The Hamiltonian H_2 commutes with the vibrational angular momentum operator

$$M = Q_{2x}P_{2x} - Q_{2y}P_{2y} = -i\frac{\partial}{\partial\alpha}. \tag{C.17}$$

Thus, the wave functions are simultaneous eigenfunctions of H_2 and M, and they are of the form

$$\Psi_{v,l} = F_{v,l}(Q_2)e^{il\alpha}. \tag{C.18}$$

By introducing new operators

$$Q^{\pm} = Q_{2x} \pm iQ_{2y}, \tag{C.19}$$

$$P^{\pm} = P_{2x} \pm iP_{2y}, \tag{C.20}$$

multiplication relations

$$P^+P^- = P_{2x}^2 + P_{2y}^2, \tag{C.21}$$

$$Q^+Q^- = Q_{2x}^2 + Q_{2y}^2 \tag{C.22}$$

are derived, and the Hamiltonian is transformed as

$$H_2 = \frac{1}{2}(P^+P^- + \omega_2^2 Q^+Q^-). \tag{C.23}$$

Here, four types of ladder operators are defined:

$$R^{\pm(\pm)} = P^{(\pm)} \pm i\omega_2 Q^{(\pm)}, \tag{C.24}$$

where the signs $\pm$ are correlated with one another. The commutators of $Q^{\pm}$ and $P^{\pm}$ are derived as

$$[Q^+, Q^+] = [Q^+, Q^-] = [Q^-, Q^-] = 0, \tag{C.25}$$

$$[P^+, P^+] = [P^+, P^-] = [P^-, P^-] = 0, \tag{C.26}$$

$$[P^+, Q^+] = [P^-, Q^-] = 0, \tag{C.27}$$

and

$$[P^+, Q^-] = [P^-, Q^+] = -2i, \tag{C.28}$$

and the commutation relations between H_2 and the ladder operators $R^{\pm(\pm)}$ are given by

$$[H_2, R^{\pm(\pm)}] = \omega_2 R^{\pm(\pm)}. \tag{C.29}$$

The commutation relations between the vibrational angular momentum operator M and the ladder operators $R^{\pm(\pm)}$ are given by

$$[M, R^{\pm(\pm)}] = (\pm)R^{\pm(\pm)}. \tag{C.30}$$

The signs $(\pm)$ on the right-hand side of Eq. (C.30) coincide with $(\pm)$ of the ladder operators.

The commutators of Eq. (C.29) are applied to one of the simultaneous eigenfunctions of H_2 and M as

$$\begin{aligned}
[H_2, R^{\pm(\pm)}]\Psi_{v,l} &= \pm\omega_2 R^{\pm(\pm)}\Psi_{v,l} \\
&= H_2 R^{\pm(\pm)}\Psi_{v,l} - E_v R^{\pm(\pm)}\Psi_{v,l}.
\end{aligned} \tag{C.31}$$

Thus, the wave functions multiplied by the ladder operator are also eigenfunctions of the Hamiltonian

$$H_2 R^{\pm(\pm)}\Psi_{v,l} = (E_v \pm \omega_2)R^{\pm(\pm)}\Psi_{v,l}. \tag{C.32}$$

Similarly, the commutators of Eq. (C.30) are applied to the wave functions as

$$
\begin{aligned}
[M, R^{\pm(\pm)}]\Psi_{v,l} &= (\pm)R^{\pm(\pm)}\Psi_{v,l} \\
&= MR^{\pm(\pm)}\Psi_{v,l} - lR^{\pm(\pm)}\Psi_{v,l},
\end{aligned}
\tag{C.33}
$$

Thus, $R^{\pm(\pm)}\Psi_{v,l}$ are also eigenfunctions of the vibrational angular momentum operator:

$$
MR^{\pm(\pm)}\Psi_{v,l} = [l(\pm)1]R^{\pm(\pm)}\Psi_{v,l}.
\tag{C.34}
$$

The ladder operators $R^{\pm(\pm)}$ change the energy eigenvalues as follows:

Table C.1: Creation and annihilation by the ladder operators $R^{\pm(\pm)}$

	energy eigenvalue	l
$R^{+(+)}$	ω_2 increase	increase by 1
$R^{+(-)}$	ω_2 increase	decrease by 1
$R^{-(+)}$	ω_2 decrease	increase by 1
$R^{-(-)}$	ω_2 decrease	decrease by 1

The ladder operators restrict the energy eigenvalues. Multiplications of the ladder operators,

$$
R^{+(+)}R^{-(-)} = 2H_2 + 2\omega_2 M - 2\omega_2,
\tag{C.35}
$$

$$
R^{+(-)}R^{-(+)} = 2H_2 - 2\omega_2 M - 2\omega_2,
\tag{C.36}
$$

lead to a transformation of the Hamiltonian:

$$
H_2 = \frac{1}{4}(R^{+(+)}R^{-(-)} + R^{+(-)}R^{-(+)}) + \omega_2.
\tag{C.37}
$$

Thus, the energy eigenfunctions are simultaneous eigenfunctions of the Hamiltonian and the operator $R^{+(+)}R^{-(-)} + R^{+(-)}R^{-(+)}$. The operator commutes with the vibrational angular momentum operator M and gives eigenvalues as $(R^{+(+)}R^{-(-)} + R^{+(-)}R^{-(+)})\Psi_{s,l} = s\Psi_{s,l}$. The relations $(R^{\pm(\pm)})^{\dagger} = R^{\mp(\mp)}$ restrict the eigenvalue s:

$$
\begin{aligned}
s &= \left\langle \Psi_{s,l} | (R^{+(+)}R^{-(-)} + R^{+(-)}R^{-(+)})\Psi_{s,l} \right\rangle \\
&= \left\langle R^{-(-)}\Psi_{s,l} | R^{-(-)}\Psi_{s,l} \right\rangle + \left\langle R^{-(+)}\Psi_{s,l} | R^{-(+)}\Psi_{s,l} \right\rangle \geq 0.
\end{aligned}
\tag{C.38}
$$

This restriction imposes the lower limit of $s/4 + \omega_2$ on the energy eigenvalue, i.e.,

$$R^{-(\pm)}\Psi_{0,l} = 0, \tag{C.39}$$

where $\Psi_{0,l}$ is the wave function of the ground state. Equations (C.35), (C.36), and (C.39) lead to

$$R^{+(+)}R^{-(-)}\Psi_{0,l} = (2H_2 + 2\omega_2 M - 2\omega_2)\Psi_{0,l} = 0, \tag{C.40}$$

$$R^{+(-)}R^{-(+)}\Psi_{0,l} = (2H_2 - 2\omega_2 M - 2\omega_2)\Psi_{0,l} = 0. \tag{C.41}$$

Addition of Eq. (C.41) and Eq. (C.40) gives

$$H_2\Psi_{0,l} = \omega_2\Psi_{0,l}, \tag{C.42}$$

i.e., the energy eigenvalue for the ground state E_0 is ω_2. Subtraction of Eq. (C.41) from (C.40) gives

$$M\Psi_{0,l} = 0. \tag{C.43}$$

This means that the quantum number of the vibrational angular momentum for the ground state is $l = 0$. Solving the differential equation

$$R^{-(-)}\Psi_{0,0} = 0 \tag{C.44}$$

gives the wave function of the ground state:

$$\Psi_{0,0} \propto \exp\left(-\frac{\omega_2 Q_2^2}{2}\right). \tag{C.45}$$

Iterative application of the ladder operators to the ground state wave function $\Psi_{0,0}$ gives all the energy eigenstates and wave functions. The ladder operator increases or decreases the energy eigenvalue by ω_2:

$$E_v = \omega_2(v + 1), \quad v = 0, 1, 2, \cdots. \tag{C.46}$$

The quantum number v is related to the quantum number s of the operator $R^{+(+)}R^{-(-)} + R^{+(-)}R^{-(+)}$ as $s = 4v\omega_2$. If the operators $R^{+(+)}$ and $R^{+(-)}$ are applied to $\Psi_{0,0}$ n_+ and n_-

times, respectively,

$$n_+ + n_- = v, \tag{C.47}$$

$$n_+ - n_- = l. \tag{C.48}$$

Thus, the wave functions of the excited states are given by

$$\Psi_{v,l} \propto [R^{+(-)}]^{\frac{v-l}{2}} [R^{+(+)}]^{\frac{v+l}{2}} \Psi_{0,0}. \tag{C.49}$$

The quantum number l must be even (odd) when v is even (odd). Further, the inequalities

$$\frac{v-l}{2} \geq 0, \quad \frac{v+l}{2} \geq 0 \tag{C.50}$$

restrict the vibrational angular momentum quantum number as

$$l = v, v-2, \cdots, -v. \tag{C.51}$$

In the classical picture, a linear triatomic molecule does not exhibit the degree of freedom of rotation about the z-axis, but does so when it is bent. The quantization process discussed in this Appendix gives the quantum mechanical picture corresponding to the classical one: value 0 of the vibrational angular momentum M is always observed for the ground state of the bending vibration, but this is not the case for excited states. It should be emphasized that the observed left-right asymmetry of the C $1s$ PAD in the recoil frame for CO^+–O^+ is due to the zero-point vibration of the vibrational ground state and not due to that of the vibrational excitation.

References

[1] H. Hertz, Ann. Physik **267**, 983 (1887).

[2] W. Hallwachs, Ann. Physik **270**, 731 (1888).

[3] J. J. Thomson, Philos. Mag. **44**, 293 (1897).

[4] P. Lenard, Ann. Physik **307**, 359 (1900).

[5] P. Lenard, Ann. Physik **313**, 149 (1902).

[6] A. Einstein, Ann. Physik **322**, 132 (1905).

[7] W. C. Röntgen, Ann. Physik **300**, 12 (1898).

[8] W. H. Bragg, and W. L. Bragg, Proc. R. Soc. A **88**, 428 (1913).

[9] A. Guinier, *X-ray Diffraction: In Crystals, Imperfect Crystals, and Amorphous Bodies* (Feeman, San Francisco, 1963; republished by Dover, New York, 1994).

[10] G. H. Stout, and L. H. Jensen, *X-Ray Structure Determination, a Practical Guide*, 2nd Edition (Wiley, New York, 1989).

[11] G. Rhodes, *Crystallography Made Crystal Clear: A Guide for Users of Macromolecular Models*, 3rd Edition (Academic, Oxford, 2006).

[12] K. Siegbahn, and K. Edvarson, Nuc. Phys. **1**, 137 (1956).

[13] C. Nordling, E. Sokolowski, and K. Siegbahn, Phys. Rev. **105**, 1676 (1957).

[14] K. Siegbahn *et al.*, *ESCA: Atomic, Molecular and Solid State Structure Studied by Means of Electron Spectroscopy* (Almquist and Wiksell, Uppsala, Sweden, 1967).

[15] K. Siegbahn, Phil. Trans. R. Soc. A, **268**, 33 (1970).

[16] D. W. Turner, and M. I. Al Jobory, J. Chem. Phys. **37**, 3007 (1962).

[17] D. W. Turner, A. D. Baker, C. Baker, and C. R. Brundle, *Molecular Photoelectron Spectroscopy* (Wiley, London, 1970).

[18] K. Siegbahn, U. Gelius, H. Siegbahn, and E. Olson, Phys. Lett. A **32**, 221 (1970).

[19] C. S. Fadley, and S. Å. L. Bergström, Phys. Lett. A **35**, 375 (1971).

[20] C. Westphal, Surf. Sci. Rep. **50**, 1 (2003).

[21] E. V. Shalaeva, and M. V. Kuznetsov, J. Struc. Chem. **44**, 465 (2003).

[22] D. P. Woodruff, Surf. Sci. Rep. **62**, 1 (2007).

[23] C. S. Fadley, J. Electron Spectrosc. Relat. Phenom. **178**–**179**, 2 (2010).

[24] M. A. Van Hove, W. H. Weinberg, and C.-M. Chan, *Low-Energy Electron Diffraction: Experiment, Theory and Surface Structure Determination* (Springer-Verlag, Heidelberg, 1986).

[25] C. S. Fadley, Prog. Surf. Sci. **16**, 275 (1984).

[26] C. S. Fadley, Surf. Sci. Rep. **19**, 231 (1993).

[27] C. S. Fadley, in: *Synchrotron Radiation Research: Advances in Surface and Interface Science*, editted by R. Z. Bachrach (Plenum, New York, 1992; republished by Springer, Berlin, 2013).

[28] J. J. Barton, and D. A. Shirley, Phys. Rev. B **32**, 1892 (1985).

[29] J. J. Barton, and D. A. Shirley, Phys. Rev. B **32**, 1906 (1985).

[30] J. J. Barton, S. W. Robey, and D. A. Shirley, Phys. Rev. B **34**, 778 (1986).

[31] V. Fritzsche, and J. B. Pendry, Phys. Rev. B **48**, 9054 (1993).

[32] J. J. Rehr, and R. C. Albers, Phys. Rev. B **41**, 8139 (1990).

[33] A. P. Kaduwela, G. S. Herman, D. J. Friedman, C. S. Fadley, and J. J. Rehr, Phys. Scr. **41**, 948 (1990).

[34] Y. Chen, F. J. García de Abajo, A. Chassé, R. X. Ynzunza, A. P. Kaduwela, M. A. Van Hove, and C. S. Fadley, Phys. Rev. B **58**, 13121 (1998).

[35] X. Chen, and D. K. Saldin, Compt. Phys. Commun. **112**, 67 (1998).

[36] G. R. Harp, Y. Ueda, X. Chen, and D. K. Saldin, Compt. Phys. Commun. **112**, 80 (1998).

[37] X. Chen, G. R. Harp, Y. Ueda, and D. K. Saldin, Compt. Phys. Commun. **112**, 91 (1998).

[38] F. J. García de Abajo, M. A. Van Hove, and C. S. Fadley, Phys. Rev. B **63**, 075404 (2001).

[39] T. Fujikawa, J. Phys. Soc. Jpn. **50**, 1321 (1981).

[40] H. Shinotsuka, H. Arai, and T. Fujikawa, Phys. Rev. B **77**, 085404 (2008).

[41] D. Sébilleau, C. Natoli, G. M. Gavaza, H. Zhao, F. Da Pieve, and K. Hatada, Compt. Phys. Commun. **182**, 2567 (2011).

[42] J. C. Slater, Phys. Rev. **51**, 846 (1937).

[43] K. Hatada, K. Hayakawa, M. Benfatto, and C. R. Natoli, J. Phys.: Condens. Matter **22**, 185501 (2010).

[44] C. R. Natoli, P. Krüger, K. Hatada, K. Hayakawa, D. Sébilleau, and O. Šipr, J. Phys.: Condens. Matter **24**, 365501 (2012).

[45] J. Xu, P. Krüger, C. R. Natoli, K. Hayakawa, Z. Wu, and K. Hatada, Phys. Rev. B **92**, 125408 (2015).

[46] C. N. Yang, Phys. Rev. **74**, 764 (1948).

[47] D. Dill, J. Chem. Phys. **65**, 1130 (1976).

[48] A. V. Golovin, N. A. Cherepkov and V. V. Kuznetsov, Z. Phys. D **24**, 371 (1992).

[49] E. Shigemasa, J. Adachi, M. Oura, and A. Yagishita, Phys. Rev. Lett. **74**, 359 (1995).

[50] F. Heiser, O. Geßner, J. Viefhaus, K. Wieliczek, R. Hentges, and U. Becker, Phys. Rev. Lett. **79**, 2435 (1997).

[51] A. Yagishita, K. Hosaka, and J. Adachi, J. Electron Spectrosc. Relat. Phenom. **142**, 295 (2005).

[52] K. L. Reid, Annu. Rev. Phys. Chem. **54**, 397 (2003).

[53] K. L. Reid, Mol. Phys. **110**, 131 (2012).

[54] R. N. Zare, Mol. Photochem. **4**, 1 (1972).

[55] S. Motoki, J. Adachi, Y. Hikosaka, K. Ito, M. Sano, K. Soejima, A. Yagishita, G. Raseev, and N. A. Cherepkov, J. Phys. B **33**, 4193 (2000).

[56] N. A. Cherepkov, G. Raseev, J. Adachi, Y. Hikosaka, K. Ito, S. Motoki, M. Sano, K. Soejima, and A. Yagishita, J. Phys. B **33**, 4213 (2000).

[57] A. Lafosse, M. Lebech, J. C. Brenot, P. M. Guyon, O. Jagutzki, L. Spielberger, M. Vervloet, J. C. Houver, and D. Dowek, Phys. Rev. Lett. **84**, 5987 (2000).

[58] K. Ito, J. Adachi, Y. Hikosaka, S. Motoki, K. Soejima, A. Yagishita, G. Raseev, and N. A. Cherepkov, Phys. Rev. Lett. **85**, 46 (2000).

[59] T. Jahnke *et al.*, Phys. Rev. Lett. **88**, 073002 (2002).

[60] O. Geßner, Y. Hikosaka, B. Zimmermann, A. Hempelmann, R. R. Lucchese, J. H. D. Eland, P.-M. Guyon, and U. Becker, Phys. Rev. Lett. **88**, 193002 (2002).

[61] K. Hosaka, J. Adachi, M. Takahashi, A. Yagishita, P. Lin, and R. R. Lucchese, J. Phys. B **37**, L49 (2004).

[62] T. Jahnke *et al.*, Phys. Rev. Lett. **93**, 083002 (2004).

[63] J. Adachi, K. Hosaka, S. Furuya, K. Soejima, M. Takahashi, A. Yagishita, S. K. Semenov, and N. A. Cherepkov, J. Electron Spectrosc. Relat. Phenom. **137–140**, 243 (2004).

[64] N. Saito *et al.*, J. Phys. B **38**, L277 (2005).

[65] T. Teramoto, J. Adachi, K. Hosaka, M. Yamazaki, K. Yamanouchi, N. A. Cherepkov, M. Stener, P. Decleva, and A. Yagishita, J. Phys. B **40**, F241 (2007).

[66] X.-J. Liu *et al.*, Phys. Rev. Lett. **101**, 083001 (2008).

[67] F. P. Sturm *et al.*, Phys. Rev. A **80**, 032506 (2009).

[68] T. Teramoto, J. Adachi, M. Yamazaki, K. Yamanouchi, M. Stener, P. Decleva, and A. Yagishita, J. Phys. B **40**, 4033 (2007).

[69] A. V. Golovin, J. Adachi, S. Motoki, M. Takahashi, and A. Yagishita, J. Phys. B **38**, 3755 (2005).

[70] M. Lebech, J. C. Houver, D. Dowek, and R. R. Lucchese, Phys. Rev. Lett. **96**, 073001 (2006).

[71] J. Adachi, K. Ito, H. Yoshii, M. Yamazaki, A. Yagishita, M. Stener, and P. Decleva, J. Phys. B **40**, 29 (2007).

[72] J. Adachi, K. Hosaka, T. Teramoto, M. Yamazaki, N. Watanabe, M. Takahashi, and A. Yagishita, J. Phys. B **40**, F285 (2007).

[73] K. Hosaka, *Doctor thesis* (in Japanese, Univ. Tokyo, 2004).

[74] K. Hosaka, J. Adachi, A. V. Golovin, M. Takahashi, N. Watanabe, and A. Yagishita, Jpn. J. Appl. Phys. **45**, 1841 (2006).

[75] M. Kazama, J. Adachi, H. Shinotsuka, M. Yamazaki, Y. Ohori, A. Yagishita, and T. Fujikawa, Chem. Phys. **373**, 261 (2010).

[76] J. Adachi, M. Kazama, T. Teramoto, N. Miyauchi, T. Mizuno, M. Yamazaki, T. Fujikawa, and A. Yagishita, J. Phys. B **45**, 194007 (2012).

[77] M. Kazama, H. Shinotsuka, T. Fujikawa, M. Stener, P. Decleva, J. Adachi, T. Mizuno, and A. Yagishita, J. Electron Spectrosc. Relat. Phenom. **185**, 535 (2012).

[78] M. Kazama, T. Fujikawa, N. Kishimoto, T. Mizuno, J. Adachi, and A. Yagishita, Phys. Rev. A **87**, 063417 (2013).

[79] A. H. Zewail, J. Phys. Chem. A **104**, 5660 (2000).

[80] F. Krausz, and M. Ivanov, Rev. Mod. Phys. **81**, 163 (2009).

[81] F. Calegari, G. Sansone, S. Stagira, C. Vozzi, and M. Nisoli, J. Phys. B **49**, 062001 (2016).

[82] K. Ramasesha, S. R. Leone, and D. M. Neumark, Annu. Rev. Phys. Chem. **67**, 41 (2016).

[83] J. Feldhaus, J. Phys. B **43**, 194002 (2010).

[84] J. Phys. B **43**, *Special Issue: Intense X-ray science: the first 5 years of FLASH* (2010).

[85] J. Feldhaus, M. Krikunova, M. Meyer, Th. Möller, R. Moshammer, A. Rudenko, Th. Tschentscher, and J. Ullrich, J. Phys. B **46**, 164002 (2013).

[86] P. Emma *et al.*, Nat. Photon. **4**, 641 (2010).

[87] M. Yabashi, H. Tanaka, T. Ishikawa, J. Synchrotron Rad. **22**, 477 (2015).

[88] T. Ishikawa *et al.*, Nat. Photon. **6**, 540 (2012).

[89] K. Tono *et al.*, New J. Phys. **15**, 083035 (2013).

[90] A. Rudenko, and D. Rolles, J. Electron Spectrosc. Relat. Phenom. **204**, 228 (2015).

[91] C. Bostedt, S. Boutet, D. M. Fritz, Z. Huang, H. J. Lee, H. T. Lemke, A. Robert, W. F. Schlotter, J. J. Turner, and G. J. Williams, Rev. Mod. Phys. **88**, 015007 (2016).

[92] J. Xu, C. I. Blaga, P. Agostini, and L. F. DiMauro, J. Phys. B **49**, 112001 (2016).

[93] H. Stapelfeldt, and T. Seideman, Rev. Mod. Phys. **75**, 543 (2003).

[94] L. Holmegaard, J. H. Nielsen, I. Nevo, and H. Stapelfeldt, Phys. Rev. Lett. **102**, 023001 (2009).

[95] N. Xu, C. Wu, J. Huang, Z. Wu, Q. Liang, H. Yang, and Q. Gong, Opt. Express **14**, 4992 (2006).

[96] A. Korobenko, and V. Milner, Phys. Rev. Lett. **116**, 183001 (2016).

[97] D. Takei, J. H. Mun, S. Minemoto, and H. Sakai, Phys. Rev. A **94**, 013401 (2016).

[98] P. J. Ho, and R. Santra, Phys. Rev. A **78**, 053409 (2008).

[99] A. Debnarova, S. Techert, and S. Schmatz, J. Chem. Phys. **133**, 124309 (2010).

[100] M. P. Minitti *et al.*, Phys. Rev. Lett. **114**, 255501 (2015).

[101] J. Küpper *et al.*, Phys. Rev. Lett. **112**, 083002 (2014).

[102] J. M. Budarz, M. P. Minitti, D. V. Cofer-Shabica, B. Stankus, A. Kirrander, J. B. Hastings, and P. M. Weber, J. Phys B **49**, 034001 (2016).

[103] S. X.-L. Sun, A. P. Kaduwela, A. X. Gray, and C. S. Fadley, Phys. Rev. A **89**, 053415 (2014).

[104] F. Krasniqi, B. Najjari, L. Strüder, D. Rolles, A. Voitkiv, and J. Ullrich, Phys. Rev. A **81**, 033411 (2010).

[105] R. Boll *et al.*, Phys. Rev. A **88**, 061402(R) (2013).

[106] D. Rolles *et al.*, J. Phys B **47**, 124035 (2014).

[107] R. Boll *et al.*, Faraday Discuss. **171**, 57 (2014).

[108] K. Nakajima *et al.*, Sci. Rep. **5**, 14065 (2015).

[109] S. Minemoto *et al.*, Sci. Rep. **6**, 38654 (2016).

[110] A. Yagishita, J. Electron Spectrosc. Relat. Phenom. **200**, 247 (2015).

[111] X. Wang, A.-T. Le, C. Yu, R. R. Lucchese, and C. D. Lin, Sci. Rep. **6**, 23655 (2016).

[112] N.-T. Nguyen, R. R. Lucchese, C. D. Lin, and A.-T. Le, Phys. Rev. A **93**, 063419 (2016).

[113] J. M. Glownia *et al.*, Phys. Rev. Lett. **117**, 153003 (2016).

[114] J. Yang, *et al.*, Phys. Rev. Lett. **117**, 153002 (2016).

[115] T. Yonehara, K. Hanasaki, and K. Takatsuka, Chem. Rev. **112**, 499 (2012).

[116] *Conical Intersections: Theory, Computation and Experiment*, edited by W. Domcke, D. R. Yarkony, and H. Köppel (World Scientific, Singapore, 2011).

[117] S. Tsuru, T. Sako, T. Fujikawa, and A. Yagishita, Phys. Rev. A, submitted.

[118] S. Tsuru, M. Kazama, T. Fujikawa, J. Adachi, and A. Yagishita, J. Phys. B **47**, 071002, (2014).

[119] S. Tsuru, M. Kazama, T. Fujikawa, J. Adachi, T. Mizuno, and A. Yagishita, Chem. Phys. Lett. **608**, 152, (2014).

[120] M. Abramowitz, and I. A. Stegun, *Handbook of Mathematical Functions: with Formulas, Graphs, and Mathematical Tables* (Dover, New York, 1965).

[121] R. D. Cowan, *The Theory of Atomic Structure and Spectra* (California, Berkeley, 1981).

[122] R. D. Cowan's Atomic Structure Code,
http://www.tcd.ie/Physics/people/Cormac.McGuinness/Cowan/

[123] R. Neutze, R. Wouts, D. van der Spoel, E. Weckert, and J. Hajdu, Nature **406**, 752 (2000).

[124] H. N. Chapman *et al.*, Nature **470**, 73 (2011).

[125] M. M. Seibert *et al.*, Nature **470**, 78 (2011).

[126] T. Kimura *et al.*, Nat. Commun. **5**, 3052 (2014).

[127] J. Cooper, and R. N. Zare, J. Chem. Phys. **48**, 942 (1968).

[128] S. Motoki, J. Adachi, K. Ito, K. Ishii, K. Soejima, A. Yagishita, S. K. Semenov, and N. A. Cherepkov, J. Phys. B **35**, 3801 (2002).

[129] D. A. Varshalovich, A. N. Moskalev, and V. K. Khersonskii, *Quantum Theory of Angular Momentum* (World Scientific, Singapore, 1988).

[130] M. E. Rose, *Elementary Theory of Angular Momentum* (Wiley, New York, 1957; republished by Dover, New York, 1995).

[131] A. Messiah, *Quantum Mechanics* (Wiley, New York, 1958; republished by Dover, New York, 2014).

[132] U. Fano, and A. R. P. Rau, *Atomic Collision and Spectra* (Academic, Orlando, Florida, 1986).

[133] *X-ray Data Booklet*, edited by A. C. Thompson Rv. 3 (LBNL/PUB-490, Berkley, 2009), http://xdb.lbl.gov/.

[134] I. M. Band, Yu. I. Kharitonov, and M. B. Trzhaskovskaya, At. Data Nucl. Data Tables **23**, 443 (1979).

[135] J. W. Cooper, Phys. Rev. A **47**, 1841 (1993).

[136] P. H. Bucksbaum, A. Zavriyev, H. G. Muller, and D. W. Schumacher, Phys. Rev. Lett. **64**, 1883 (1990).

[137] L. J. Frasinski, K. Codling, P. Hatherly, J. Barr, I. N. Ross, and W. T. Toner, Phys. Rev. Lett. **58**, 2424 (1987).

[138] T. Seideman, M. Yu. Ivanov, and P. B. Corkum, Phys. Rev. Lett. **75**, 2819 (1995).

[139] K. Hoshina, K. Yamanouchi, T. Ohshima, Y. Ose, and H. Todokoro, J. Chem. Phys. **118**, 6211 (2003).

[140] T. Kanai, S. Minemoto, and H. Sakai, Nature **435**, 470 (2005).

[141] J. Itatani, J. Levesque, D. Zeidler, H. Niikura, H. Pépin, J. C. Kieffer, P. B. Corkum, and D. M. Villeneuve, Nature **432**, 867 (2004).

[142] T. Morishita, A.-T. Le, Z. Chen, and C. D. Lin, Phys. Rev. Lett. **100**, 013903 (2008).

[143] S. Minemoto, T. Umegaki, Y. Oguchi, T. Morishita, A.-T. Le, S. Watanabe, and H. Sakai, Phys. Rev. A **78**, 061402(R) (2008).

[144] F. Rosca-Pruna, and M. J. J. Vrakking, Phys. Rev. Lett. **87**, 153902 (2001).

[145] A. Goban, S. Minemoto, and H. Sakai, Phys. Rev. Lett. **101**, 013001 (2008).

[146] N. A. Cherepkov, and V. V. Kuznetsov, Z. Phys. D **7**, 271 (1987).

[147] T. Elsaesser, and M. Woerner, J. Chem. Phys., **140**, 020901 (2014).

[148] H. M. Berman *et al.*, Acta Crystallogr. Sec. D **58**, 899 (2002).

[149] *Stereochemical Applications of Gas-Phase Electron Diffraction, Part A and B*, edited by I. Hargittai, and M. Hargittai (VCH, New York, 1988).

[150] A. H. Zewail, Annu. Rev. Phys. Chem. **57**, 65 (2005).

[151] D. M. Chase, Phys. Rev. **104**, 838 (1956).

[152] I. Maruyama, T. Sako, and K. Yamanouchi, J. Phys. B **37**, 3919 (2004).

[153] K. Takahashi, and K. Ikeda, J. Chem. Phys. **99**, 8680 (1993).

[154] J. R. Wiesenfeld, and R. H. Young, Chem. Phys. **58**, 51 (1981).

[155] K. P. Huber, and G. Herzberg, *Molecular Spectra and Molecular Structure, Vol. IV, Constants of Diatomic Molecules* (Van Nostrand-Reinhold, New York, 1979; republished by Springer, Berlin, 2013).

[156] F. Martin, R. Bacis, S. Churassy, and J. Vergès, J. Mol. Spectrosc. **116**, 71 (1986).

[157] J. Tellinghuisen, J. Chem. Phys. **134**, 084301 (2011).

[158] K. Yamanouchi, *Quantum Mechanics of Molecular Structures* (Springer, Berlin, 2012).

[159] L. D. Landau, and E. M. Lifshitz, *Quantum Mechanics* (*Non-Relativistic Theory*); *Course of Theoretical Physics, Vol.3*, 3rd edition (Butterworth-Heinemann, Amsterdam, 1981).

[160] P. M. Morse, Phys. Rev. **34**, 57 (1929).

[161] B. H. Bransden, and C. J. Joachain, *Physics of Atoms and Molecules*, 2nd edition (Prentice Hall, New Jersey, 2003).

[162] C. Cohen-Tannoudji, J. Dupont-Roc, and G. Grynberg, *Atom-Photon Interactions: Basic Processes and Applications* (Wiley-VCH, Weinheim, 1998), pp. 203-204.

[163] *Photoemission in Solids I: General Principles*, edited by M. Cardona, and L. Ley (Springer, Berlin, 1978).

[164] A. E. Douglas, and I. Zanon, Can. J. Phys. **42**, 627 (1964).

[165] M. F. Arendt, and L. J. Butler, J. Chem. Phys. **109**, 7835 (1998).

[166] K. Sunanda, A. Shastri, A. K. Das, and B. N. Raja Sekhar, J. Quant. Spectrosc. Radiat. Transfer **151**, 76 (2015).

[167] T. Horio, R. Spesyvtsev, and T. Suzuki, Opt. Express **21**, 022423 (2013).

[168] R. Spesyvtsev, T. Horio, Y.-I. Suzuki, and T. Suzuki, J. Chem. Phys. **142**, 074308 (2015).

[169] C. J. Allan, U. Gelius, D. A. Allison, G. Johansson, H. Siegbahn, and K. Siegbahn, J. Electron Spectrosc. Relat. Phenom. **1**, 131 (1972-1973).

[170] J. H. Sanderson, T. Nishide, H. Shiromaru, Y. Achiba, and N. Kobayashi, Phys. Rev. A **59**, 4817 (1999).

[171] W. A. Bryan, J. H. Sanderson, A. El-Zein, W. R. Newell, P. F. Taday, and A. J. Langley, J. Phys. B **33**, 745 (2000).

[172] L. Adoui *et al.*, Nucl. Instrum. Methods Phys. Res. B **245**, 94 (2006).

[173] R. K. Kushawaha, S. Sunil Kumar, I. A. Prajapati, K. P. Subramanian, and B. Bapat, J. Phys. B **42**, 105201 (2009).

[174] M. R. Jana, P. N. Ghosh, B. Bapat, R. K. Kushawaha, K. Saha, I. A. Prajapati, and C. P. Safvan, Phys. Rev. A **84**, 062715 (2011).

[175] M. Schmidbauer, A. L. D. Kilcoyne, H.-M. Köppe, J. Feldhaus, and A. M. Bradshaw, Phys. Rev. A **52**, 2095 (1995).

[176] S. Miyabe, C. W. McCurdy, A. E. Orel, and T. N. Rescigno, Phys. Rev. A **79**, 053401 (2009).

[177] S. Miyabe, D. J. Haxton, T. N. Rescigno, and C. W. McCurdy, Phys. Rev. A **83**, 023404 (2011).

[178] E. B. Wilson, Jr., J. C. Decius, and P. C. Cross, *Molecular Vibrations: The Theory of Infrared and Raman Vibrational Spectra* (McGraw-Hill, New York, 1955; republished by Dover, New York, 1980).

[179] S. Sugano, Y. Tanabe, and H. Kamimura, *Multiplets of Transition-Metal Ions in Crystals* (Academic Press, New York, 1970).

[180] T. Inui, Y. Tanabe, and Y. Onodera, *Group Theory and Its Applications in Physics* (Springer, Berlin, 1990).

[181] P. R. Bunker, and P. Jensen, *Molecular Symmetry and Spectroscopy*, 2nd edition (NRC, Ottawa, 2006).

[182] G. Herzberg, *Molecular Spectra and Molecular Structure: III. Electronic Spectra and Electronic Structure of Polyatomic Molecules*, 2nd edition (Van Nostrand-Reinhold, New York, 1966; republished by Krieger, Malabar, Florida, 1991).

[183] J. Phys. B **45**, *Special issue on molecular-frame photoelectron angular distributions* (2012).

[184] S. Wada, H. Kizaki, Y. Matsumoto, R. Sumii, and K. Tanaka, J. Phys.: Condens. Matter **18**, S1629 (2006).

[185] R. R. Lucchese, H. Fukuzawa, X.-J. Liu, T. Teranishi, N. Saito, and K. Ueda, J. Phys. B **45**, 194014 (2012).

[186] T. Osipov, C. L. Cocke, M. H. Prior, A. Landers, Th. Weber, O. Jagutzki, L. Schmidt, H. Schmidt-Böcking, and R. Dörner, Phys. Rev. Lett. **90**, 233002 (2003).

[187] M. Yamazaki, J. Adachi, Y. Kimura, A. Yagishita, M. Stener, P. Decleva, N. Kosugi, H. Iwayama, K. Nagaya, and M. Yao, Phys. Rev. Lett. **101**, 043004 (2008).

[188] A. Kivimäki, B. Kempgens, K. Maier, H. M. Köppe, M. N. Piancastelli, M. Neeb, and A. M. Bradshaw, Phys. Rev. Lett., **79**, 998 (1997).

[189] W. Domcke, and L. S. Cederbaum, Chem. Phys. **25**, 189 (1977).

[190] W. Eberhardt, E. W. Plummer, I.-W. Lyo, R. Carr, and W. K. Ford, Phys. Rev. Lett. **58**, 207 (1987).

[191] R. Murphy, and W. Eberhardt, J. Chem. Phys. **89**, 4054 (1988).

[192] D.T. Clark, and J. Müller, Chem. Phys. **23**, 429 (1977).

[193] W. Moffitt, and A. D. Liehr, Phys. Rev. **106**, 1195 (1957).